THERMO-MECHANICAL CHARACTERIZATION OF COMPOSITE MATERIALS AT CRYOGENIC TEMPERATURES FOR SPACE APPLICATIONS USING COMPUTATIONAL TECHNIQUES

DISSERTATION-II

Submitted in Partial fulfilment of the requirement for the award of degree

of

MASTER OF TECHNOLOGY

in

MECHANICAL ENGINEERING

by

Danish Handa

(11507112)

Under the guidance of

Dr. Raja Sekhar Dondapati (17715)

DEPARTMENT OF MECHANICAL ENGINEERING
LOVELY PROFESSIONAL UNIVERSITY
PUNJAB
2016-2017

CERTIFICATE

I hereby certify that the work being presented in the dissertation entitled ***"Thermo-Mechanical Characterization of Composite Materials at Cryogenic Temperatures For Space Applications Using Computational Techniques"*** in partial fulfilment of the requirement of the award of the Degree of master of technology and submitted to the Department of Mechanical Engineering of Lovely Professional University, Phagwara, is an authentic record of my own work carried out under the supervision of Dr. Raja Sekhar Dondapati, Associate Professor, Department of Mechanical Engineering, Lovely Professional University. The matter embodied in this dissertation has not been submitted in part or full to any other University or Institute for the award of any degree.

Date: Danish Handa

11507112

This is to certify that the above statement made by the candidate is correct to the best of my knowledge.

Date: Dr. Raja Sekhar Dondapati

(17715)

COD: Piyush Gulati

The external viva-voce examination of the student was held successfully on

Signature of Examiner

DECLARATION

I, Danish Handa, student of **Master of Technology (Mechanical Engineering)** under School of **Mechanical Engineering** of Lovely Professional University, Punjab, hereby declare that all the information furnished in this dissertation reports based on my own intensive research and is genuine. This dissertation does to the best of my knowledge, contain part of my work which has been submitted for the award of my degree either of this university without proper citation.

Danish Handa
11507112

Date:

ACKNOWLEDGEMENT

I offer my sincerest gratitude to my supervisor, **Dr. Raja Sekhar Dondapati**, Associate Professor, School of Mechanical Engineering, Lovely Professional University, Punjab and Mrs**. Preeti Rao Usurumarti**, P.V.K.Institute of Technology, Ananthapur, Andhra Pradesh who has supported me throughout my thesis with their patience, knowledge, valuable advice, uninterrupted active supervision and constant encouragement. I attribute the level of my Master's degree to their encouragement and effort without them this thesis, too, would not have been completed or written.

I am thankful to **Mr. Gaurav Vyas**, Assistant Professor, School of Mechanical Engineering, Lovely Professional University, Punjab who continuously motivated, clearing concepts and encouraged me to do this research work.

I am thankful to **Mr. Gurpreet Singh Phull**, (HOS) and **Mr. Piyush Gulati** (COD) School of Mechanical Engineering, Lovely Professional University, Punjab

I would like to thank all the staff members of the School of Mechanical engineering who have been very patient and cooperative with us.

I would also like to extend my gratitude to my seniors Mr. Abhinav Kumar, Mr. Mohit Kalsia, friend Mr. Seepana PraveenKumar and who always encouraged and supported me in this thesis work.

I would like to acknowledge the support extended by IIT Kharagpur in providing the necessary computational facilities to carry out this work.

I would like to thank **Lovely Professional University** for giving me the opportunity to use their resources and work in such a challenging environment. I am grateful to the individuals who contributed their valuable time towards my thesis.

Last but not the least, I express my sincere gratitude to my parents who have always supported me throughout my studies at university and encouraged me with their best wishes.

Danish Handa
11507112

TABLE OF CONTENTS

LIST OF FIGURES

ABSTRACT

Composite materials are used in various applications such as military, aerospace, sports equipment, railways, etc. Due to low weight to strength ratio, composite materials are preferred in space applications. However, these composite materials when used for fuel and oxygen carrying tanks experience cryogenic temperatures. During this time, these composite materials are prone to cracking thereby aiding failure of the material. Hence, an attention is needed to develop and characterize a composite material which can be used at cryogenic temperatures.

In the present work, Thermo-mechanical characterization on Kevlar composite is to be done using computational techniques. Further, the failure of Kevlar due to the propagation of cracks at cryogenic temperatures is predicted using Extended Finite Element Method (X-FEM). This method involves the assumption of an un-cracked portion of composite material as a continuum and the cracked portion as a discontinuity in the material. The stress concentrations zones and the strain energy that is absorbed while the crack propagates are predicted.

CHAPTER

1 INTRODUCTION

Kevlar 49 due to its excellent mechanical and thermal properties such as high tensile modulus, high strength to weight ratio, high impact resistance, low thermal conductivity and negative coefficient of thermal expansion has become significantly popular in recent years for its increasing applications in the aerospace industry, especially at cryogenic temperatures as support structures, vessels, cryogenic tanks for storing fuel in rocket or spacecraft, etc. [1]–[4]. It has very low compressive strength. However, while bending, it establishes a high degree of yielding on the compression side. Such a failure mode is not observed in glass and carbon fibers, and gives Kevlar 49 composites superiority [5]. Moreover, at cryogenic temperatures, materials undergo ductile to brittle transition (DTBT) which contributes to the development of micro-cracks thereby aiding failure of the structure as they are unable to resist the propagation of cracks. Further, the compatibility of Kevlar based composites at cryogenic temperatures made it possible be used in superconducting devices, which include high temperature superconducting cables [6]–[8], superconducting magnets [9]–[11], superconducting motors [12]–[14], etc. However, for retaining the superconductivity, these superconducting devices need to be cooled at very low temperatures (cryogenic temperatures). Especially in superconducting motors in which the torque tube must have the capability to hinder the effect of heat transfer between the driven and the driving end. One end of the torque tube is exposed to the atmospheric conditions, whereas the other end to the cryogenic conditions. Hence, the material must be thermally stable in order to get sustained in such conditions as the materials possess brittle behaviour at cryogenic temperatures due to which they undergo brittle failure. Hence, an attention is needed for better understanding of the crack growth behaviour. Various researchers, Viola et al. [15], Aliabadi et al. [16], Broberg [17], Lim et al. [18], Nobile and Carloni [19] and García-Sánchez et al. [20] have purposed analytical solutions for the propagation of cracks and dynamic analysis of cracks in anisotropic and orthotropic materials. Nonetheless, the analytical methods are not protean enough for solving arbitrary problems, numerous numerical techniques such as boundary element method, collocation method, finite difference method, finite element method (FEM),

extended finite element method (X-FEM) and numerical manifold method has been developed for better prediction of cracks [21], [22].

In this research work, using linear elastic fracture mechanics (LEFM) approach, the mechanical behaviour of Kevlar 49 composites with three cases of edge crack, one being towards the loading end, the second being at the middle and the last being towards the fixed end of the specimen are considered under tension at room temperature and the cryogenic temperature is investigated by developing two-dimensional finite element models using extended finite element method (X-FEM) technique in a commercial code Abaqus/CAE. Stress, strain, strain energy and strain energy density as a function of the width of the Kevlar specimen for the surface just above and below the crack is analyzed at various pressures ranging from 100 MPa to 1000 MPa and further are validated with the analytical relations obtained from the literature.

CHAPTER

2 TERMINOLOGY

Composite materials are replacing the conventional metals and nonmetals for various applications including on-ground and off-ground applications. Hence, researchers around the world are concentrating upon the development of new composite materials for the applications in demand. On the other side, the manufacturers are replacing their equipment to be compatible with composite material manufacturing. Due to significantly large applications of composite materials, it is essential to investigate the behaviour of these materials at various mechanical and thermal loading conditions. The following sections discuss the classification of composite materials along with the theories of failure applicable to these materials. Further, to determine the failure of the composite materials, it is necessary to observe the failure behavior of the materials. Therefore, the fracture mechanics criteria are discussed in the subsequent sections.

2.1 Composite Materials

Composites are proving to be an essential part of today's era. Composites are preferred over monolithic materials because these materials cannot meet the demands of today's innovative technologies. For example, it is necessary for Satellites to be dimensionally steady in space where the temperature varies between -160˚C to 93.3˚C and the coefficient of thermal expansion is limited to the value as low as of the order of $\pm 1.8\times10^{-7}$ m/m/˚C [23]. These conditions cannot be met by monolithic materials. Therefore composites such as Kevlar/epoxy, graphite/epoxy, boron/epoxy, etc. are preferred over monolithic materials.

A Composite can be defined as the compounding of two or more constituents at the macroscopic level to form a third useful material that results in better properties than those of the individual components used alone. The constituents are reinforcements (fibres, particles or flakes), the main load carrying constituent and a matrix, which holds the fibres together and keep them in their specified position and it can further be classified as a polymer matrix, metal matrix, ceramic matrix and carbon matrix. Due to the use of advanced composite materials in several applications such as aerospace, railways, sports equipment, military equipment, etc., the word 'composite' have become popular in recent years. However, there

are several historical examples of composites in the literature. The composites came into existence around 10000 BC. The most common composite which was used as a construction material was straw bricks. Then further the composite materials that were used for developing the writing materials were fibrous composite materials, developed during the Egyptian era at about 4000 BC. These writing materials were fabricated from the papyrus plant and then were laminated. Further, Egyptians used heat-softened glass to make containers from coarse fibres. In 1930s, advanced composites came into existence such as glass fibers which were reinforced with resins. Aircrafts and boats were developed by using these glass composites which are nowadays commonly known as fibre- glass. Since the 1970s, application of composites boosted due to the advancement of new fibres such as aramids, boron and carbon, etc. and new composite systems with matrices made of metals and ceramics. The properties that can be improved by forming a composite material are: strength, stiffness, thermal conductivity, fatigue life, temperature dependent behaviour, corrosion resistance, wear resistance, weight, acoustical insulation, etc.

2.1.1 Classification and Characteristics of Composite Materials

Composite materials are generally classified into two systems; one is based on matrix materials and other on reinforcement.

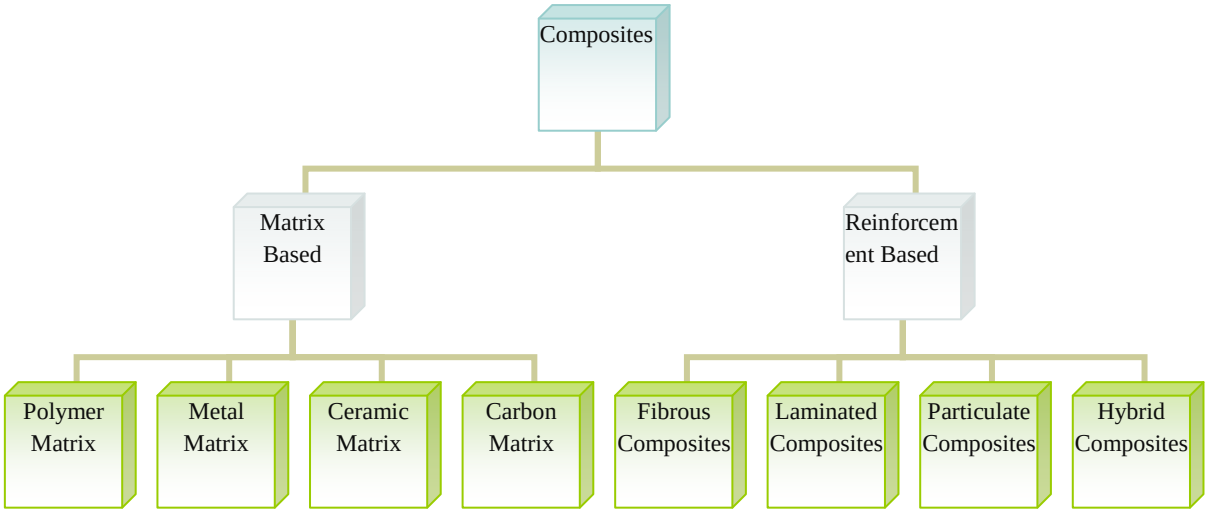

Figure 1 Classification of composites on the basis of matrix and reinforcement

2.1.1.1 Classification of Composites Based on Matrix Material

Matrix materials can further be classified into following categories: polymer matrix, metal matrix, ceramic matrix and carbon matrix.

2.1.1.1.1 Polymer Matrix

Polymer matrices are light weight, corrosion resistant and are less costly in comparison to other matrices. A Polymer is a long chain of molecules containing one or more repeated units known as monomers, which are joined together by covalent bonds. It can further be classified as: Thermoplastic polymers in which the molecules are not chemically joined. They are held in place by weak forces such as Vander wall's and hydrogen bonding. These can be re-shaped. Examples: Polymethyl methacrylate (PMMA), Acrylonitrile butadiene styrene (ABS), Nylon, Polycarbonate, etc. Thermosetting Polymers are composed of molecules, chemically joined by cross links due to which they cannot be re-shaped. However, if the number of cross links is less, then in some cases it is possible to re-shape the materials at high temperatures. Examples: Bakelite, Polyester, epoxies, Polyurethane, etc.

2.1.1.1.2 Metal Matrix

Metal matrices are used for high strength applications and in those cases where long term use is made. Example: In severe environment such as high temperature and chemical attack. Metals can be strengthened by number of heat treatment processes along with the mechanical treatments. However, they have more weight in comparison to polymers and are prone to corrosion. Commonly used metal matrices are aluminium and titanium, and other metal matrices can be magnesium, beryllium, nickel and cobalt.

2.1.1.1.3 Ceramic Matrix

Ceramic matrices have the low fracture toughness in comparison to polymers and metals, as these are brittle materials and whenever a crack originates, it will propagate at a very rapid rate. Commonly used ceramic matrices are silicon carbide, silicon nitride, aluminium nitride, boron nitride, etc. Alumina (Al_2O_3) and Mullite (Al_2O_3+SiO_2) are the two commonly used oxide ceramics. Silicon nitride has the highest strength, whereas aluminium nitride has the highest thermal conductivity.

2.1.1.1.4 Carbon Matrix

Carbon matrices are used along with the carbon fibres where even high temperatures are encountered, generally in range of 2000˚C to 3000˚C.

2.1.1.2 Classification of Composites Based on Reinforced Material Structure

Reinforced materials can be classified into following: Fibrous composites, laminated composites, particulate composites and hybrid composites.

2.1.1.2.1 Fibrous Composites

As the name suggests, the fibrous composites are the composites developed from polymer matrix reinforced with fibres. The fibres used are glass fibre, carbon fibre, boron fibre, etc. and the polymers used are epoxy, polyester, etc. Due to their high strength to weight ratio, they are used in various applications such as aerospace, railways, sport equipment, etc.

2.1.1.2.2 Laminated Composites

A laminate composite is made up of two or more layers (lamina's) of different materials that are bonded together. Example: plywood is a laminate in which one layer or lamina is placed over the other to form a laminate. It can be classified into the following categories; Bi metals, are laminates of two different metals that have different coefficients of thermal expansion. These are used to make thermostats. Clad metals, are used to combine the properties of two or more metals. Example: High strength aluminium alloy does not resist corrosion, but has high strength. Whereas pure aluminium is corrosion resistance, but have less strength. Therefore, high strength aluminium alloy is covered or clad with pure aluminium in order to attain high strength and corrosion resistance. Fibre glass or safety glass is a layer of polyvinyl butyl which is a plastic, sandwiched between two layers of glass. The brittleness of the glass gets reduced due to plastic and its impact strength greatly improves.

2.1.1.2.3 Particulate Composite

It contains particles of metals or non-metals, suspended in a matrix of another material which can be metallic or non-metallic. Depending upon the type of particle and matrix used, the particulate composites are classified into four categories: Non-metallic particles in a non-metallic matrix. Example: Rocket propellants contain aluminium powder which is metallic and polyurethane matrix which is non-metallic. Metallic particles in a non-metallic matrix. Example: Concrete is a particulate composite in which sand and gravel particles are combined with a mixture of cement and water. Non-metallic particles in a metallic matrix. Example: Boron carbide in stainless steel is used for making control rods. Metallic particles in a metallic matrix. Example: Lead particles used in copper alloys and steel to improve machinability. Lead is a natural lubricant which is used in bearings made from copper alloys

2.1.1.2.4 Hybrid Composites

Combinations of some or all types of composites are known as hybrid composites. Laminated fibre reinforced composites comes under the category of hybrid composites, in which layers of fibre reinforced materials are bonded together with different fibre directions in each layer.

2.1.2 Applications of Composites

Composite materials are widely used in the applications as follows:

2.1.2.1 Aerospace Applications

- Composite materials are used for making space telescopes, space crafts, satellites, booster rockets, etc.
- Carbon-Carbon composites are used on the leading edges of the space shuttles as it can sustain very high temperatures.
- India's light combat aircraft (LCA) is made from Kevlar fibre reinforced polymer composites.
- Glass composites are used in the tail fin of the combat aircraft.

2.1.2.2 Missiles

Composites are used for making rocket motor cases, nozzles, nose cone and interstage structures.

2.1.2.3 Railways

Composites are used to make bodies of railway bogies, railway tracks, gear cases and pantographs.

2.1.2.4 Sports Equipment

- Modern day tennis rackets are made from a high strength graphite or carbon fibres, which make them strong and lightweight.
- Sports helmets, hockey sticks, surfing bolts, scuba diving tanks, speed boats and racing cars such as F-1 are other where composites are widely used.

2.1.2.5 Automotive

- Composites are used to make brake shoes, clutch plates, spring and shafts, which are generally made from carbon fibres.
- Other applications include accelerators, radiators and fuel tanks.

2.1.2.6 Military Applications

Helmets, bullet proof jackets, portable bridges and non-detectable ships are generally made from composite materials.

2.1.2.7 Marine Applications

Ship and boat hulls, masts, hovercrafts, which run on land and water, heat exchangers, ventilation ducts, engineering foundations, etc., are some of the areas where composites are used.

2.1.3 Classification of Fibres

Fibres are generally classified into following: Natural fibres and advance fibres

1.1.3.1 Natural Fibres

Natural fibers are divided into three following categories:

- Plant or Vegetable fibres such as cotton, jute, bamboo, sugar cane, etc.
- Animal fibres like silk, spider silk, camel hair, sinew fibre, etc.
- Mineral fibres for example asbestos, basalt, mineral wool, glass wool, etc.

1.1.3.2 Advance Fibres

Advance fibres are the fibres which have high specific stiffness and high specific strength. They have higher strength than natural fibres.

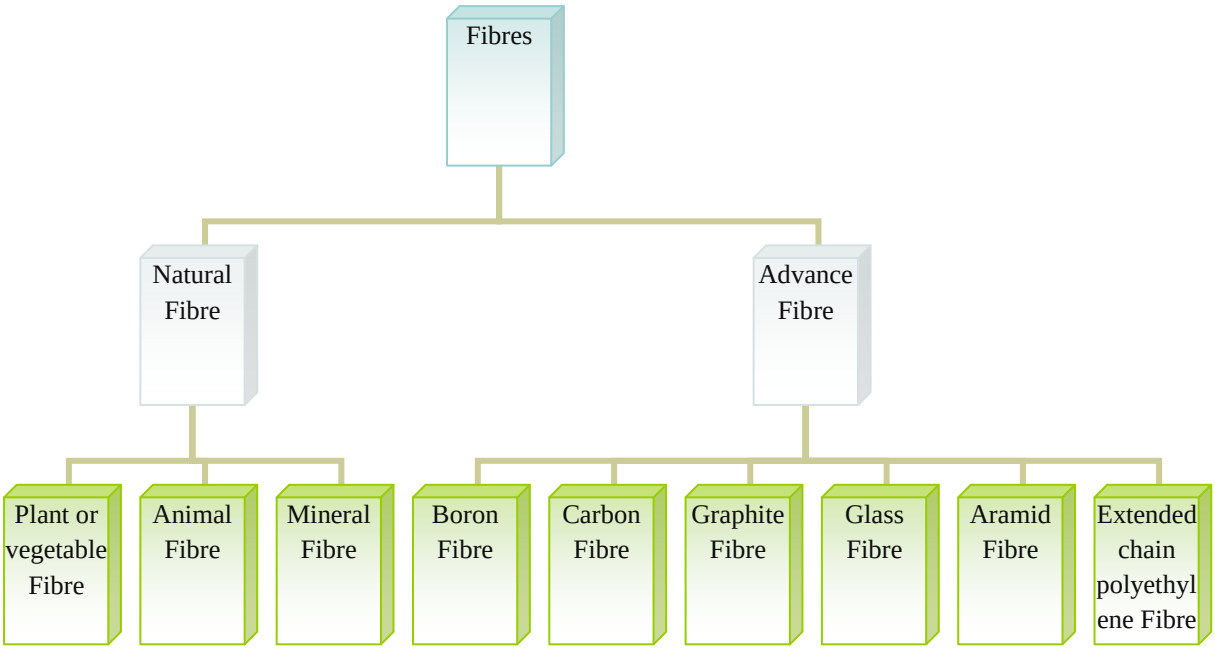

Figure 2 Classification of fibres

2.1.4 Failure Theories for Composite Materials

Various parameters that are used for relating the failure theories are:

$(\sigma_1^T)_{ult}$ - Ultimate longitudinal tensile strength (in direction 1)

$(\sigma_2^T)_{ult}$ - Ultimate transverse tensile strength (in direction 2)

$(\sigma_1^C)_{ult}$ - Ultimate longitudinal compressive strength (in direction 1)

$(\sigma_2^C)_{ult}$ - Ultimate transverse compressive strength (in direction 2)

$(\tau_{12})_{ult}$ - Ultimate in-plane shear strength 

There are various theories for determining the failure of a laminate. These theories can be classified as follows:

2.1.4.1 Maximum Stress Theory:

The theory is based on the maximum normal stress theory and the maximum shear stress theory developed by Rankine and Tresca respectively. This theory states that if the stress, normal or the shear in a lamina equals or exceeds the corresponding ultimate stress of that lamina, then the laminate will fail. Mathematically, it can be written as:

$$-(\sigma_1^C)_{ult} < \sigma_1 < (\sigma_1^T)_{ult}$$

$$-(\sigma_2^C)_{ult} < \sigma_2 < (\sigma_2^T)_{ult}$$

$$-(\tau_{12})_{ult} < \tau_{12} < (\tau_{12})_{ult}$$

If the above criteria are violated, the material will fail.

2.1.4.2 Maximum Strain Theory:

This theory is based on maximum normal strain theory given by Saint-Venant's and the maximum shear stress theory which is commonly known as Tresca theory. Failure in lamina will be obtained if any of the following condition is violated.

$$-(\varepsilon_1^C)_{ult} < \varepsilon_1 < (\varepsilon_1^T)_{ult}$$

$$-(\varepsilon_2^C)_{ult} < \varepsilon_2 < (\varepsilon_2^T)_{ult}$$

$$-(\gamma_{12})_{ult} < \gamma_{12} < (\gamma_{12})_{ult}$$

2.1.4.3 Tsai Hill Failure Theory:

This theory is based on Von Mises theory, also known as distortion energy failure theory. According to this theory, the material fails when distortion energy is greater than the failure distortion energy of the material. Hill modified this theory to adapt it for a uni-directional lamina as given below:

$$(G_2+G_3)\sigma_1^2+(G_1+G_3)\sigma_2^2+(G_1+G_2)\sigma_3^2-2G_3\sigma_1\sigma_2-2G_2\sigma_1\sigma_3-2G_1\sigma_2\sigma_3$$
$$+2G_4\tau_{23}^2+2G_5\tau_{13}^2+2G_6\tau_{12}^2<1$$

Here G_1, G_2, G_3, G_4, G_5 and G_6 are components of strength criteria and are evaluated as follows:

Case 1:

$$\text{Apply } \sigma_1 = (\sigma_1^T)_{ult}$$

$$\text{Therefore, } (G_2+G_3)(\sigma_1^T)_{ult} = 1$$

Case 2:

$$\text{Apply } \sigma_2 = (\sigma_2^T)_{ult}$$

$$\text{Therefore, } (G_1+G_3)(\sigma_2^T)_{ult} = 1$$

Case 3:

$$\text{Apply } \sigma_3 = (\sigma_3^T)_{ult}$$

$$\text{And } (\sigma_3^T)_{ult} = (\sigma_2^T)_{ult}$$

$$\text{Therefore, } (G_1 + G_2)(\sigma_2^T)_{ult} = 1$$

Case 4:

$$\text{Apply } \tau_{12} = (\tau_{12})_{ult}$$

$$\text{Therefore, } 2G_6(\tau_{12}^2)_{ult} = 1$$

Where:

$$G_1 = \frac{1}{2}\left[\frac{2}{(\sigma_2^T)_{ult}^2} - \frac{1}{(\sigma_1^T)_{ult}^2}\right]$$

$$G_2 = \frac{1}{2}\left[\frac{1}{(\sigma_1^T)_{ult}^2}\right]$$

$$G_3 = \frac{1}{2}\left[\frac{1}{(\sigma_1^T)_{ult}^2}\right]$$

$$G_6 = \frac{1}{2}\left[\frac{1}{(\tau_{12}^2)_{ult}}\right]$$

Assuming plane stress, that is $\sigma_3, \tau_{23}, \tau_{13} = 0$

$$\left[\frac{\sigma_1}{(\sigma_1^T)_{ult}}\right]^2 - \left[\frac{\sigma_1\sigma_2}{(\sigma_1^T)_{ult}^2}\right] + \left[\frac{\sigma_2}{(\sigma_2^T)_{ult}}\right]^2 + \left[\frac{\tau_{12}}{(\tau_{12})_{ult}}\right]^2 < 1$$

If the above condition is violated, the laminate will fail.

2.1.4.4 Tsai Wu Failure Theory:

This theory is based on total strain energy failure theory. Tsai Wu considered the Beltrami theory for studying the failure of uni- directional lamina assuming plane stress condition. A lamina is considered to be failed if the following condition is violated.

$$H_1\sigma_1 + H_2\sigma_2 + H_3\sigma_3 + H_{11}\sigma_1^2 + H_{22}\sigma_2^2 + H_{66}\tau_{12}^2 + 2H_{12}\sigma_1\sigma_2 < 1$$

Case 1:

$$\text{Apply } \sigma_1 = (\sigma_1^T)_{ult}, \sigma_2 = 0 \text{ and } \tau_{12} = 0$$

$$\text{Therefore, } H_1(\sigma_1^T)_{ult} + H_{11}(\sigma_2^T)_{ult}^2 = 1$$

Case 2:

$$\text{Apply } \sigma_1 = -\left(\sigma_1^C\right)_{ult}, \sigma_2 = 0 \text{ and } \tau_{12} = 0$$

$$\text{Therefore, } -H_1\left(\sigma_1^C\right)_{ult} + H_{11}(\sigma_1^C)_{ult}^2 = 1$$

$$H_1 = \frac{1}{\left(\sigma_1^T\right)_{ult}} - \frac{1}{\left(\sigma_1^C\right)_{ult}} \text{ and } H_{11} = \frac{1}{\left(\sigma_1^T\right)_{ult}\left(\sigma_1^C\right)_{ult}}$$

Case 3:

$$\text{Apply } \sigma_2 = \left(\sigma_2^T\right)_{ult}, \sigma_1 = 0 \text{ and } \tau_{12} = 0$$

$$\text{Therefore, } H_2\left(\sigma_2^T\right)_{ult} + H_{22}(\sigma_2^T)_{ult}^2 = 1$$

Case 4:

$$\text{Apply } \sigma_2 = -\left(\sigma_2^C\right)_{ult}, \sigma_1 = 0 \text{ and } \tau_{12} = 0$$

$$\text{Therefore, } -H_2\left(\sigma_2^C\right)_{ult} + H_{22}(\sigma_2^C)_{ult}^2 = 1$$

$$H_2 = \frac{1}{\left(\sigma_2^T\right)_{ult}} - \frac{1}{\left(\sigma_2^C\right)_{ult}} \text{ and } H_{22} = \frac{1}{\left(\sigma_2^T\right)_{ult}\left(\sigma_2^C\right)_{ult}}$$

Case 5:

$$\text{Apply } \sigma_1 = 0, \sigma_2 = 0 \text{ and } \tau_{12} = \left(\tau_{12}\right)_{ult}$$

$$\text{Therefore, } H_6\left(\tau_{12}\right)_{ult} + H_{66}\left(\tau_{12}\right)_{ult}^2 = 1$$

Case 6:

$$\text{Apply } \sigma_1 = 0, \sigma_2 = 0 \text{ and } \tau_{12} = -\left(\tau_{12}\right)_{ult}$$

$$\text{Therefore, } -H_6\left(\tau_{12}\right)_{ult} + H_{66}\left(\tau_{12}\right)_{ult}^2 = 1$$

$$H_6 = 0 \text{ and } H_{66} = \frac{1}{\left(\tau_{12}\right)_{ult}^2}$$

For obtaining H_{12}, experimental procedures are followed. One of the procedures is explained below:

Apply equal tensile loads along the axis 2.

If $\sigma_x = \sigma_y = \sigma$ and $\tau_{xy} = 0$ is the load at which the lamina fails then

$$\left(H_1 + H_2\right)\sigma + \left(H_{11} + H_{22} + 2H_{12}\right)\sigma^2 = 1$$

Therefore, we will get H_{12} as

$$H_{12} = \frac{1}{2\sigma^2}\left[1 - \left(H_1 + H_2\right)\sigma - \left(H_{11} + H_{22}\right)\sigma^2\right]$$

2.2 Fracture Mechanics

Fracture mechanics deals with the development and propagation of the crack, the forces required for the propagation of a crack, the stresses produce at the tip of the crack and the displacements and strains associated with the propagation of a crack. Fracture mechanics can be studied through a number of parameters.

- Energy release rate (ERR)
- Stress intensity factor (SIS)
- Crack tip opening displacement (CTOD)
- J - Integral

Typically, the structures fail due to the development of a crack. The failure of the structures is classified into categories Type-I and Type-II.

- Type-I failure occurs due to negligence during design, construction or operation of a structure.
- Type-II failure occurs due to application of a new design technology which produces unexpected results. Example: World War II liberty ships.

2.2.1 History of Fracture Mechanics

The fracture mechanics developed after the Second World War. Before that, the knowledge was limited and the designs were based on the Egyptian era. The Egyptians built the pyramids with stones and these structures are still standing tall due to their design. The Romans constructed several structures, but their designs were limited to compression loading, as at that time the construction materials used were timber, brick and mortar. These were used as they were able to bear compressive loading due to their brittle nature. After the industrial revolution, there was mass production of iron and steel due to which new designs came into existence, such as the tower bridge in London. During the World War II, most of the ships manufactured by American and British navy were destroyed due to brittle failure even though their hull was made of steel. This happened due to the **Ductile to Brittle Transition (DTBT)** of steel under freezing temperatures. These ships were made using welding techniques instead of the riveted joints, which were unable to resist the propagation of cracks. This is an example of Type-II failure. In order to solve this problem, a naval research lab was set up in Washington DC in 1945. In the lab, various researchers such as Irwin, Wells and Westergaard conducted experiments on different types of materials such as brittle, ductile, viscoplastic, viscoelastic, etc. [24]. In 1956, Irwin developed the energy

release rate concept which was derived from Griffith's theory. Irwin extended the Griffith's approach to ductile materials by including plastic as well as elastic energy. Westergaard developed a technique for analyzing the stresses and displacements near the tip of the crack and Irwin used this approach to show that the stresses and displacements near the tip of the crack could be described by a constant known as stress intensity factor (SIF).

In 1956, Wells used the fracture mechanics concept to identify the cause of failure in a comet jet aircrafts. General Electric manufactured large size steam turbines in 1957. However, these turbines suffered failure due to bursting of the large rotor forgings. In order to solve this problem, Winne and Wundt applied the fracture mechanics approach, using the Irwin's Energy release rate concept. In 1960's, **Linear Elastic Fracture Mechanics (LEFM)** concept was developed, but was unable to predict the failure of ductile materials. Therefore, the number of researchers such as Irwin, Dugdale, Barenblatt and Wells developed **Elastic Plastic Fracture Mechanics (EPFM)** theory around 1960s. Further, in the 1960s, Wells performed experiments on medium and high strength structural steels, during his tenure at the British Welding Research Association and these steels were unable to be characterized by LEFM. Therefore, another parameter was required for their characterization and this parameter was related to the crack tip opening displacement and hence this parameter was known as **Crack Tip Opening Displacement (CTOD)**. In 1968, Rice [25] developed another parameter for characterizing the nonlinear material behaviour near the tip of the crack by assuming plastic deformation near the crack tip as nonlinear elastic and developed a line integral to calculate this nonlinear energy release rate and this parameter was called as **J integral**. In the same year, Hutchinson [26], Rice and Rosengren [27] developed the J integral approach and applied it to the crack tip stress fields in nonlinear materials, known as HRR singularity. This theory was applied to nuclear power plants in 1970s by two researchers, Begley and lands. They applied the J integral approach to characterize the fracture toughness of the steel used in nuclear boilers. No further major breakthrough was observed in fracture mechanics till the computers came into existence, in 1980's. With the advancement of computer technology and finite element method (FEM) modelling software, the researchers were able to accurately predict the propagation of cracks in different types of materials. Nowadays, dedicated software such as NISA (Numerically integrated method for system analysis), ABAQUS, Solidworks, Ansys, etc. are available for accurate prediction of the stresses and displacements near the tip of the crack. Another common technique which is

widely used now-a-days is photoelasticity, a branch physics in which due to the phenomena of interference, displacement contours and stress contours are easily predicted.

2.2.2 Fracture Mechanics Approach to Design

Figure 3 compares the fracture mechanics approach with the traditional approach to structural design and material selection. Most of the design approaches deal with the yield strength of a material in which the applied stress is compared with the yield strength of the material. If the applied stress is lower than the yield strength, the material is considered as safe for engineering application, but the fracture approach has three parameters: 1. Applied stress 2. Flaw/crack size 3. Fracture toughness.

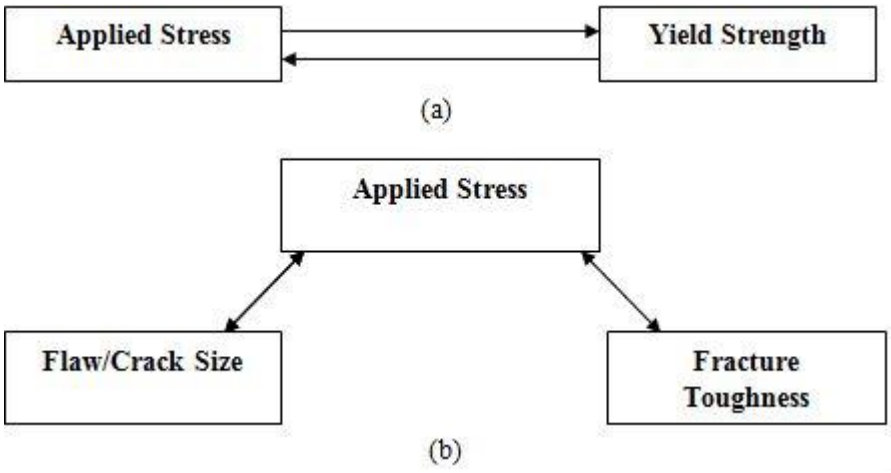

Figure 3 Comparison of the fracture mechanics approach to design with the traditional strength of materials approach: (a) the strength of materials approach (b) the fracture mechanics approach.

There are two substitute approaches for the analysis of fracture: the energy approach and the stress-intensity approach, discussed below.

2.2.2.1 Energy Approach

The energy approach was given by Griffith [28] and it states that a crack will grow in size when the energy/stress applied is sufficient to overcome the resistance of a material. The resistance offered by the material includes the surface energy, plastic work and other types of energy dissipation associated with crack load. According to Griffith, the Energy Release rate (ERR) 'G' which is defined as the rate of change in potential energy with the crack area for a linear elastic material.

$$ERR = -\frac{d\pi}{dA}$$

The ERR for an elliptical crack is given by:

$$G = \frac{\pi\sigma^2 a}{E}$$

Where 'E' is the Young's Modulus, 'σ' is the applied stress and 'a' is half the crack size as shown in Figure 4. The energy approach states that the fracture will take place when $G \geq G_c$, which is the critical energy release rate and given by following equation.

$$G_c = \frac{\pi\sigma_f^2 a_c}{E}$$

Where 'σ_f' is the fracture stress, and 'a_c' is the critical length of the crack.

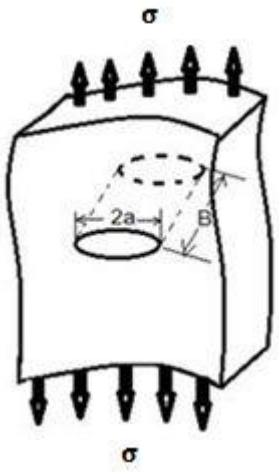

Figure 4 Crack in an infinite plate subjected to a uniaxial tensile stress.

2.2.2.2 Stress Intensity Approach

The stress intensity approach is based on the stress intensity factor (K).

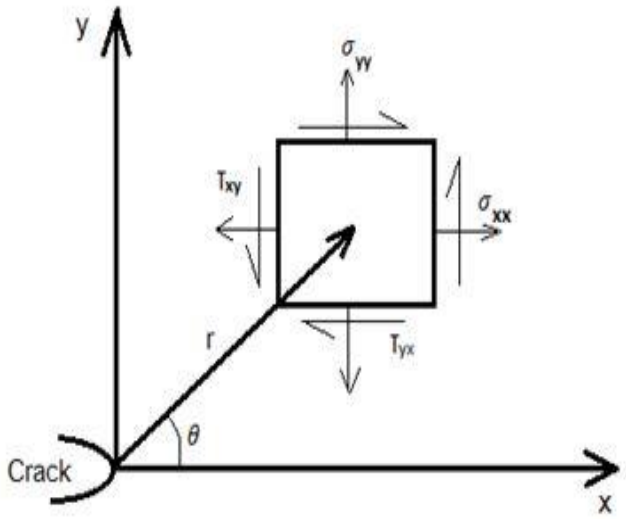

Figure 5 Stresses nearby the tip of a crack in an elastic material [24].

$$\sigma_{XX} = \frac{K_1}{\sqrt{2\pi r}} Cos\left(\frac{\theta}{2}\right)\left[1 - Sin\left(\frac{\theta}{2}\right) Sin\left(\frac{3\theta}{2}\right)\right]$$

$$\sigma_{YY} = \frac{K_1}{\sqrt{2\pi r}} Cos\left(\frac{\theta}{2}\right)\left[1 + Sin\left(\frac{\theta}{2}\right) Sin\left(\frac{3\theta}{2}\right)\right]$$

$$\tau_{XY} = \frac{K_1}{\sqrt{2\pi r}} Cos\left(\frac{\theta}{2}\right) Sin\left(\frac{\theta}{2}\right) Sin\left(\frac{3\theta}{2}\right)$$

All the three stresses shown above, the stress value is varying with angle 'θ', the 'r' value (distance of the element from the tip of the crack) and the constant of proportionality K_1. This constant is known as a stress intensity factor, which relates the stresses at a particular point in a material with the stresses at the tip of the crack. Similar to 'G_c', the stress intensity approach states that the crack will propagate when $K_1=K_{1c}$, Where K_{1c} is the critical stress intensity factor and it is the measure of material resistance.

$$K_1 = \sigma\sqrt{\pi a}$$

$$K_{1c} = \sigma_f \sqrt{\pi a_c}$$

The relationship between K_1 and G can be written as:

$$G = \frac{K_1^2}{E}$$

G_c and K_{1c} will also hold the same relation. Thus, for linear elastic materials, the energy and stress intensity approaches to fracture mechanics are essential.

2.2.3 Crack Tip Plastic Zone

Irwin [29] and Dugdale [30] predicted the size of plastic zone at the tip of the crack. A stress singularity exists in front of a physical crack, which means, stress is infinite at the tip of the crack. However, in actual while conducting experiments, it has been found that stress never reaches infinity due to plastic deformation at the crack tip. This means that there is always a region around the crack tip where plastic deformation occurs and stress singularity diminishes, this zone is known as the crack tip plastic zone.

2.2.3.1 Irwin Plastic Zone Correction

Assuming plane stress case, Figure 6 shows the magnitude of the stress 'σ_y', in the plane $\theta=0$ until a distance 'r_p^*' from the crack tip, the stress is higher than the yield stress 'σ_{ys}'.

$$\sigma_y = \frac{K_1}{\sqrt{2\pi r_p^*}} = \sigma_{ys}$$

$$r_p^* = \frac{\sigma^2 a}{2\sigma_{ys}^2}$$

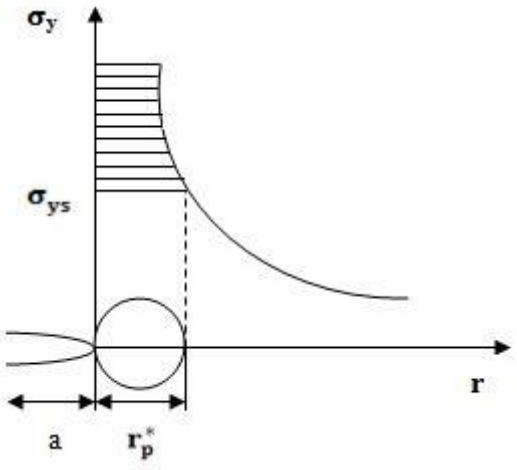

Figure 6 Plastic zone at crack tip

Irwin showed that the actual plastic zone size must be larger than the first estimate of the r_p^*. The load shown by the shaded area must be carried forward so the material slightly beyond the plastic zone will also be brought under a stress above the yield stress. Therefore, the crack behaves as if it is slightly longer than the physical size of the crack. The effective crack size

is then equal to $(a+\delta)$. The fig shows a physical crack of size 'a' replaced by a longer crack of size $(a+\delta)$.

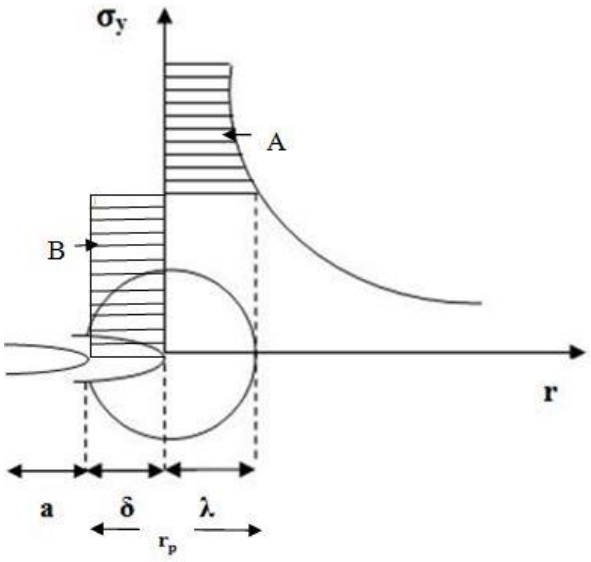

Figure 7 Physical crack of size 'a' replaced by a longer crack of size 'a+δ'.

Figure 7 shows a physical crack of size 'a' replaced by a longer crack of size $(a+\delta)$. The stress at the tip of the effective crack is again limited to yield stress and the stress acting on the part 'δ', in front of the physical crack is equal to the yield stress. Therefore 'δ' must be large enough to carry the load, which is lost by cutting the area 'A'.

$$\sigma_{ys} = \frac{K_1}{\sqrt{2\pi\lambda}} = \sigma\frac{\sqrt{\pi(a+\delta)}}{\sqrt{2\pi\lambda}}$$

$$\lambda = \frac{\sigma^2(a+\delta)}{2\sigma_{ys}^2} \approx r_p^*$$

Equating the shaded area A and B,

$$\delta\sigma_{ys} = \left[\int_0^{\lambda} \sigma\sqrt{\frac{a+\delta}{2r}}dr\right] - \lambda\sigma_{ys}$$

$$\sigma_{ys}(\delta+\lambda) = 2\left(\sigma\sqrt{\frac{a+\delta}{2}}\right)\left(\sqrt{r}\right)_0^{\lambda}$$

$$\sigma_{ys}(\delta+\lambda) = \sigma\sqrt{2ar_p^*}$$

$$\left(\delta + r_p^*\right) = \frac{\sigma}{\sigma_{ys}}\sqrt{2ar_p^*}$$

$$\left(\delta + r_p^*\right)^2 = 4r_p^{*2}$$

$$\left(\delta + r_p^*\right) = 2r_p^*$$

$$\delta = r_p^* = \lambda$$

$$r_p = \delta + \lambda$$

$$r_p = 2r_p^*$$

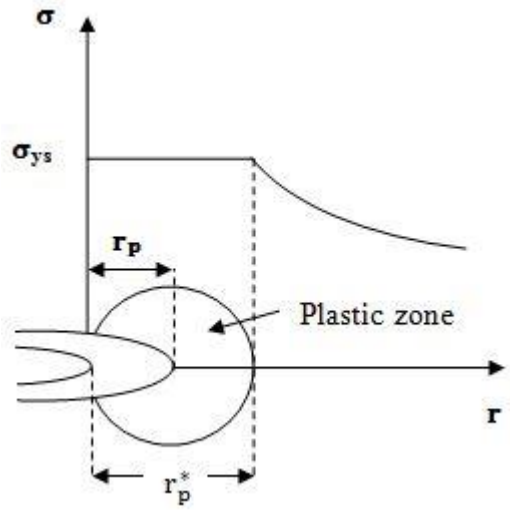

Figure 8 Estimation of plastic zone size

The plastic zone correction if applied consistently, then a connection to the value of K is also necessary. Therefore, the new stress intensity factor, including the Irwin plastic zone correction becomes equal to:

$$K = c\sigma\sqrt{\pi\left(a + r^*\right)}$$

2.2.3.2 Dugdale Approach

Dugdale considered a crack subjected to a remote tensile stress 'σ' and developed a relation for the size of the plastic zone by using the superposition principle as shown below:

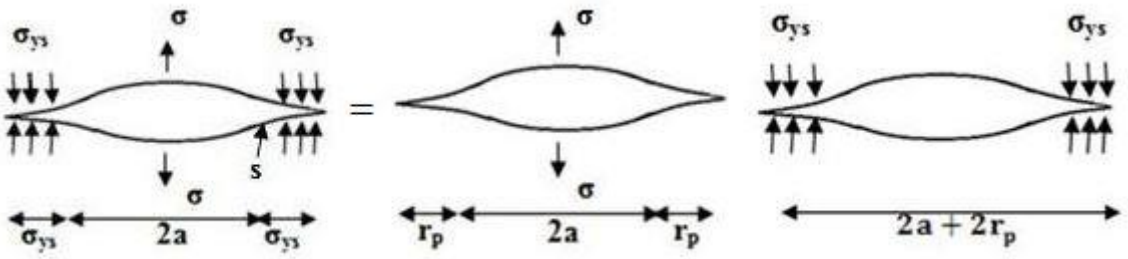

Figure 9 The Dugdale model, using superposition law

Dugdale considered an effective crack which is longer than the physical crack. The crack edges 'r_p^*' in front of the physical crack carries the yield stress 'σ_{ys}'. The size of 'r_p^*' is chosen in such a way that the stress similarity disappears. This means that the stress intensity due to remote stress 'σ' must be compensated by the stress intensity due to the wedge forces.

$$K_\sigma = -K_{\sigma_{ys}} = -K_{r_p}$$

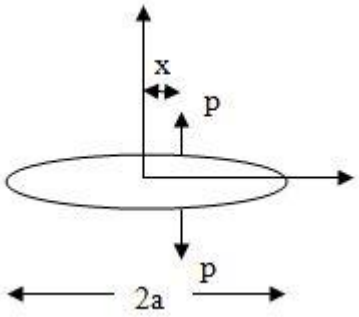

Figure 10 Crack-opening force applied at a distance x from the centre line

As per the relation for stress intensity due to a wedge force 'P' as given as:

$$K_A = \frac{P}{\sqrt{\pi a}}\sqrt{\frac{a+x}{a-x}}$$

$$K_A = \frac{P}{\sqrt{\pi a}}\sqrt{\frac{a-x}{a+x}}$$

If the wedge forces are distributed from point 's' to the crack tip, the SIF can be written as

$$K_A = \frac{P}{\sqrt{\pi a}}\int_s^a \left(\sqrt{\frac{a+x}{a-x}} - \sqrt{\frac{a-x}{a+x}}\right)dx$$

$$K = 2P\sqrt{\frac{a}{\pi}}\int_s^a \frac{1}{\sqrt{\left(a^2 - x^2\right)}}dx$$

$$K = 2P\sqrt{\frac{a}{\pi}}\arccos\left(\frac{s}{a}\right)$$

Applying the result of the Dugdale model, integral will be taken from a to $a + r_p$, therefore substituting $s = a$, $a = a + r_p$ and $p = \sigma_{ys}$

$$K_{r_p} = 2\sigma_{ys}\sqrt{\frac{a + r_p}{\pi}}\arccos\left(\frac{a}{a + r_p}\right)$$

Making use of equation

$$K_\sigma = \sigma\sqrt{\pi\left(a + r_p\right)}$$

Neglecting negative sign

$$\sigma\sqrt{\pi\left(a + r_p\right)} = 2\sigma_{ys}\sqrt{\frac{\left(a + r_p\right)}{\pi}}\arccos\left(\frac{a}{a + r_p}\right)$$

$$Cosx = \left(1 - \frac{x^2}{2!} + \frac{x^4}{4!} - \frac{x^6}{6!}.....\right)$$

$$\arccos\left(\frac{a}{a + r_p}\right) = \frac{\sigma\pi}{2\sigma_{ys}}$$

$$\left(\frac{a}{a + r_p}\right) = Cos\left(\frac{\sigma\pi}{2\sigma_{ys}}\right)$$

$$\left(\frac{a}{a + r_p}\right) = 1 - \left(\frac{\sigma^2\pi^2}{8\sigma_{ys}^2}\right)$$

$$r_p = \frac{8\sigma_{ys}^2 a}{8\sigma_{ys}^2 - \sigma^2\pi^2} - a$$

$$r_p = \frac{\pi K^2}{8\sigma_{ys}^2}$$

2.2.4 J-Integral

J integral is used for the case where there is significant crack tip plasticity because in such cases the value of 'G' is affected by crack tip plastic zone. Eshelby [31] defined number of contour integrals on line integrals which are path independent, by virtue of theorem of energy conservation. One such 2-D integral can be written as:

$$J = \int_{\Gamma} \omega dy - T \frac{\partial U}{\partial x} ds$$

Where ω is the strain energy per unit volume.

$$\omega(x, y) = \int_0^{\varepsilon} \sigma_{ij} d\varepsilon_{ij}$$

T is the traction force

$$T = \sigma_{ij} n_{ij}$$

U is the displacement in x-direction and ds is the element of url (Γ).

J=0 along any any closed contour. This can be shown below:

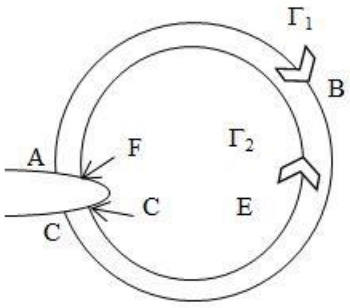

Figure 11 A closed contour where J = 0

Along AF & CD, $T = 0$ and displacement in 'y' direction, $dy = 0$. Therefore $J = 0$ for AF and CD, contribution of ABC must be equal to the contribution of DEF, i.e., $J_{\Gamma 1} = J_{\Gamma 2}$. It proves that J integral is path independent. J integral, is an energy related quantity because both ω and $T \frac{\partial U}{\partial x}$ have the dimensions of strain energy. J integral is defined as the change in

potential energy for a virtual crack extension 'da', i.e., $J = -\frac{\partial V}{\partial a}$, where V is the potential energy. For linear elastic material, 'J' becomes equal to 'G' and also $J = \left(\frac{\partial V}{\partial a}\right)_p = -\left(\frac{\partial V}{\partial a}\right)_\Delta$

$$\left.\begin{aligned} V &= -\frac{1}{2}P\Delta \\ -\left(\frac{\partial V}{\partial a}\right)_p &= \frac{1}{2}P\left(\frac{\partial \Delta}{\partial a}\right)_p \\ -\left(\frac{\partial V}{\partial a}\right)_\Delta &= \frac{1}{2}P\left(\frac{\partial P}{\partial a}\right)_\Delta \end{aligned}\right\} \text{ For linear elastic case}$$

$$\left.\begin{aligned} J &= \left(\frac{\partial V}{\partial a}\right)_p = \int_0^P \left(\frac{\partial \Delta}{\partial a}\right)_p dP \\ J &= -\left(\frac{\partial V}{\partial a}\right)_p = \int_0^\Delta \left(\frac{\partial P}{\partial a}\right)_\Delta d\Delta \end{aligned}\right\} \text{ For nonlinear elastic case}$$

Above equations can be shown diagrammatically as below,

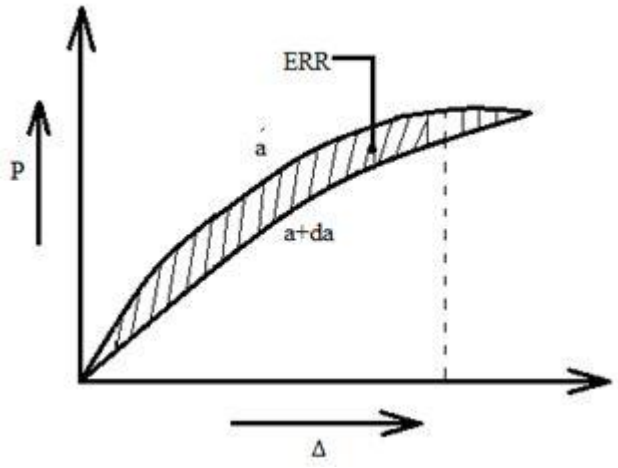

Figure 12 Nonlinear energy release rate (ERR)

Elastic plastic materials can be treated as non-linear elastic if the material unloads along the same path as it was loaded. This is the basic assumption for calculating the J integral. This theory is known as the deformation theory of plasticity. The area under the curve gives the ERR. The material unloads the same curve as along which it was loaded.

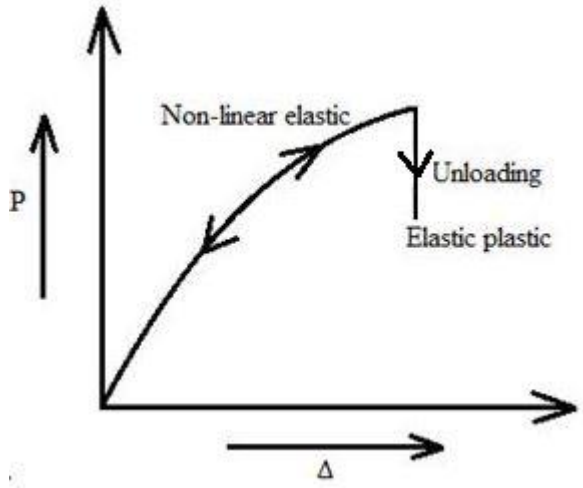

Figure 13 Schematic comparison of the stress-strain behaviour of elastic-plastic and nonlinear elastic materials

The elastic plastic material unloads along a different path, whereas a non-linear elastic material unloads along the same path along which it was loaded. Therefore, if no unloading is allowed we can assume elastic plastic case to be equivalent to the non-linear elastic case. This is known as the deformation theory of plasticity. If exact results are to be obtained, then the incremental theory of plasticity should be used. J integral is the more universal criteria than ERR because it is applicable to the cases where significant plastic deformation is associated with crack growth and fracture. J for linear elastic case becomes equal to:

$$J = G = \frac{K^2}{E}$$

2.2.5 Crack Tip Opening Displacement

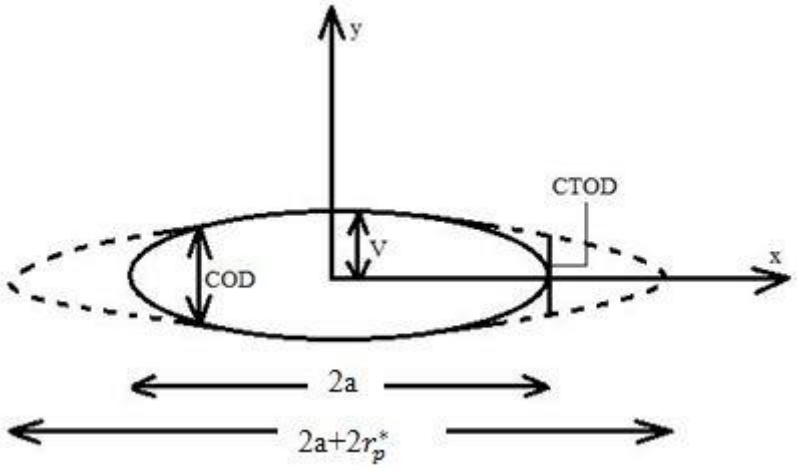

Figure 14 Estimation of COD in terms of CTOD

The effective solution for crack displacement COD is given by:

$$COD = 2v = \frac{4\sigma}{E}\sqrt{a^2 - x^2}$$

Using Irwin's plastic zone correction r_p^*,

$$COD = \frac{4\sigma}{E}\sqrt{\left(a + r_p^*\right)^2 - x^2}$$

Here $\left(a + r_p^*\right)$ is the effective crack size and the origin at the centre of the crack. The CTOD is found by substituting $x = a$

As r_p^{*2} is very small, therefore

$$CTOD = \frac{4\sigma}{E}\sqrt{2ar_p^*}$$

The general expression for COD can be written as:

$$COD = \frac{4\sigma}{E}\sqrt{2a_{eff}r}$$

CTOD can be obtained from the above equation by putting $r = r_p^*$ and $a_{eff} = a$, where $2a_{eff} = 2a + 2r_p^*$.

Substituting the value of r_p^*, that is

$$r_p^* = \frac{4K_1^2}{\pi E\sigma_{ys}}$$

Therefore,

$$CTOD = \frac{4\sigma}{E}\sqrt{\frac{2a^2\sigma^2}{2\sigma_{ys}^2}}$$

$$CTOD = \frac{4}{\pi}\frac{K_1^2}{E\sigma_{ys}}$$

This equation is valid in the area of linear elastic fracture mechanics (LEFM). Substituting the expression for CTOD in COD equation.

$$CTOD^2 = \frac{16\sigma^2}{E^2}2ar_p^*$$

Therefore,

$$COD = \frac{4\sigma}{E}\sqrt{a^2 - x^2 + \frac{E^2}{16\sigma^2}\left(CTOD^2\right)}$$

The above equation is used for finding the CTOD by measuring a COD value through a clip gauge. Alternatively, we can use the Dugdale approach to find CTOD. CTOD given by Dugdale is as shown below:

$$CTOD = \frac{8\sigma_{ys}a}{\pi E}\log\left(Sec\frac{\pi a}{2\sigma_{ys}}\right)$$

Expanding $\log\left(Sec\frac{\pi a}{2\sigma_{ys}}\right)$, we get

$$CTOD = \frac{8\sigma_{ys}a}{\pi E}\left[\frac{1}{2}\left(\frac{\pi a}{2\sigma_{ys}}\right)^2 + \frac{1}{12}\left(\frac{\pi a}{2\sigma_{ys}}\right)^4 + ...\right]$$

Neglecting higher order terms, we get

$$CTOD = \frac{\pi\sigma^2 a}{E\sigma_{ys}} = \frac{G_1}{\sigma_{ys}}$$

Comparing with the previous equation to CTOD, the difference is a factor of

$$\left(\frac{4}{\pi}\right)$$

Li et al., [32] presented the concept of extended cohesive damage model (ECDM) in order to simulate multicrack propagation in fibre composites. A cohesive damage model using Extended Finite Element Method (XFEM) was introduced for developing ECDM. It was reported that by excluding the enriched degree of freedoms (DoFs), multicrack propagation in fibre composites can effectively be predicted without knowing the crack paths in advance. It was proposed that ECDM works well for muticrack failure in fibre composites.

N. R. Iyer et al., [33] in their work introduced innovative methods for analysing the fracture and damage tolerant estimation of metallic structural components for the effective and safe design of structures. XFEM and Numerically Integrated Modified Virtual Crack Closure Integral (NI-MVCCI) method is used for investigating the cracked stiffened panels when fractured. Strain energy release rate, stress intensity factor, residual stress and remaining life assessment under various loading conditions were evaluated.

S. C. Wu et al., [34] used Extended Finite Element Technique and Virtual Node Polygonal Method (VPM) for determining the properties such as thermophysical, fracture and mechanical considerations for discs of the brake, made of forged alloy steel. Computational outcomes were engaged to estimate the fatigue lifespan and safety territory of in-service and due to emergency breaking mode and crack propagation due to thermal fatigue was attained for estimating the safety degree of the brake disc.

H. Zhang et al., [35] investigated the effect of tangential force on fretting fatigue of Al 2024-T351 alloy specimens using XFEM in combination with the Cyclic Cohesive Zone Model. They concluded that as the tangential force increases, the depth of the knee point increases. Moreover, crack growth life, crack initiation life and total fatigue life decrease.

G. Liu et al., [36] analysed the fatigue behaviour of arbitrary crack growth in ductile materials, using corrected Extended Finite Element Method (XFEM). Von Mises yield criterion along with isotropic hardening and Newton–Raphson iterative method was used to model finite strain plasticity and solve nonlinear problem respectively. Mixed-mode stress

intensity factors were determined by the Interaction integral method and crack growth angle and rate by the modified Paris law and the maximum principal stress criterion, respectively.

K. P. Marimuthu et al., [37] investigated Characterization on the development of cone-cracks in brittle materials upon spherical indentation by using Extended Finite Element Method (XFEM). When an indenter touched the surface part outside the ring crack, a kinked-cone-crack was observed. The effects of friction, Poisson's ratio on cone-crack evolution were analysed and then an Extended Finite Element (XFE) analyses were performed in order to determine the database for Roesler's constant.

T. Huang and Y. X. Zhang [38] developed an Extended Finite Element model using ABAQUS via the user element subroutine (UEL) in order to determine the multiple crack behaviour and tensile strain hardening of engineered cementitious composites (ECC) under uniaxial loading. It was observed that the random fibre distribution and random matrix flaws affected the tensile behaviour of ECC.

Y. Liu et al., [39] used an Extended Finite Element Method (XFEM) for analysing the influence on the crack growth characteristic of unbonded areas geometric parameters. An experiment was performed to find the effect of crack growth due to the unbonded areas sizes and locations along the thickness. It was observed that the unbonded areas effectively increased the fatigue life and blocked the crack growth.

N. Rodriguez-Florez et al., [40] analysed the behaviour of crack growth through bone's intra-cortical pores, using Extended Finite Element Method (XFEM) in ABAQUS. Multiple enriched regions with independent crack-growth possibilities and void material properties that were assigned to the pores were compared and found that multiple cracks will initiate progressively by assigning multiple enrichment regions, which will not be seen when the voids are filled. It was concluded that realistic fracture patterns will not be created if the pores are filled with one enrichment region in the model.

H. Jia and Y. Nie [41] analysed the interaction between a single or multiple macroscopic inclusion and macroscopic crack defects under thermo-mechanical load by implementing the Extended Finite Element approach. The thermo-mechanical response of the material under the effects of different shapes of multiple inclusions was investigated. By using an interaction integral method or the M-integral method, stress intensity factors of cracks were

obtained and in the case of multiple cracks or multiple inclusions, the stress, strain and stiffness fields were simulated.

X. Xu et al., [42] based on the high-speed photography, experimentally investigated the crack problem in terms of crack propagation speed and morphology. With the purpose of studying the effects of multiple cracks, a 3D model using Extended Finite Element Method (XFEM) was created. Based on K criterion of a brittle solid and displacement field of the crack tip, brittle dynamic stress intensity factors (DSIFs) of several failure modes were investigated.

R. Dimitri et al., [43] predicted the fracture direction of propagation inside a specimen and computed the stress intensity factor for cracked plates under different loading conditions by combining the numerical Extended Finite Element Method (XFEM) with the level set method. The results obtained from the XFEM are compared with the theoretical data given in the handbooks and found to be significant.

Z.Wang et al., [44] analysed the fracture behaviour of three-dimensional linear elastic solids by considering 3D straight and curved planar cracks, using novel local mesh refinement approach. A structural coupling system using variable-node transition hexahedron elements based on the generic point interpolation with a random number of nodes on each of their faces was presented in order to treat the mismatching problem induced by different scale-meshes in the domain. The three-dimensional finite element approximations of field variables were enhanced by enrichments with a purpose that the mesh turns out to be fully independent of the crack geometry. Linear elastic fracture parameters such as stress intensity factors were evaluated using displacement extrapolation method and were validated by the XFEM results and found to be significant.

A. Nasirmanesh and S.Mohammadi [45] analysed cracked functionally graded cylindrical shells by performing Eigen value buckling analysis with eight nodded degenerated shell elements using Extended Finite Element Method (XFEM). Functionally graded materials (FGM) cylindrical shells which were subjected to different loading conditions such as axial compression, axial tension and combined axial compression and internal pressure were examined and the effects of various parameters such as aspect ratio of the cylinder and internal pressure, crack length and angle and gradient index of the material on the buckling behaviour were also investigated.

K. Huang et al., [46] proposed a new domain-independent interaction integral (DII-integral) that can be used to estimate the dynamic stress intensity factors (DSIFs) of an interface crack in nonhomogeneous materials under dynamic loading conditions. Therefore an extended finite element method (X-FEM) in combination with the DII-integral was used to inspect the effectiveness of DII-integral and the significance of material non-homogeneity on the DSIFs and found that the results were in good agreement for an interface crack in nonhomogeneous materials.

Z. Wang et al., [47] described a numerical framework for modelling approximate holes and inclusions in three-dimensional solids depending on an exact combination of the locally enriched partition of unity method, the variable-node hexahedron elements and a posterior error estimation scheme. Accuracy, effectiveness and performance of the approach was demonstrated by a series of numerical illustrations that involved single and multiple inclusions or holes in three dimensions with different arrangements.

L. Wu et al., [48] applied an edge-based smoothed extended finite element method (ES-XFEM) for analysing the dynamic fracture of 2D elastic solids under impact loading. The dynamic stress intensity factor (DSIF) was deduced from the J-integral approach with the support of the strain smoothing method. The analysis showed that ES-XFEM is an efficient numerical approach for simulating the dynamic fracture problems.

X. F. Hu et al., [49] performed an experiment on a double cantilever beam for three-dimensional delamination migrations in multidirectional composite laminates and validated the results using integrated extended finite element method along with the cohesive element method. The numerical results clarified that due to the interaction between delamination and matrix crack, the tested specimens failed.

L.Marsavina et al., [50], with three different densities 100, 145 and 300 kg/m3 under mixed mode loading examined the behaviour of PUR foams. Asymmetric semi-circular bend and asymmetric Four-Point Bend specimens were used to perform the experiments. Four fracture criteria such as maximum energy release rate, equivalent stress intensity factor, maximum circumferential tensile stress and strain energy density were used to compare the crack initiation angles recognised for the asymmetric semi-circular bend.

C. Zhang et al., [51] determined the numerical solutions for identifying the crack problems in elastodynamics, using the Nelder–Mead and Quasi-Newton optimization techniques. XFEM together with Newmark-β method by means of Rayleigh damping was respectively used to model the fracture and employ the time integration. Various tests were conducted for dynamic loads and found that the Nelder-Mead method worked more effective under the harmonic load than the pounding load whereas the Quasi-Newton method attains nearly the identical results.

T. J. Singh et al., [1] reviewed the mechanical and thermal characteristics of Kevlar fibre and its composites. Kevlar 49 fabrics, when investigated for different ranges of strain rates, the dynamic properties such as young´s modulus, tensile strength, maximum strain and toughness, are dependent on strain rate. The compressive strength of Kevlar composite was found to be less and tensile to compressive strength ratio, high when compared with glass and carbon fibre. Kevlar fibre reinforced Hybrid composites when hybridised with other fibres such as glass, carbon, etc. improves the thermal as well as mechanical properties.

S. N. Raja et al., [52] conducted a quasi-static tensile test by using a novel continuous dynamic analysis (CDA) for monitoring the development in loss factor and storage modulus of Kevlar 49 fibres as a function of strain. Rate dependent stress and strain results obtained for Kevlar were compared to Nomex, polyester, rubber and spider silk. They also found that the storage modulus of Kevlar came to be equal to Young's modulus and the measured quantifiable relations between storage modulus and strain provided perceptions in the change of the mechanical properties of aramid for specific applications.

R. Tian and L.Wen., [53] presented an improved extended finite element method (iXFEM) to overcome the difficulties such as ill-conditioning and mass lumping corresponding to extra degree of freedoms from three aspects: 1) eliminating the linear dependence and the ill-conditioning problems of the standard and the corrected XFEMs; 2) to eliminate extra degree of freedoms in crack tip enrichment to simplify optimal mass lumping in dynamic analyses; 3) to be interpolating at enriched nodes to permit direct essential/contact boundary behaviours. The iXFEM is numerically examined and compared with the standard XFEM and the corrected XFEM and established that iXFEM in terms of accuracy, convergence, and conditioning/stability gives excellent performance.

S. H. Ardakani et al., [54] used an extended finite element approach for analysing the fracture of shape memory alloys for super elastic and shape memory effects. First of all, the stationary crack mode was investigated and then the effects of loading rate on the behaviour of materials in the crack tip were examined. In the existence of an initial crack, analysis for the propagation of crack was performed by implementing a weighted averaging criterion, where the direction of the propagation of crack was determined by weighted averaging of effective stresses at all the integration points around the crack tip.

G. Wang et al., [55] employed an XFEM approach for analysing the electric field of insulating plate subjected to crack. Classic finite element method and extended finite element method were compared by performing two numerical tests and found that for electric field analysis of discontinuous and singular solutions, XFEM has some advantages over the classic finite element method. XFEM was practiced to analyse the electric field at the crack tip of an insulating plate subjected to an edge crack, which revealed that the relative error between CFEM and XFEM came out to be small when the mesh size of XFEM around the crack tip was larger than that of CFEM.

F. Curá et al., [56] investigated the relationship between rim and web thickness in thin-rimmed gears, alluding to bending failures on the path where the crack was propagated. Using linear elastic fracture mechanics approach, a three-dimensional, extended finite element model was generated from numerical simulations. Three-dimensional XFEM techniques predicted the crack propagation paths subjected to bending for various geometries of gear, related to the preliminary crack position along the width of the face. ISO blank factor CR was introduced for predicting the results due to the interaction between rim and web geometries.

J. J. Liu et al., [57] calculated the distribution of crack tip stress for different crack lengths and stress intensity factors and rate of fatigue crack propagation on 5E62 aluminium alloy. The values of crack tip stress and stress intensity factor increased as the crack length increased in the Paris region, resulted in the increment of fatigue crack growth rate.

M. Yu et al., [58] introduced XFEM for studying the behaviour of propagation of crack on the different load ratio under shear and tension. It was observed that the path through which the crack propagates does not depend upon meshing and the crack expands through the mesh.

It was concluded that the angle with which the crack propagates became smaller as the ratio of tension to shear displacement increased.

Y. L. Pang and D. M. Dai [59] introduced the basic theory of the XFEM and conducted the simulation of the behaviour of crack propagation for fibre reinforced materials. Analysed the edge crack and central crack behaviour and found that for edge cracks, the overall stiffness of the specimen reduced with the expansion of crack as the cross-sectional area of the fibre decreased and found that for central crack, the propagation of crack does not affect the overall stiffness of the specimen.

S. Natarajan et al., [60] used XFEM, one of the partition unity methods in order to study the interaction between a crack and an inclusion. Crack tip stress field distribution was studied numerically under the influence of few parameters such as crack length, the geometry of the inclusions and the number of inclusions. Numerical examples such as inclusion-crack interaction and crack tip shielding have been studied to check the accuracy of the work.

L. P. Qiu et al., [61] investigated the behaviour of propagation of a crack in wood by developing the XFEM based models in ABAQUS. Experimental work was performed on curved Glulam beams under bending loads subjected to four point bending for determining elastic properties of Northeast China larch and Mode I and Mode II fracture toughness.

X. D. Zhang et al., [62] invested and provided a new idea for the detection of cracks in beam-like structures. An extended finite element analysis was performed to identify the effect of free vibrations on the beam-like structures subjected to a crack. The XFEM along with the genetic algorithms was effectively used to detect a crack in a cantilever beam.

A. Bersani et al., [4] conducted an experiment for measuring the rate of elongation of Kevlar-49 fibre at low temperatures and examined the long-term performances of the Kevlar-49 fibre at low temperatures, the fibre was kept under a constant tension of 2.7 kg at 4.2K for a period of 8 months and concluded that the Kevlar-49 fibre can safely be used in cryogenic applications where a high mechanical stability under stress is needed.

D. Zhu et al., [63] investigated the stress–strain response in warp and fill directions, the effect of poisson’s ratio, and the response of in-plane shear for Kevlar 49 fabric. The stress-strain responses of Kevlar 49 in both warp and fill directions, exhibits nonlinear and orthogonal behaviour. The young´s modulus appears to be same for both warp and fill directions. The

crimp strain, the tensile strength, and the ultimate strain differ between both the directions. The poisson´s ratio of the fabric is a function of strain, in the beginning, it increases as the strain increases and then decreases gradually until the specimen fails at a strain of 2.5%. Depending on the level of pre-load, the maximum value of the poisson's ratio varies in the range 0.35 to 0.75. The shear response being nonlinear consists of four distinct regions that are: linear elastic rotation region, dissipative rotation region, yarn compression region and shear locking region.

M. Cheng et al., [64] performed an experiment to obtain the mechanical properties of single Kevlar KM2 fibre subjected to various loading conditions such as longitudinal, transverse, etc. Kevlar KM2 fibres show linear and elastic behaviour when loaded in the longitudinal direction. When loaded transversely, Kevlar KM2 fibres show large deformation. A large residual strain is determined in the transverse direction of the Kevlar KM2 fibre, however, it does not significantly affect the mechanical properties in the longitudinal direction.

X. Q. Li et al., [65] investigated a three-point bending numerical simulation of CFRP reinforced concrete beam with initial crack based on XFEM using ABAQUS software. The numerical study for non-CFRP and CFRP plies presented the path where the propagation of crack takes place, under crack damage modes and ultimate loading condition.

B. L. James et al., [3] investigated mechanical properties of Titanium 15-3-3-3 and Kevlar 49 subjected to tensile loads at room temperatures as well as at cryogenic temperatures. It was reported that Kevlar 49 have a higher break strength, tensile modulus, ultimate tensile strength and yield strength at 77 K than at room temperature. However, the elongation does not change much with low temperatures. At 5K, Titanium 15-3-3-3 becomes very brittle, the break strength, ultimate tensile strength and yield strength increased significantly

A. R. M. Kasavajhala and L. Gu [21] examined the behaviour of single edge v-notched crack in the aluminium plate by developing 3-D finite element models using ABAQUS software and further analysed the behaviour of crack when repaired with e-glass/epoxy and Kevlar-49/epoxy prepreg patches on both sides. The effect of patch repair, crack length and adhesive thickness was discussed and found that for all cases, the results proved to be better for the case of e-glass/epoxy and Kevlar-49/epoxy than the bare plate and the service life of composite-repaired structures improved.

R. P. Reed and M. Golda [66] reviewed the tensile, compressive, fatigue, thermal expansion, thermal conductivity and specific heat of unidirectional laminates reinforced with boron, alumina, aramid, S-glass, E-glass, and high strength, high modulus and medium modulus carbon fibres at various temperature ranges from 4 K to 295K. Composite tensile strengths and moduli depend primarily on the fibre strength and moduli, but compressive and fatigue properties also depend on the matrix resin. The fibres have a wide range of thermal properties at low temperatures. Two fibres, aramid and carbon (graphite), expanded axially on cooling to low temperatures. The thermal conductivities of glass and alumina were found to be relatively low at ambient temperatures. However, at very low temperatures (<30 K), the thermal conductivities of carbon fibres were concluded to be the lowest. The specific heats of fibre- reinforced composites were comparable to, or higher than, those of metals and alloys used in cryogenic structures.

G. Hartwig and S. Knaak [67] discussed the thermo-mechanical properties of carbon, glass and Kevlar fibre reinforced epoxy composites at cryogenic temperatures and purposed future developments of thermoplastics that would enhance the properties of fibre composites.

S. Yang et al., [68] experimentally investigated the fracture and impact properties by taking the composite laminates of novel Auxetic Kevlar. Further, the treatment of polyurethane was done on Kevlar and were compared with the Kevlar that was not treated. The fabrication of the composite was done with the vacuum infusion process by considering short nylon fibres having different lengths and densities. In order to determine the fracture properties, double cantilever beam configuration was considered. It was concluded that both the fracture toughness and the initiation toughness was increased by 225% and 557%, respectively, when the Auxetic Kevlar was flocked. Moreover, when compared to woven counterpart, a reduction in the damaged area was observed in the Auxetic Kevlar during Impact Testing.

R. Kapoor et al., [69] investigated the high strain rate compression response of Kevlare fibre reinforced polypropylene (PP) composites, experimentally. The fabrication of laminates (8 and 24 layers) for Kevlar/PP composite was done by vacuum assisted compression molding technique. Further, the interfacial property between Kevlar fiber and PP resin was improved by adding Maleic anhydride grafted-PP to PP. Split Hopkinson pressure bar was used to determine the properties at high strain rates ranging from 1370 to 6066 s-1. The comparison of the behaviour of PP resin with epoxy was done and found to be different. Further, in order

to obtain the mechanical properties, stress-strain relations at high strain rates were obtained. Moreover, the failure mechanisms such as, shear fracture, fiber failure and delamination were analysed by scanning electron microscopy (SEM).

A. K. Bandaru et al., [70] performed a ballistic test of composite armors which are thermoplastic based and made up of Kevlar/ Propylene (PP). The standard for the blastic test used was NIJ-STD 0106.01 Type IIIA. Different 2D and 3D shapes of Kevlar fabrics were produced and a compression molding technique was to form composite armor panels. It was analysed that when maleic anhydride grafted PP, a coupling agent was added, there was an improvement in the interfacial property between Kevlar and PP. It was observed that in comparison to thermoset based laminates, there is a reduction in density for thermoplastic based composites. Different armor panels were consider in order to impart the ballistic impact tests with a full metal jacket of 9mm. It was concluded that there was an increment in the damage for 2D armor when compared to 3D armor by 2.4-7%. The failure modes were simulated by using ANSYS AUTODYN v. 14.0.

G. Cai et al., [71] developed a bending fatigue test apparatus for fiber materials, in order to perform bending fatigue tests. A Xenon lamp irradiation system and a temperature control system were installed in the test apparatus. Kevlar 49 and PBO fibres were considered for the performance of bending fatigue tests. It was observed that the tests for the fibres were strongly dependent on temperature and light irradiation. It was concluded that when the temperature increased, the fatigue life decreases. Further, on comparison, it was observed that the fatigue strength of fibres without light irradiation was higher that that of with light irradiation.

A. Russelle and N. Naganambi, [72] conducted an finite element analysis of the tail drive shaft. Three cases, a damaged, undamaged and patched models were considered for the analysis of the deformation, stress and strain. It was observed that for the patch model, the deformation, stress and strain were reduced. It was concluded that the patch can be one of the solution for the repair of the damaged part at the critical time.

S. C. Woo and T. W. Kim, [73] used an acoustic emission (AE) and a split-Hopkinson pressure bar (SHPB) and considered a carbon/Kevlar hybrid composite in order to study the failure characteristics, when the composite is subjected to high strain-rate compressive loading. A compressive test, considering high strain rates (1002-1941 s-1) was performed and

the specimens that were taken were of cylindrical shape and were further located between the transmitted and incident bars. In order to monitor the duration of the test, the specimen was connected to the AE signals. Further, the scanning electron microscopy and the optical microscopy were used to observe the failure mechanism.

B.S. Yilbas and S.S. Akhtar, [74] used a finite element code in order to predict the thermal stress field, when the Kevlar laminates are cut with a laser. A thermocouple data is used to validate the temperature predictions. The scanning electron and optical microscopes are incorporated and the examination of the cutting section was done, in order to analyse the morphological changes. Due to the formation of thermal compression, the values of von Mises stress are observed to be higher at the midthickness and at the cutting edges of the Kevlar laminate.

U. K. Fatema and Y. Gotoh, [75] used an iodine aided palladium free catalyzation process in order to do electroless nickel plating on Kevlar fiber. In order to impart iodide component into the near fiber surface, the treatment of iodine–potassium iodide aqueous solution was done on Kevlar. The silver nitrate aqueous solution was treated with doped iodine in order to obtain the silver iodide particles and further these particles were reduced to silver metal particles. Further, a nickel layer, in order to resist the alkaline corrosion tests, tape peel-off and sonication was deposited on the fibre surface. It was observed that there was an increment in electrical conductivity, ferromagnetic properties and tensile strength of the plated fibres.

A. Srivastava et al., [76] used silica particle based shear thickening fluid (STF) on Kevlar woven fabrics, in order to improve the Impact energy absorption capacity. A study of impact energy absorption, yarn pull out force and STF add-on% is done by considering the influence of silica concentration and padding pressure. It was observed that the impact energy absorption increases and the STF add-on% reduces with the increment of padding pressure.

D. Micheli et al., [77] developed a material which is able to shield from electromagnetic interferences and simultaneously able to absorb mechanical shocks. The electromagnetic shielding effectiveness characterization was carried out in the range of 0.8 to 8 GHz and metallic bullets were fired (400 m/s and 1000 m/s) in order to determine the energy absorbing capability. Tiles made of hybrid multi-scale material (Carbon with Kevlar fibre plies with a polymeric matrix reinforced by carbon nanotubes) approximately of 3.5 mm thickness are

taken for the test. It was concluded that high energy impacts were absorbed by a light tile made up of composite material with local delamination of the layered structure.

M. Su et al., [78] studied the macro-properties of Kevlar fiber/bismaleimide composites and the Kevlar fibers on the interfacial adhesion are considered for analysing the effect of oxygen-plasma treatment. It was observed that by changing the morphology and chemistry of the surfaces of the fibers, the interfacial adhesion was significantly affected from oxygen-plasma treatment, which leads to the improvement of the dielectric properties of composites, water resistance and interlaminar shear strength. The optimum condition, 70W for 5 min, was observed by authors for treating Kevlar fiber.

S. L. Valença et al., [79] used a hand lay-up process in order to manufacture the composite plates made up from Kevlar/glass hybrid fabric and Kevlar fiber plain fabric with epoxy matrix (DGEBA). Bending, Impact and tensile tests were performed in order to obtain the mechanical properties of composites. To observe matrix and reinforcement fractures, scanning electron microscopy was used. The results for the Bending, Impact and tensile strengths came to be better for Kevlar/glass hybrid fabric.

R. B. Nath et al., [80] used a Kevlar 49 fibre with epoxy matrix in order to do the Elasto-plastic finite element analysis, when subjected to the tensile loading. An experiment is performed by using laser Raman spectroscopy and the results are further compared with the finite element results. Furthermore, the analysation of residual stresses which are present due to the curing is done. Moreover, a co-relation is obtained using experimental data.

I.F. Brown and C.J. Burgoyne, [81] examined the friction and wear behaviour at low sliding velocities under large contact pressures for Kevlar 49 sliding against aluminium. Further, the results obtained from the experiment are validated with the results from the literature. capstan discs of radii 10–80 mm is used and yarns of 1000 filaments are wound around the disc in order to perform medium scale tests. For a given severity regime, the number of cycles to failure are used to calculate the wear rate. Five orders of magnitude of load 6–40000 N were used in order to determine that the wear rate is found to be directly proportional to the applied load. Further, they obtained that the Archard wear equation can be used to express the Kevlar 49-on-aluminium abrasion.

M. Akay, [82] studied the influence of moisture and Moisture absorption behaviour of Kevlar-49/epoxy-resin laminates on the thermal and mechanical properties. Oven-curing and autoclaving were used to prepare the laminates. Higher values of moisture diffusivity and a greater amount of moisture absorption is observed due to the higher percentage of voids in the oven-cured laminates. Deterioration in mechanical properties and depression in the glass-transition temperature were caused due to Moisture absorption.

A. M. Hindeleh and Sh. M. Abdo, [83] used X-ray diffraction techniques for studying the effect of annealing on the microparacrystallite (mPC) and crystallinity size of Kevlar 49 fibres in the range 20-500°C. Until 350°C, the crystallinity remained constant, it reached its maximum value at 400°C and again it decreased at 500°C. Whereas, until 250°C the size of mPC remained constant and further at 400°C it reached its maximum value and then they decreased.

A. Mittelman and I. Roman, [84] investigated the failure modes, tensile strength and mechanical behaviour in Kevlar/epoxy (volume fraction range 0.26-0.73) composites (unidirectional) under the unidirectional load parallel load. The results calculated from the Rule of Mixture were obtained to be different than that of the measured tensile strength. The catastrophic final failure coinciding with Failure of Kevlar fibres occurred at extremely short loading intervals.

P.N.B. Reis et al., [85] predicted the best impact performance for the amount of nanoclays to be used. 1.5%, 3% and 6% of epoxy system in weight was considered in order to disperse Nanoclays Cloisite 30B. Silane treatment appropriate to the epoxy resin was done earlier to nanoclays, in order to obtain the better dispersion and an interface adhesion matrix/clay. The best performance in terms of penetration threshold and elastic recuperation was obtained with the laminates manufactured with filling of 6 wt.% of nanoclays in epoxy resin. The displacement at peak load showed the opposite tendency.

A. Bendada et al., [86] applied infrared vision on two impacted panels made of aramid–phenolic composite subjected to different spectral bands. Two methods: (1) near and short-wave infrared transmittography and reflectography, and (2) mid-wave active infrared thermography were respectively used. In order to highlight the damages due to the impacts on the samples, optical methods, namely holographic interferometry and digital speckle photography are used.

J. S. Lin, [87] modified the surface of Kevlar fibre by using bromination, grafting and metalation. The fibre characterisation was done with scanning electron microscopy (SEM), intrinsic viscosity, infrared spectroscopy and tensile measurement. From the SEM micrographs, it was analysed that the untreated fibre has the smoother surface when compared to that with the surface morphology of the bromine etched Kevlar fibre. Further, with the increase of the treating time of bromine, there is a decrement in the tensile strength of the Kevlar fibre. Furthermore, it was concluded that there was an increment of 12% in the interlaminar shear strength of the bromoacetic acid-grafted Kevlar specimen and 8% for the epichlorohydrin-grafted Kevlar specimen.

CHAPTER

4 SCOPE OF THE STUDY

Kevlar finds its applications in most of the advanced systems, including manufacturing of wings of jet planes. Further, due to identified compatibility of Kevlar at cryogenic temperatures, it is also used as insulating material in the construction of superconducting devices such as high temperature superconducting motors. In addition torque tube which is used to connect between driver and to driven end in cryogenically cooled motors. Furthermore, the very low thermal coefficient of expansion of Kevlar makes it suitable for high as well as low temperature simultaneously. This indicates the endurance limits of Kevlar due to fatigue loading (Thermal) are large. Hence studies on the effect of mechanical as well as thermal loading on the Kevlar would benefit the development of measuring and utility devices both at room and cryogenic temperatures. Further, power to weight ratio can be enhanced significantly with the use of Kevlar where power consumption is off-grid.

CHAPTER

5 OBJECTIVES OF THE STUDY

In the present work, the thermo-mechanical properties of Kevlar composites at room temperature and at cryogenic temperature are investigated. Further, the failure of Kevlar due to the propagation of cracks at room temperature and at cryogenic temperatures is predicted using Extended Finite Element Method (XFEM). The main objective of this research is to know about the behaviour of Kevlar fibre at room and cryogenic temperatures. This work may help the researchers to analysis the amount of stress a Kevlar fibre can sustain. This work may also help the researchers to know about the materilas that must be use for self healing purposes. Kevlar may also be made self healed by adding some material in the form of liquid or semi liquid. Hence, in the current research work following prospects are considered and evaluated:

1. Estimated the amount of stress a Kevlar specimen can withstand at room as well at cryogenic temperatures.
2. Estimated the amount of elongation a Kevlar specimen can bear at room as well at cryogenic temperatures. This elongation is estimated in the form of maximum inplane principal strain.
3. Estimated the amount of energy a Kevlar specimen can store while loading. This energy is known as the strain energy.
4. Estimated the strain energy density (strain energy per unit volume).
5. Estimated the stress concentration zones at the crack tip under various loading conditions.

CHAPTER

6 RESEARCH METHODOLOGY

Two-dimensional 50X30mm extended finite element (XFE) meshed models of Kevlar-49/Epoxy specimen with an edge crack, as shown in Figure 16 are used for analysing the crack behaviour in a commercial code ABAQUS. A 4-node quadrilateral mesh with mesh size of 2mm is considered for obtaining the results. A 5mm crack is initially created and further the boundary conditions (fixed at one end) and uniaxial tensile loads of 100 MPa to 1000 MPa (other end) are applied as shown in Figure 15. Considering Kevlar-49/Epoxy to be isotropic, Young's Modulus (E) Kevlar specimen at room temperature (298 K) and cryogenic temperature (76 K) is 80 GPa and 99.4 GPa respectively [21], [66].

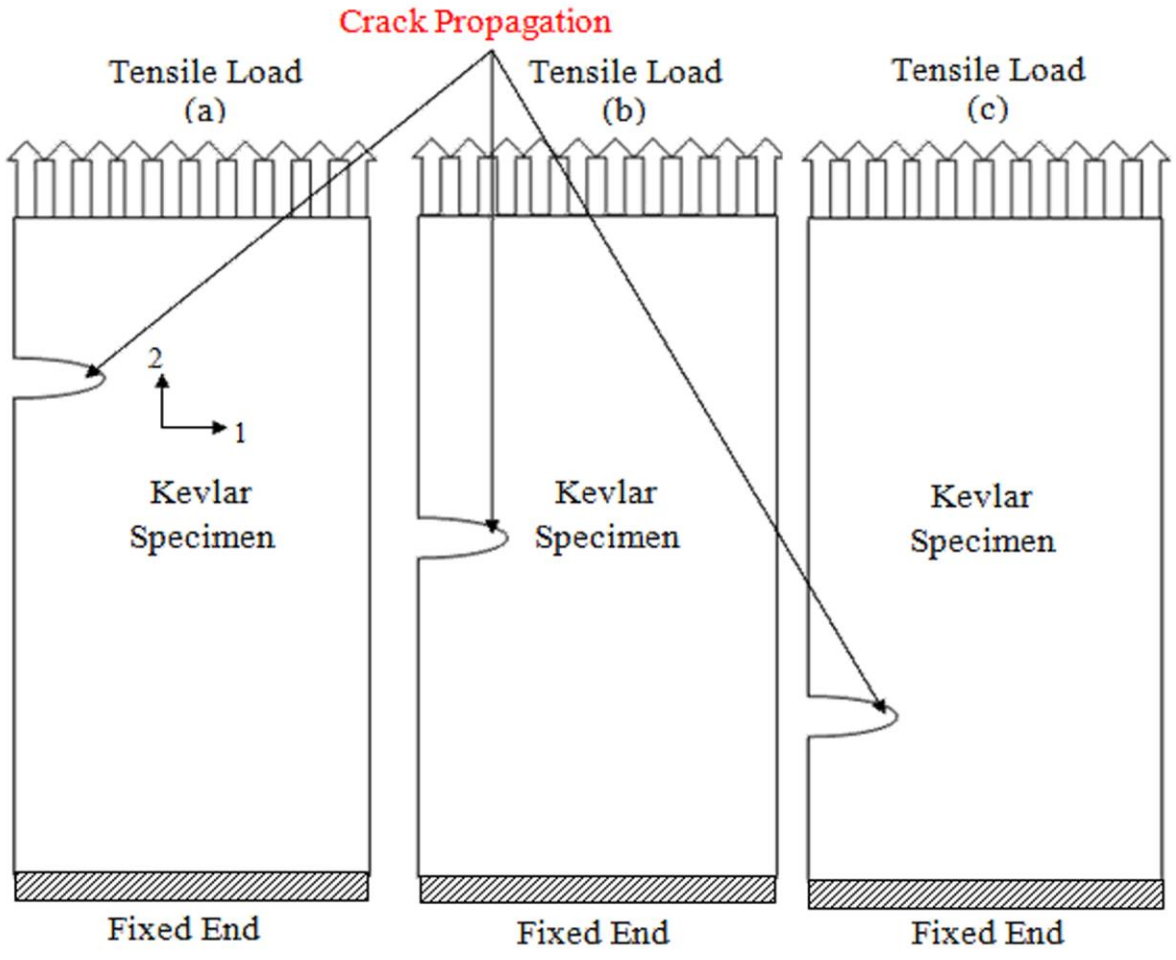

Figure 15 Schematic model of the Kevlar specimen (a) crack towards the loading end; (b) crack at the mid position; (c) crack towards the fixed end.

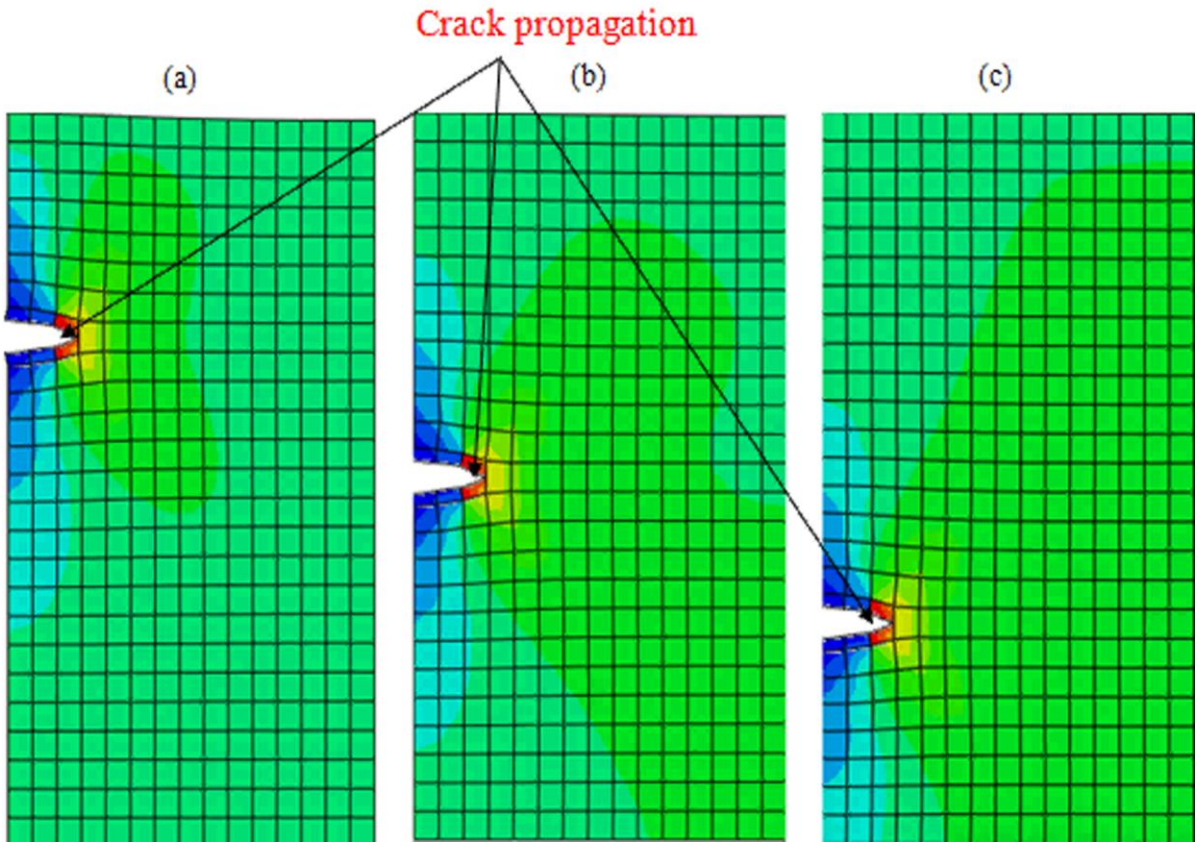

Figure 16 Computational model of the Kevlar specimen (a) crack towards the loading end; (b) crack at the mid position; (c) crack towards the fixed end.

6.1 2D Crack Modeling in Abaqus/CAE 6.13

6.1.1 Part Modeling

1. From the module section, select Part. Click Create Part, Enter name as Specimen 1, select Modeling space as 2D planar, Type as Deformable and Base Feature as Shell and enter Approximate Size as 200. Click Continue.
2. Use a rectangle tool to draw a rectangle (50×30) mm. Click Done.

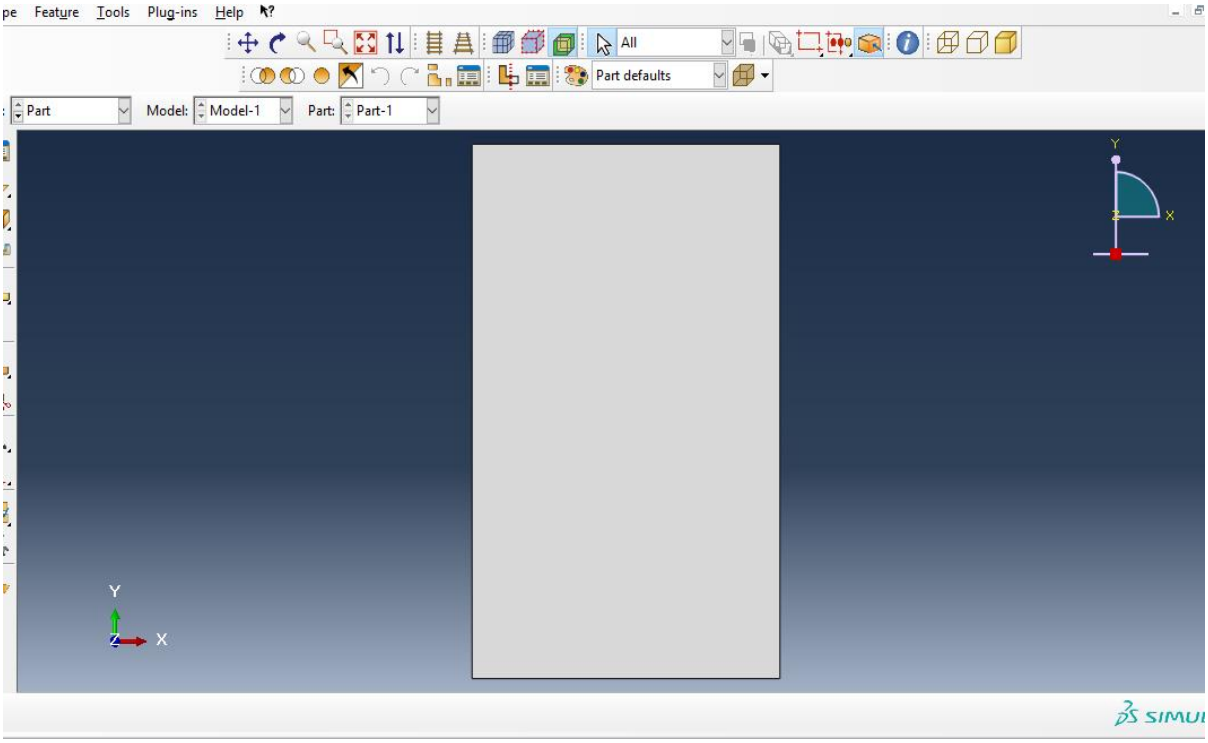

Figure 17 Finite element model of Kevlar specimen.

6.1.2 Assign Material Properties

1. Select Property from the module section. Enter name as Kevlar with epoxy resin. Click on Mechanical, then Elasticity and then Elastic.

   Enter Young's modulus as 99.4 GPa and Poisson's ratio as 0.34. Click on Mechanical, then Damage for Traction Separation laws and then Maxps Damage. Enter a value 1.15 GPa. Select the Suboptions menu, click on Damage Evolution. Enter Displacement at Failure as 0.5. Click Ok.
2. Click on Create Section. Name as xyz. Accept the default settings by clicking Continue. Select Kevlar with epoxy resin as material and click Ok.
3. Click on Assign Section. Select the specimen. Click Done. Accept the default settings and click Ok.

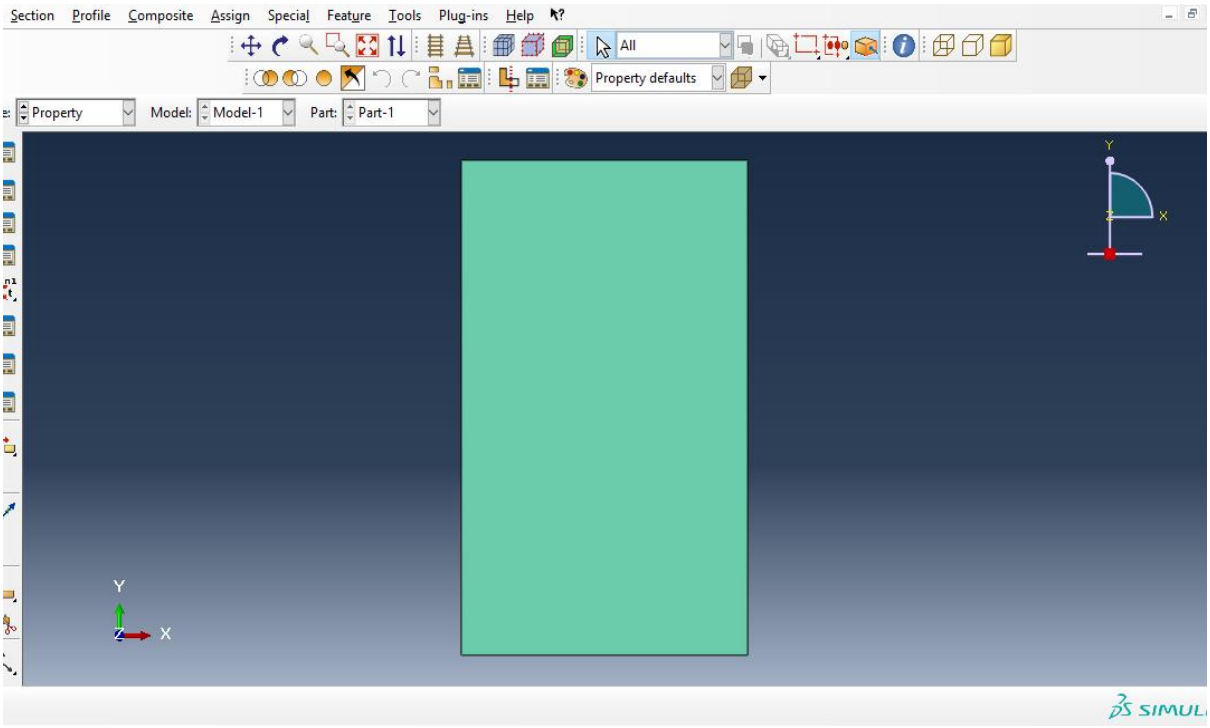

Figure 18 Finite element model of Kevlar specimen after assigning the section.

4. Select Assembly from the module section, then click Create Instance. Select the default settings and click Ok.
5. Select step from the module section, then click create step. Select default settings and click Ok.

6.1.3 Applying Loads and Boundary Conditions:

1. Click Create Load. Enter name as ‘TopPressure’, Select Category as Mechanical, select Types for Selected Step as Pressure. Click Continue. Select the top edge of the specimen. Click Done. Enter -5000 as Magnitude and Click Ok.
2. Click Create Boundary Condition. Enter name as Fixed, select Step as Initial, select Category as Mechanical, and Types for Selected Step as Displacement/Rotation and click Continue. Click on the bottom edge of the specimen and click ‘Done’. Set U1, U2 and UR3 to zero and click Ok.
3. Repeat step 4 for the top, right and left edges of the specimen, but U2 should not be set to zero. Only U1 and UR3 must be set to zero.

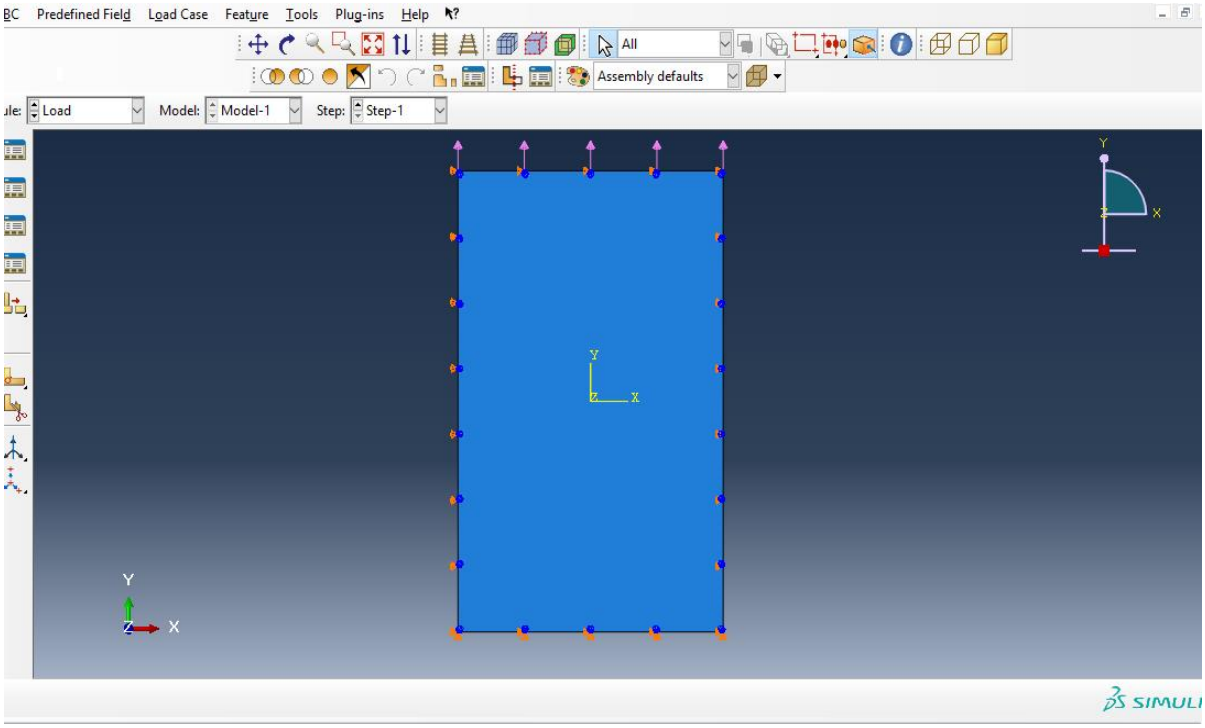

Figure 19 Application of load and boundary conditions on Kevlar specimen.

4. Expand Field Output Requests; double click on F-Output-1. Expand Strains and click on the box next to total strain components. Similarly expand the Failure/Fracture options and click on the box next to PHILSM, Level set value phi and click Ok. This will allow you to view the level set function defining the crack.

6.1.4 Meshing

1. Select Mesh from the module section. Select object as part, click Assign Mesh Controls. Select element shape as Quad, Techniques as Free and Algorithm as Medial axis. Click Ok.
2. Click Seed Part. Enter Approximate global size as 2 and click ok
3. Click Mesh Part and click yes.

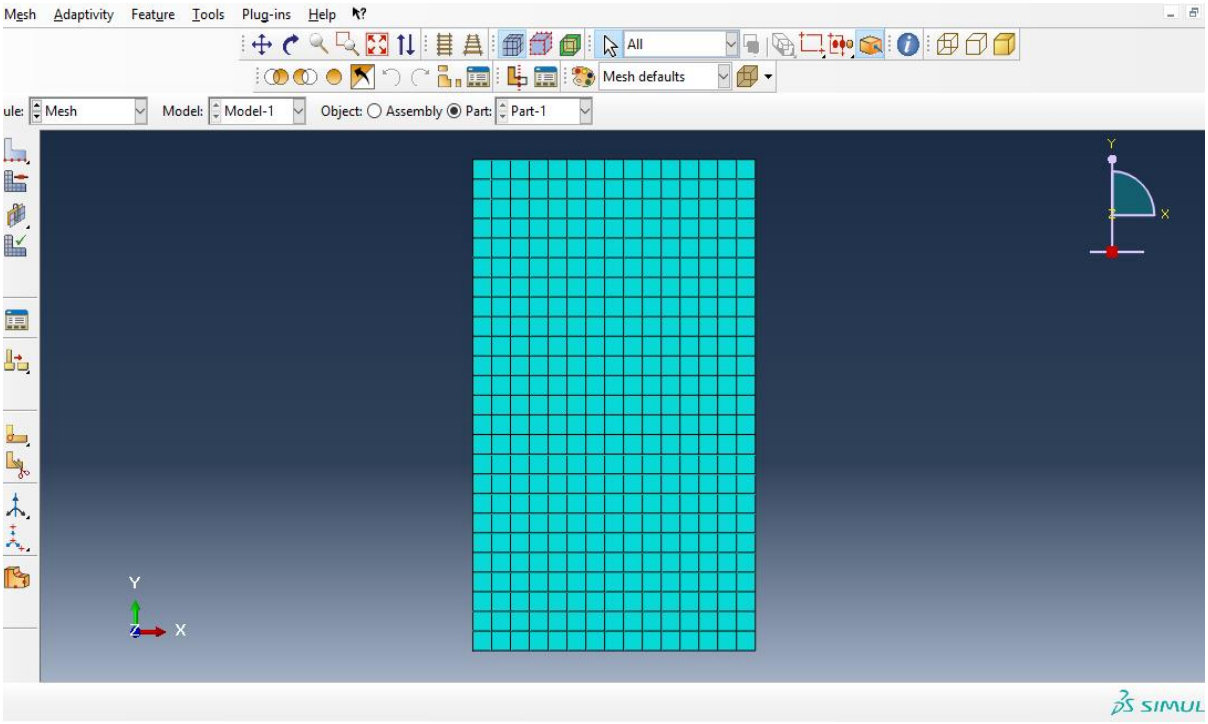

Figure 20 Meshed Finite element model of Kevlar specimen.

6.1.5 Creating the crack

1. Select Part from module section. Click Create Part. Enter name as Crack, select modeling space as 2D Planar, Type as Deformable, and Base Feature as wire and approximate size as 200. Click Continue.
2. Draw a line of approximately of 5mm. Click Done.

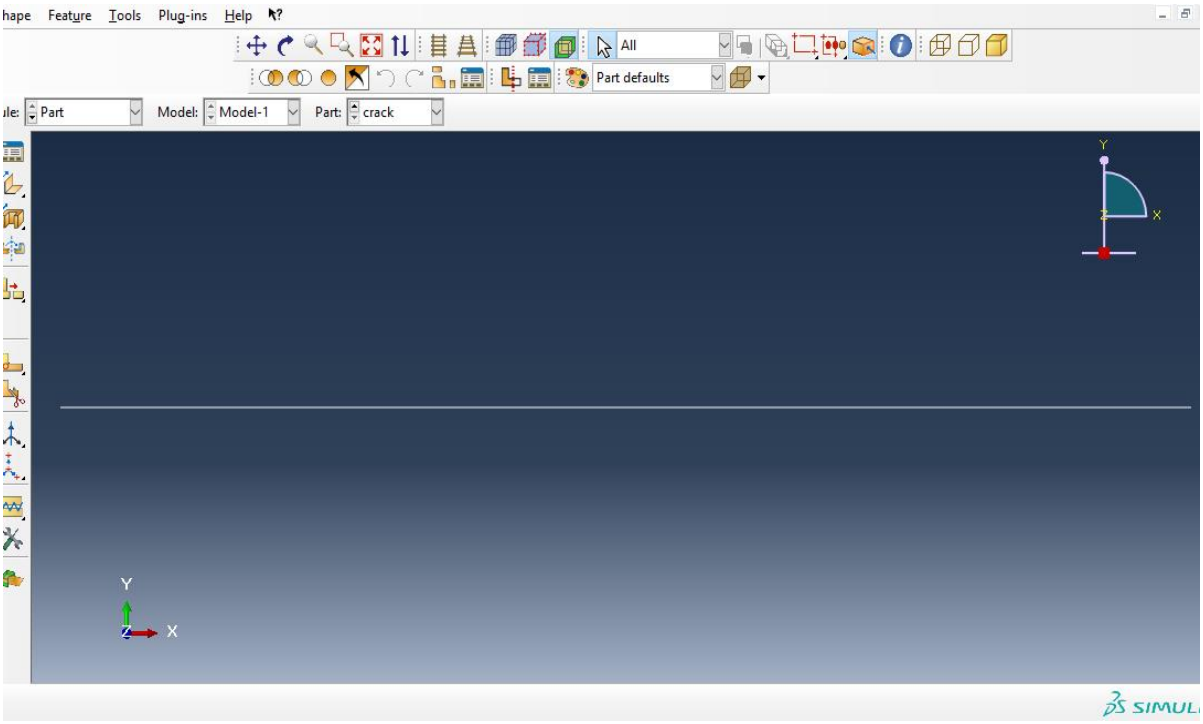

Figure 21 Determination of a crack in the form of wire.

3. Select Assembly from module section, and then click on Create Instance. Select Parts as Crack and accept the default settings by clicking Ok.
4. Select Interaction from module section. Click on special, then Crack, then Create. Name as ‘EdgeCrack’ and select Type as XFEM. Click Continue. Select the specimen, click on Crack location, click the crack generated on the specimen, click ‘Done’ and click Ok.
5. Select Interaction, then create, select the step as initial and Types of Selected Step as XFEM crack growth. Click Continue and then click Ok.

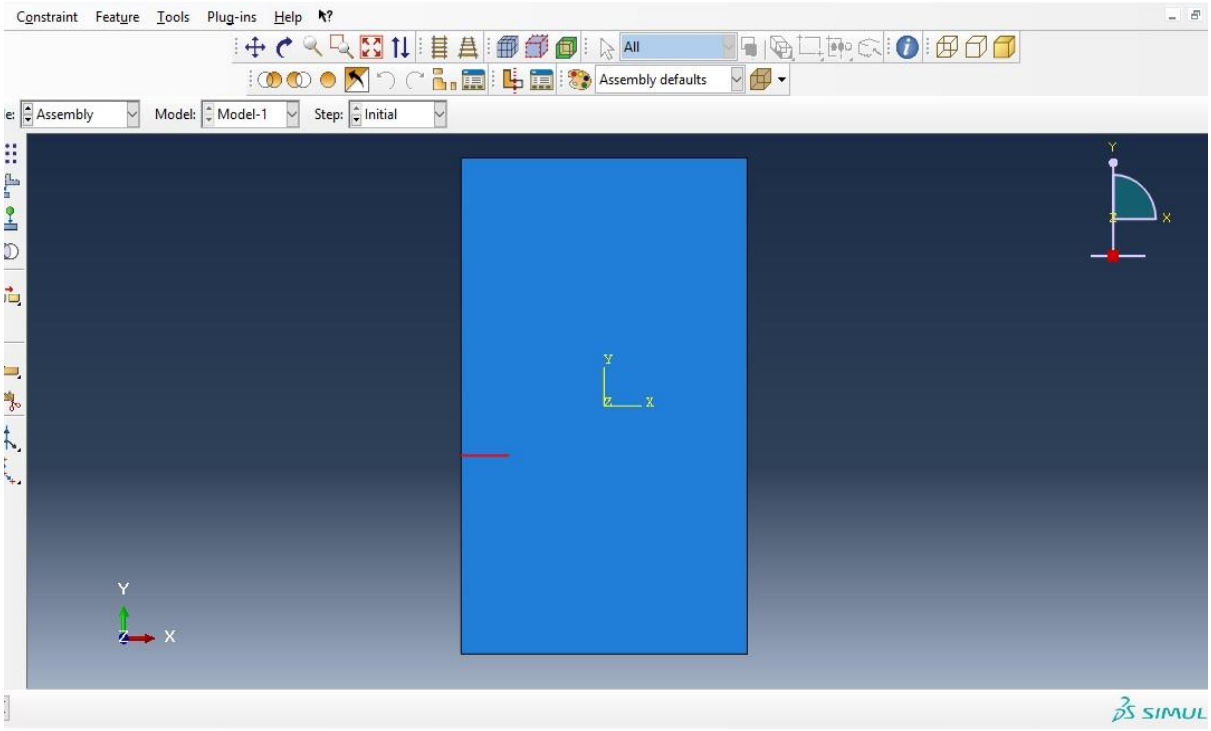

Figure 22 Edge crack interaction with Kevlar specimen.

6.1.6 Solving the Problem

1. Select Job from the module section. Click on Job Manager, click on Create, Enter the name as Crack2D, click continue.
2. Accept the default settings by clicking Ok.
3. Click on submit.
4. When under the status, completed will display, click on Results to view the results.

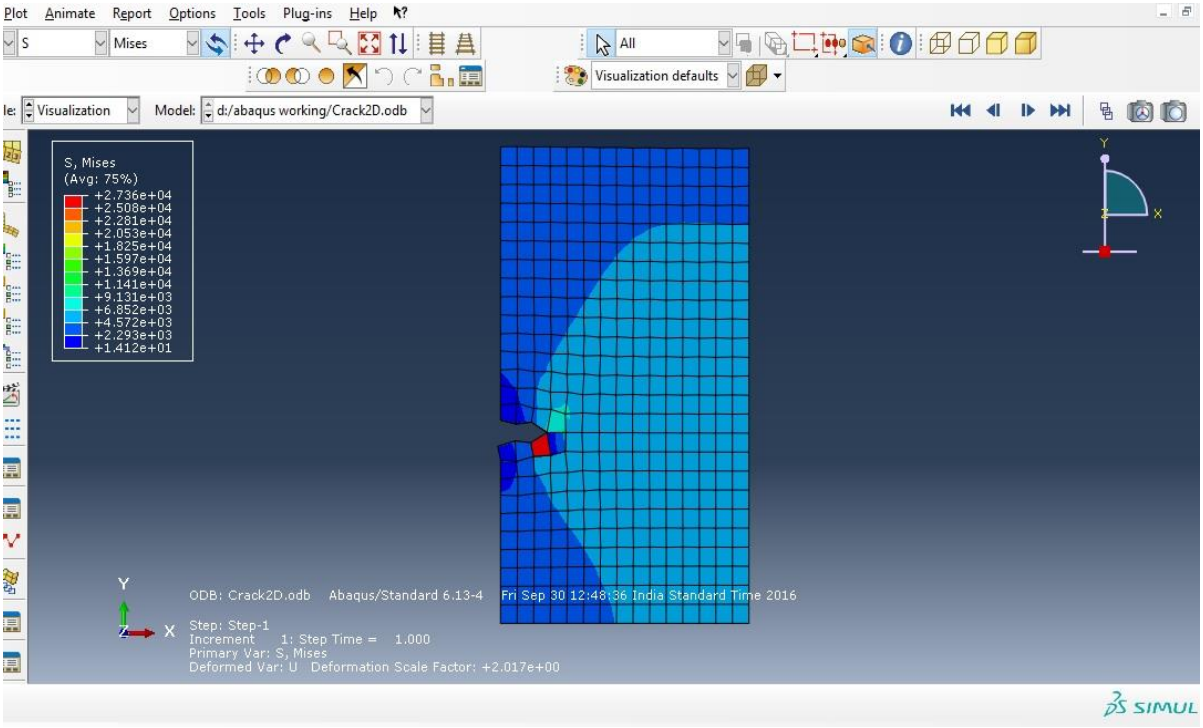

Figure 23 Determination of Von Mises stress for the Kevlar specimen.

CHAPTER

7 RESULTS AND DISCUSSIONS

The mechanical characterization of Kevlar at room and crogenic temperatures has been show in the coming sections. Further, the variation of Von Mises stress, Maximum inplane strain, strain energy and strain energy density obtained from extended finite element modeling with respect to the width of the Kevlar-49/Epoxy specimen has been shown. Furthermore, the computational results are validated from the analytical relations as shown below.

- Von Mises Stress

As the specimen is considered to be two dimensional, therefore the Von Mises stresses obtained were calculated by

$$\sigma_v = \sqrt{\sigma_{11}^{\,2} - \sigma_{11}\sigma_{22} + \sigma_{22}^{\,2} + 3\sigma_{12}^{\,2}}$$

Where σ_v is the Von Mises Stress, σ_{11} and σ_{22} are the normal stresses in 1 and 2 direction respectively, as shown in Figure 15 and σ_{12} is the shear stress in 12 plane.

- Maximum Inplane Strain

For the two dimensional specimen, the strains obtained were calculated by

$$\sigma_{p1}, \sigma_{p2} = \frac{\sigma_{11} + \sigma_{22}}{2} \pm \sqrt{\left(\frac{\sigma_{11} - \sigma_{22}}{2}\right) + \sigma_{12}^{\,2}}$$

$$\varepsilon_{p1} = \frac{1}{E}\left(\sigma_{p1} - \nu\sigma_{p2}\right)$$

Where σ_{p1} and σ_{p2} are maximum and minimum inplane principal stresses respectively, ε_{p1} is the maximum inplane principal strain and ν is the poisson's ratio.

- Strain Energy

The energy which is stored under deformation is known as the strain energy. For a two dimensional elastic case, the strain energy can be calculated from:

$$U = \sum \frac{1}{2}\sigma\varepsilon$$

Where U is the strain energy function.

- Strain Energy Density

A stored energy in an elastic material is basically referred to as strain energy density that is defined as strain energy per unit volume. For a two dimensional case, the strain energy density function is obtained by the following relation.

$$W = \frac{1}{2}\left(\sigma_{11}\varepsilon_{11} + \sigma_{22}\varepsilon_{22} + \sigma_{12}\varepsilon_{12}\right)$$

Where W is the strain energy density function, ε_{11} and ε_{22} are the the normal strains in 1 and 2 direction respectively and ε_{12} is the shear strain in 12 plane.

7.1 Mechanical Characterization of Kevlar at Room Temperatures

The results of three cases of a Kevlar specimen subjected to a uniaxial tensile loading obtained from the finite element solutions are considered in this section. The three cases are: 1) Crack towards the loading end, 2) Crack at the mid position and 3) Crack towards the fixed end in the specimen at the room temperatures are considered.

7.1.1 Crack towards the loading end

7.1.1.1 Stress Analysis

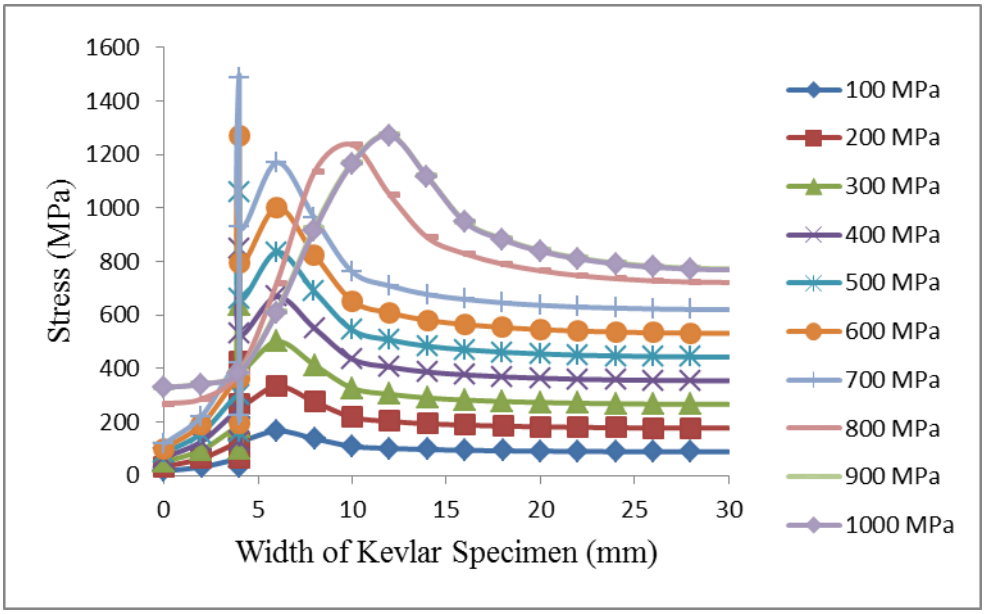

Figure 24 Stress as a function of Width of the Kevlar Specimen under deformed conditions above the crack location.

Figure 24 shows the variation of stress as a function of width of the Kevlar specimen under deformed conditions above the crack location, for the crack located near to the loading end of the specimen, at room temperature. It is observed along the width of the Kevlar specimen, as the pressure increases, the stress first increases and then it gradually decreases. The

maximum stress of 1484 MPa occurred when the pressure of 700 MPa is applied. This increment in stress is due to the effect of stress that is concentrated at the tip of the crack. At approximately 700 MPa pressure, the crack tends to propagate. Therefore at this pressure, the maximum stress occurred. After the application of pressure more than 700 MPa, the graphs are shifted towards the right hand side, that is, the crack propagates towards the right hand side.

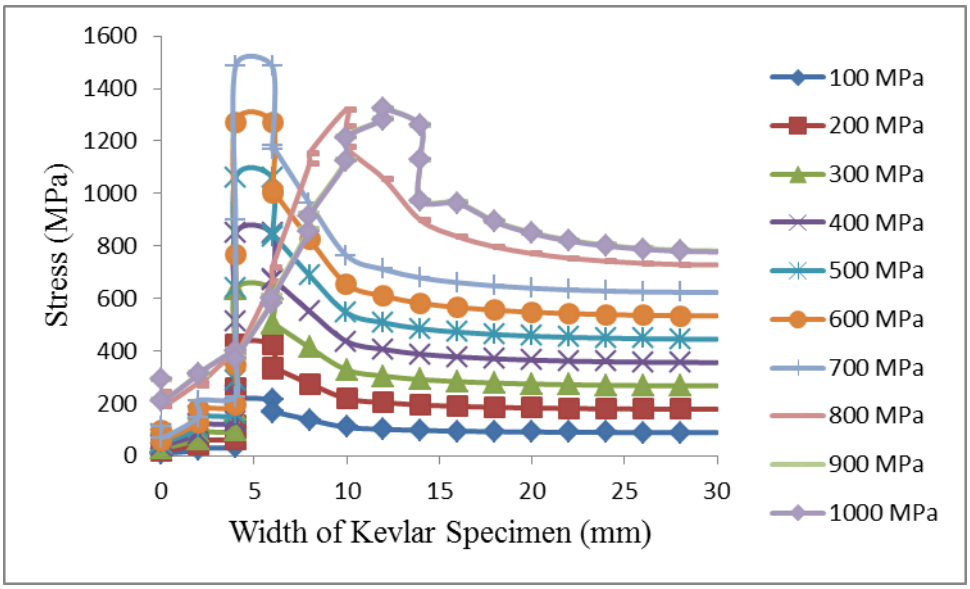

Figure 25 Stress as a function of Width of the Kevlar Specimen under deformed conditions below the crack location.

Figure 25 shows the variation of stress as a function of width of the Kevlar specimen under deformed conditions below the crack location, for the crack located near to the loading end of the specimen, at room temperature. It is observed that as the pressure increases, the stress increases. Moreover, along the width of the Kevlar specimen, the stress first increases and then it gradually decreases. On observing Figure 24 and Figure 25, it can be seen that there is an abrupt decrement for above the crack location and a gradual decrement in an initial stage for below the crack location. This difference may be due to the presence of residual stresses in the specimen.

7.1.1.2 Strain Analysis

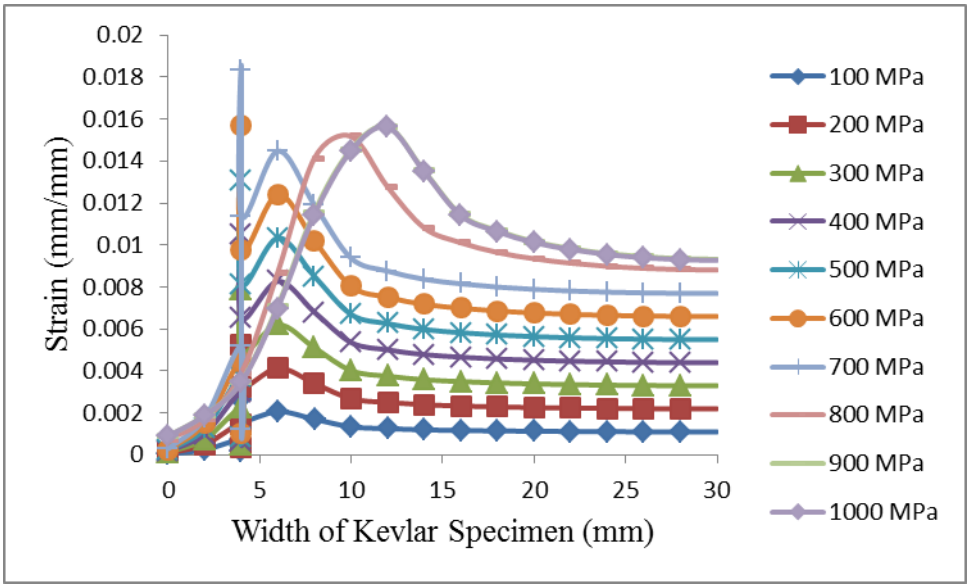

Figure 26 Strain as a function of Width of the Kevlar Specimen under deformed conditions above the crack location.

Figure 26 shows the variation of strain as a function of width of the Kevlar specimen under deformed conditions above the crack location, for the crack located near to the loading end of the specimen, at room temperature. It is observed that along the width of the Kevlar specimen, as the pressure increases, the strain first increases and then it gradually decreases. The maximum strain of 0.0183 mm/mm occurred when the pressure of 700 MPa is applied. As the stress is directly proportional to the strain, the similar type of increment is observed in the strain as observed in the stress. At approximately 700 MPa pressure, the crack tends to propagate. Therefore at this pressure, the maximum strain occurred. After the application of pressure more than 700 MPa, due to the shifting of the crack towards the right hand side, that is, the crack propagates towards the right hand side , the graphs are shifted towards the right hand side.

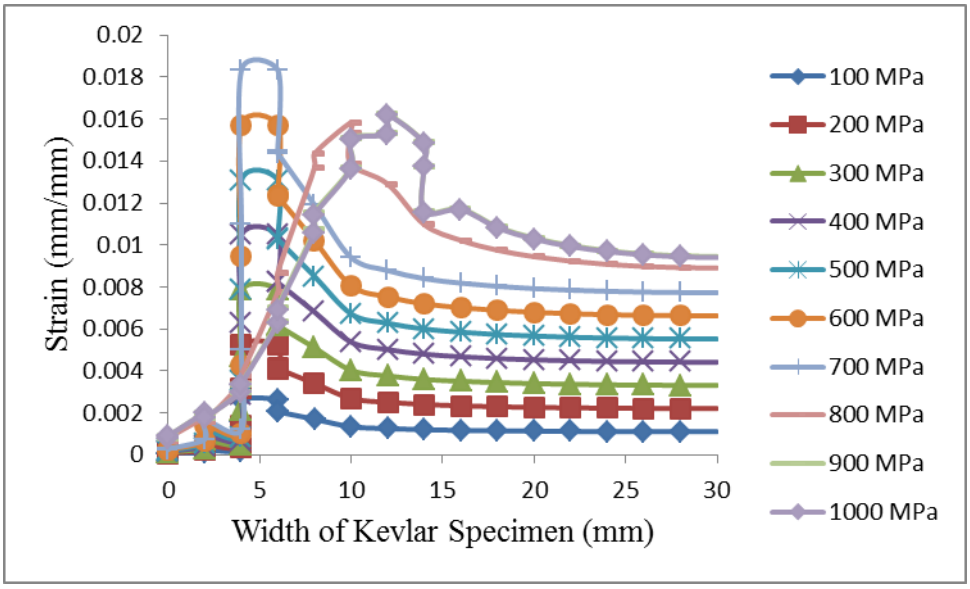

Figure 27 Strain as a function of Width of the Kevlar Specimen under deformed conditions below the crack location.

Figure 27 shows the variation of strain as a function of width of the Kevlar specimen under deformed conditions below the crack location, for the crack located near to the loading end of the specimen, at room temperature. It is observed that as the pressure increases, the strain increases. Moreover, along the width of the Kevlar specimen, the strain first increases and then it gradually decreases. As there is difference in the behaviour of stresses, therefore, the difference in the behaviour of strains for above and below the crack location occurred.

7.1.1.3 Strain Energy Analysis

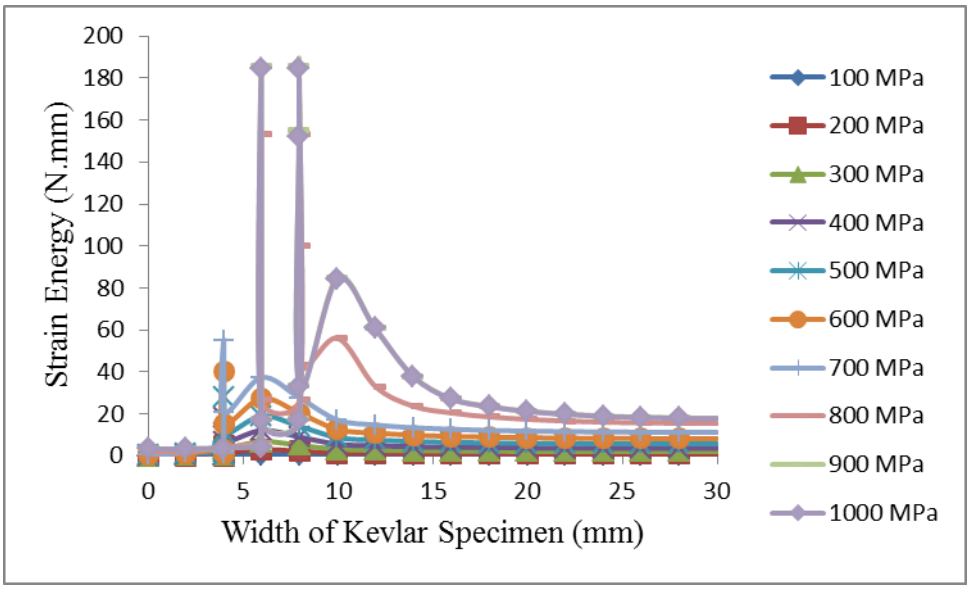

Figure 28 Strain Energy as function of Width of the Kevlar Specimen under deformed conditions above the crack location.

Figure 28 shows the variation of strain energy as a function of width of the Kevlar specimen under deformed conditions above the crack location, for the crack located near to the loading end of the specimen, at room temperature. It is observed that as the pressure increases, the strain energy increases and then decreases abruptly. The maximum amount of energy during the application of the load that the specimen could able to absorb was found to be approximately 186 N.mm at 900 MPa, nearly at the width of 6mm and the it suddenly decreases and again it reaches to its maximum value, that is, 186 N.mm at 8 mm width uptil which the material again sustained the energy and after that the crack further propagated. This may be the indication that when the crack is propagated and reached at 6mm from the start of propagation, it was able to absorb the energy uptil 186 N.mm and then it propagated further and after reaching at 8mm, it again withstand the load uptil the same energy and then further propagated.

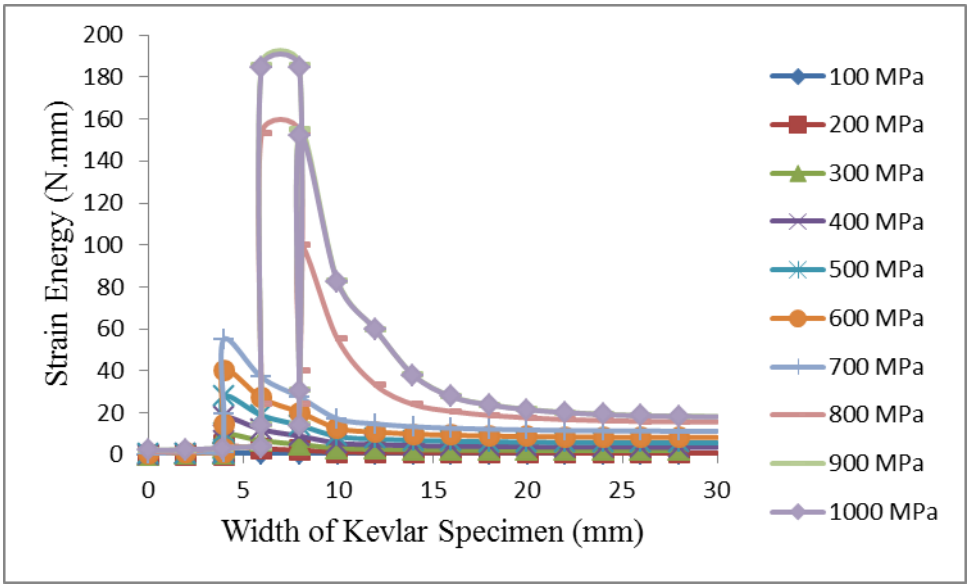

Figure 29 Strain Energy as function of Width of the Kevlar Specimen under deformed conditions below the crack location

Figure 29 shows the variation of strain energy as a function of width of the Kevlar specimen under deformed conditions below the crack location, for the crack located near to the loading end of the specimen, at room temperature. It is observed that as the pressure increases, the strain energy increases and then firstly it gradually decreases and then a sudden decrement is observed. Moreover, along the width of the Kevlar specimen, the strain energy is higher between 5-10 mm, where the edge crack is further propagated.

7.1.1.4 Strain Energy Density Analysis

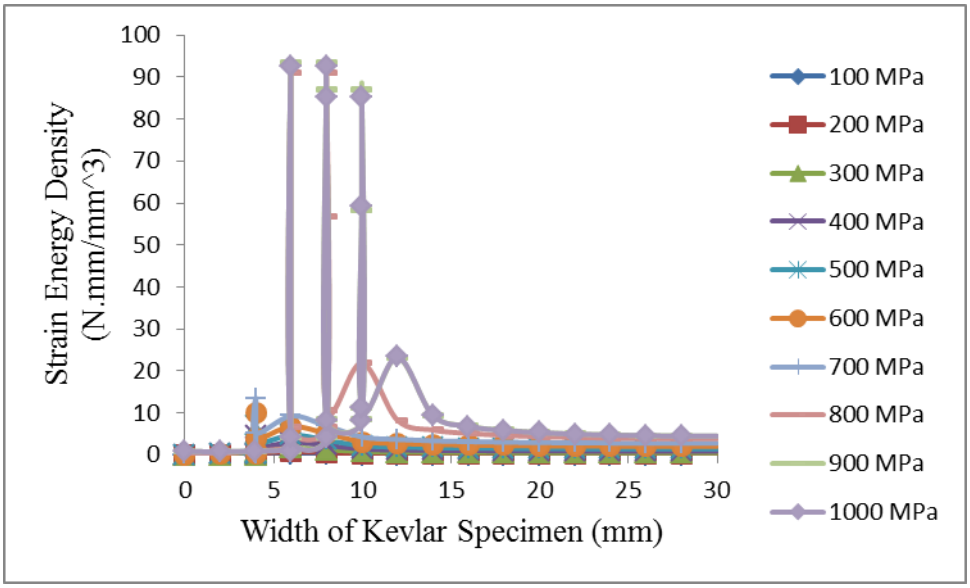

Figure 30 Strain Energy Density as function of Width of the Kevlar Specimen under deformed conditions above the crack location

Figure 30 shows the variation of the strain energy density as a function of the width of the Kevlar specimen under deformed conditions above the crack location, for the crack located near to the loading end of the specimen, at room temperature. It is observed that as the pressure increases, the strain energy density firstly increases and then a sudden decrement is observed. As the strain energy density is defined as the strain energy per unit volume. Therefore, the similar behaviour will be observed in strain energy density as in strain energy. The maximum value for strain energy density observed is 93.5 N.mm/mm^3 at approximately 6mm and 8mm width of the specimen.

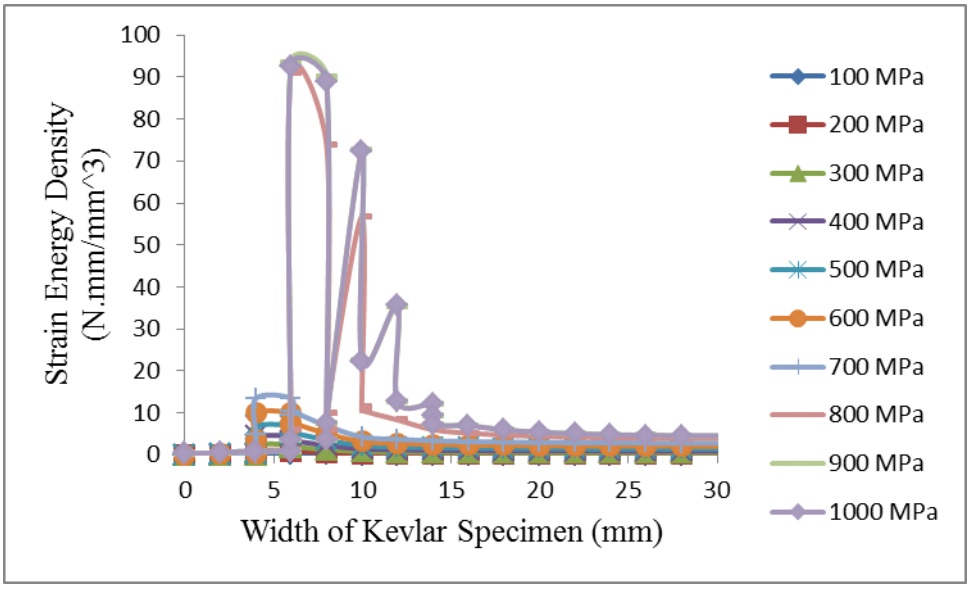

Figure 31 Strain Energy Density as function of Width of the Kevlar Specimen under deformed conditions below the crack location

Figure 31 shows the variation of the strain energy density as a function of the width of the Kevlar specimen under deformed conditions below the crack location, for the crack located near to the loading end of the specimen, at room temperature. It is observed that as the pressure increases, the strain energy density increases and then firstly decreases gradually and then a sudden decrement is observed. Moreover, along the width of the Kevlar specimen, the strain energy density is high between 5-10 mm from where the edge crack is initiated.

7.1.2 Crack at the mid position

7.1.2.1 Stress Analysis

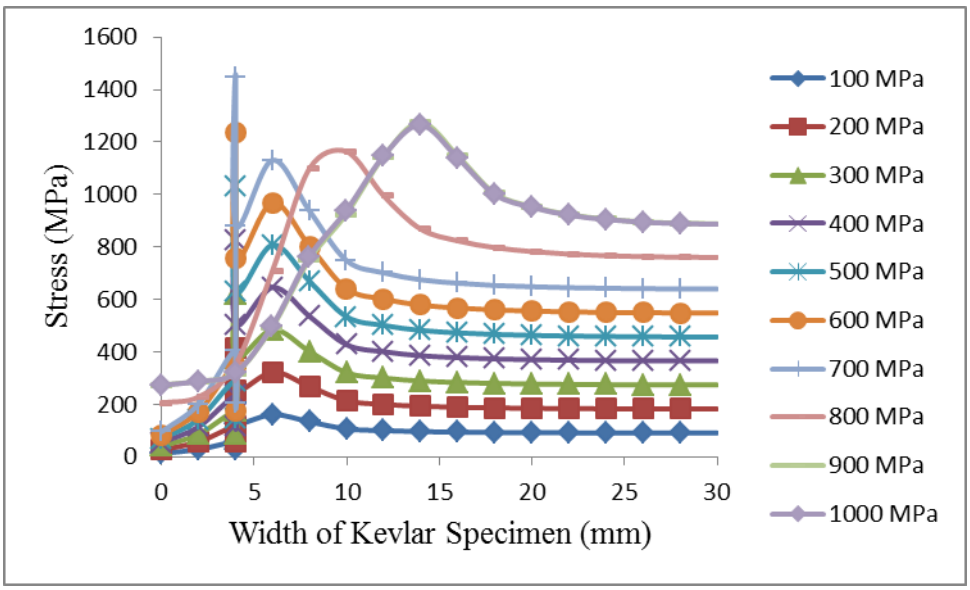

Figure 32 Stress as a function of Width of the Kevlar Specimen under deformed conditions above the crack location

Figure 32 shows the variation of stress as a function of width of the Kevlar specimen under deformed conditions above the crack location, for the crack located at the middle of the specimen, at room temperature. It is observed that, along the width of the Kevlar specimen, the stress first increases and then it gradually decreases. The maximum stress of 1445 MPa occurred when the pressure of 700 MPa is applied. This increment in stress is due to the effect of stress that is concentrated at the tip of the crack. At approximately 700 MPa pressure, the crack tends to propagate. Therefore at this pressure, the maximum stress occurred. After the application of pressure more than 700 MPa, the graphs are shifted towards the right hand side, that is, the crack propagates towards the right hand side.

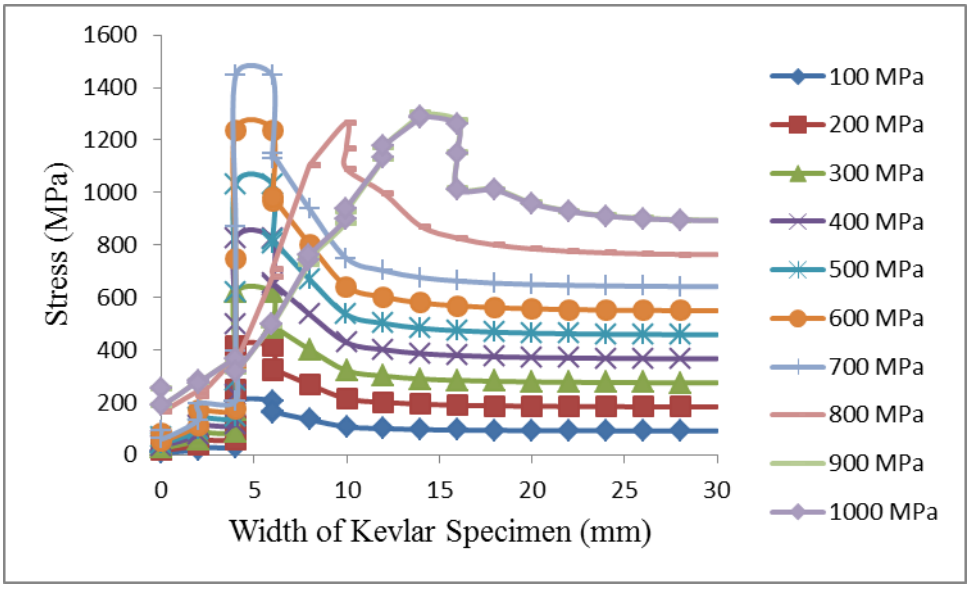

Figure 33 Stress as a function of Width of the Kevlar Specimen under deformed conditions below the crack location

Figure 33 shows the variation of stress as a function of width of the Kevlar specimen under deformed conditions below the crack location, for the crack located at the middle of the specimen, at room temperature. It is observed that as the pressure increases, the stress increases. Moreover, along the width of the Kevlar specimen, the stress first increases and then it gradually decreases. On observing Figure 32 and Figure 33, it can be seen that there is an abrupt decrement for above the crack location and a gradual decrement in an initial stage for below the crack location.

7.1.2.2 Strain Analysis

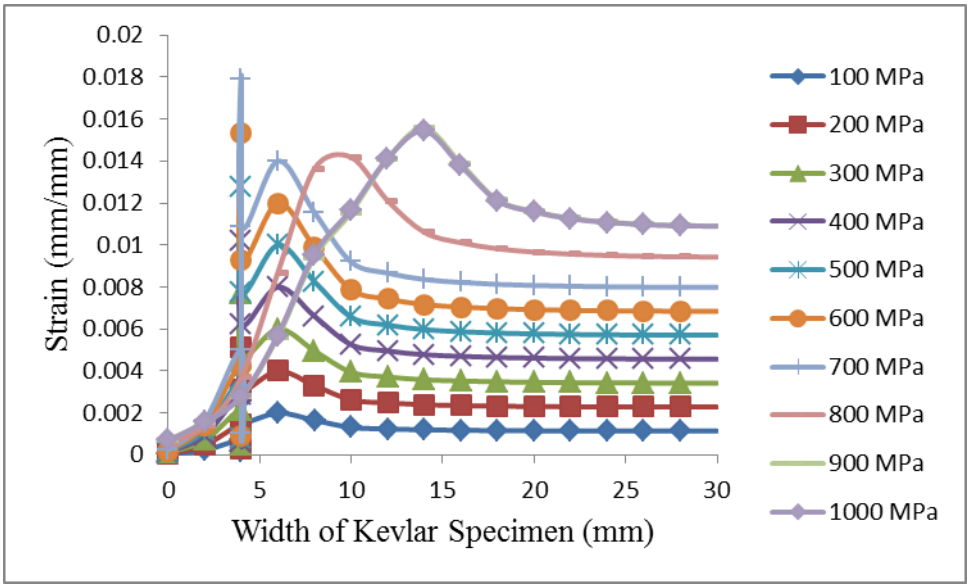

Figure 34 Strain as a function of Width of the Kevlar Specimen under deformed conditions above the crack location

Figure 34 shows the variation of strain as a function of width of the Kevlar specimen under deformed conditions above the crack location, for the crack located at the middle of the specimen, at room temperature. It is observed that along the width of the Kevlar specimen, as the pressure increases, the strain first increases and then it gradually decreases. The maximum strain of 0.0179 mm/mm occurred when the pressure of 700 MPa is applied. As the stress is directly proportional to the strain, the similar type of increment is observed in the strain as observed in the stress. At approximately 700 MPa pressure, the crack tends to propagate. Therefore at this pressure, the maximum strain occurred. After the application of pressure more than 700 MPa, due to the shifting of the crack towards the right hand side, that is, the crack propagates towards the right hand side , the graphs are shifted towards the right hand side.

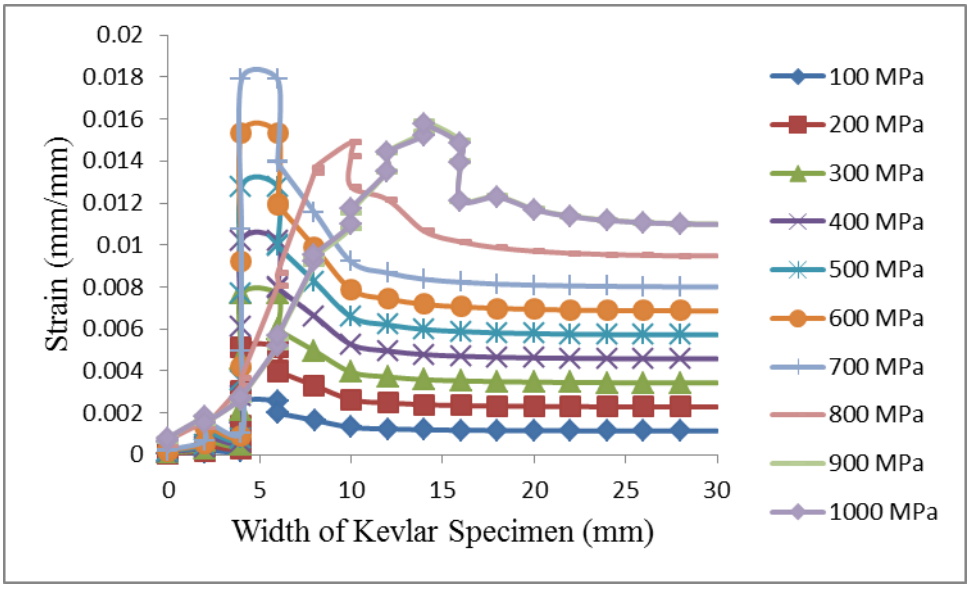

Figure 35 Strain as a function of Width of the Kevlar Specimen under deformed conditions below the crack location

Figure 35 shows the variation of strain as a function of width of the Kevlar specimen under deformed conditions below the crack location, for the crack located at the middle of the specimen, at room temperature. It is observed that as the pressure increases, the strain increases. Moreover, along the width of the Kevlar specimen, the strain first increases and then it gradually decreases. As there is difference in the behaviour of stresses, therefore, the difference in the behaviour of strains for above and below the crack location occurred.

7.1.2.3 Strain Energy Analysis

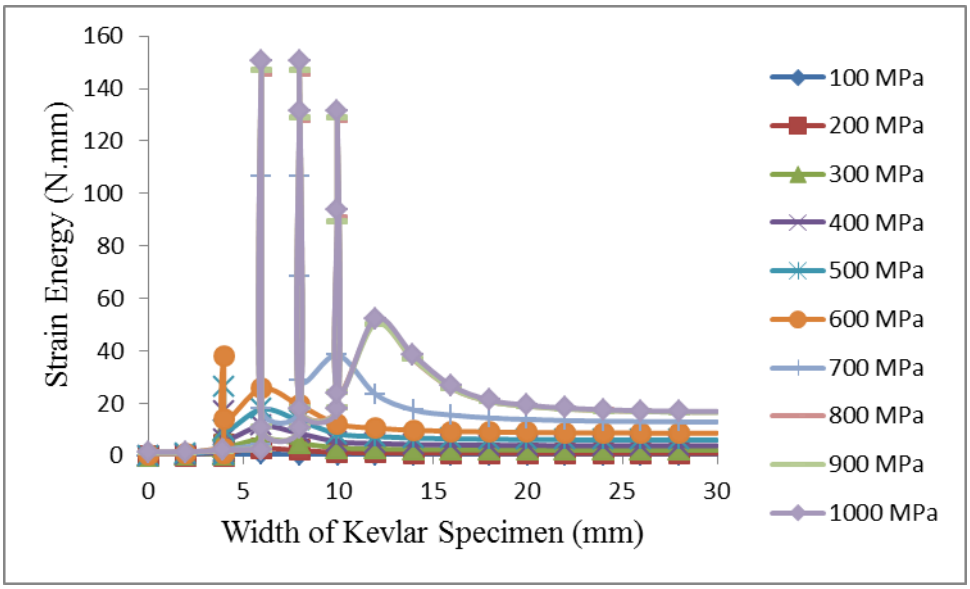

Figure 36 Strain Energy as function of Width of the Kevlar Specimen under deformed conditions above the crack location

Figure 36 shows the variation of strain energy as a function of width of the Kevlar specimen under deformed conditions above the crack location, for the crack located at the middle of the specimen, at room temperature. It is observed that as the pressure increases, the strain energy increases and then decreases abruptly. The maximum amount of energy during the application of the load that the specimen could able to absorb was found to be approximately 150 N.mm at 1000 MPa, nearly at the width of 6mm and the it suddenly decreases and again it reaches to its maximum value, that is, 150 N.mm at 8 mm width uptil which the material again sustained the energy and after that the crack further propagated. This may be the indication that when the crack is propagated and reached at 6mm from the start of propagation, it was able to absorb the energy uptil 150 N.mm and then it propagated further and after reaching at 8mm, it again withstand the load uptil the same energy and then further propagated.

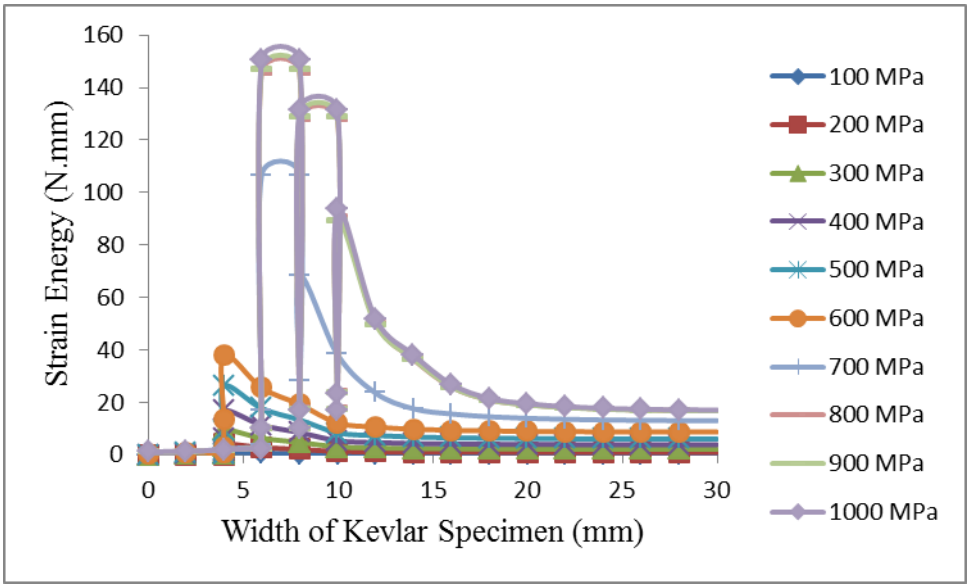

Figure 37 Strain Energy as function of Width of the Kevlar Specimen under deformed conditions below the crack location

Figure 37 shows the variation of strain energy as a function of width of the Kevlar specimen under deformed conditions below the crack location, for the crack located at the middle of the specimen, at room temperature. It is observed that as the pressure increases, the strain energy increases and then firstly it gradually decreases and then a sudden decrement is observed. Moreover, along the width of the Kevlar specimen, the strain energy is higher between 5-10 mm, where the edge crack is further propagated.

7.1.2.4 Strain Energy Density Analysis

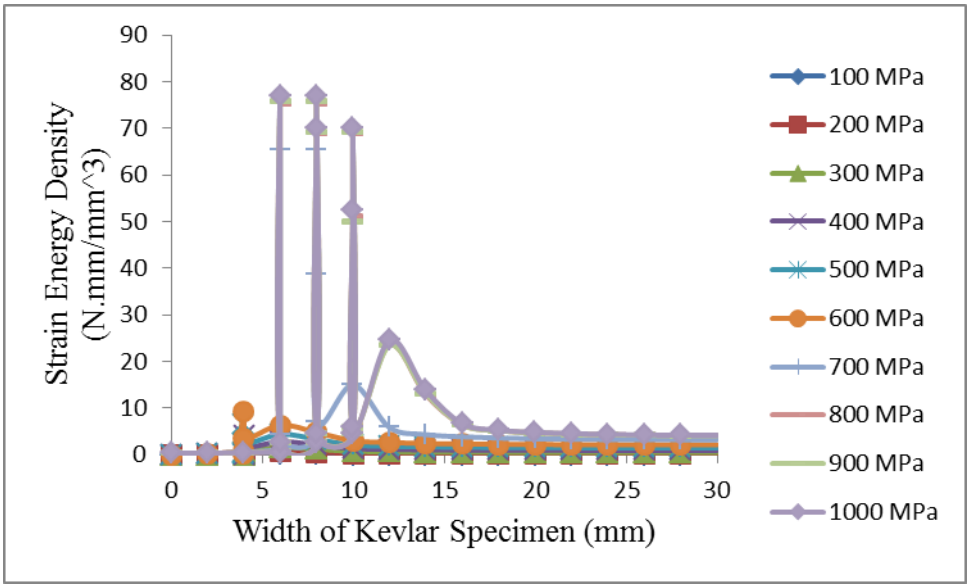

Figure 38 Strain Energy Density as function of Width of the Kevlar Specimen under deformed conditions above the crack location

Figure 38 shows the variation of the strain energy density as a function of the width of the Kevlar specimen under deformed conditions above the crack location, for the crack located at the middle of the specimen, at room temperature. It is observed that as the pressure increases, the strain energy density firstly increases and then a sudden decrement is observed. As the strain energy density is defined as the strain energy per unit volume. Therefore, the similar behaviour will be observed in strain energy density as in strain energy. The maximum value for strain energy density observed is 77 $N.mm/mm^3$ at approximately 6mm and 8mm width of the specimen.

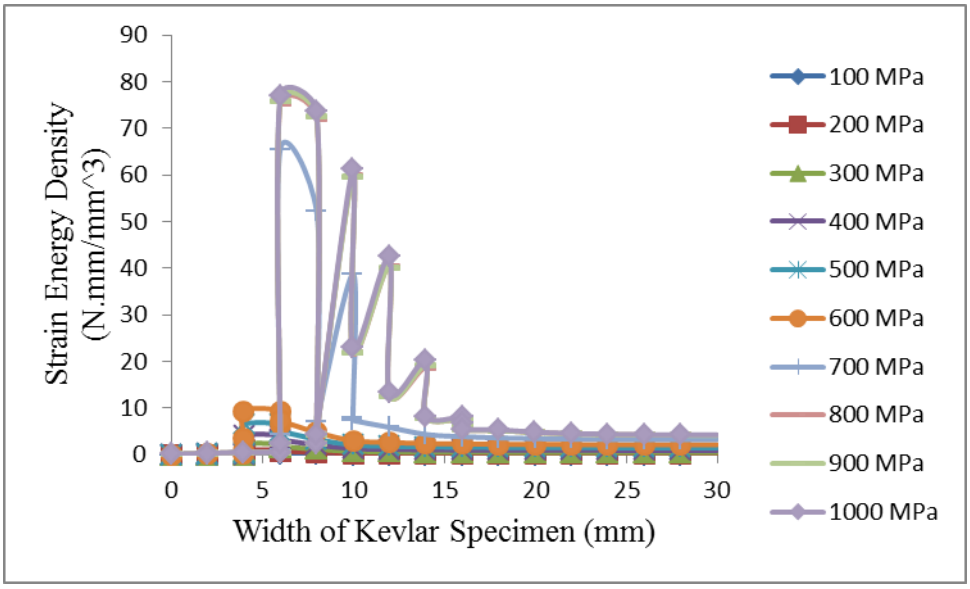

Figure 39 Strain Energy Density as function of Width of the Kevlar Specimen under deformed conditions below the crack location

Figure 39 shows the variation of the strain energy density as a function of the width of the Kevlar specimen under deformed conditions below the crack location, for the crack located at the middle of the specimen, at room temperature. It is observed that as the pressure increases, the strain energy density increases and then firstly decreases gradually and then a sudden decrement is observed. Moreover, along the width of the Kevlar specimen, the strain energy density is high between 5-10 mm from where the edge crack is initiated.

7.1.3 Crack towards the fixed end

7.1.3.1 Stress Analysis

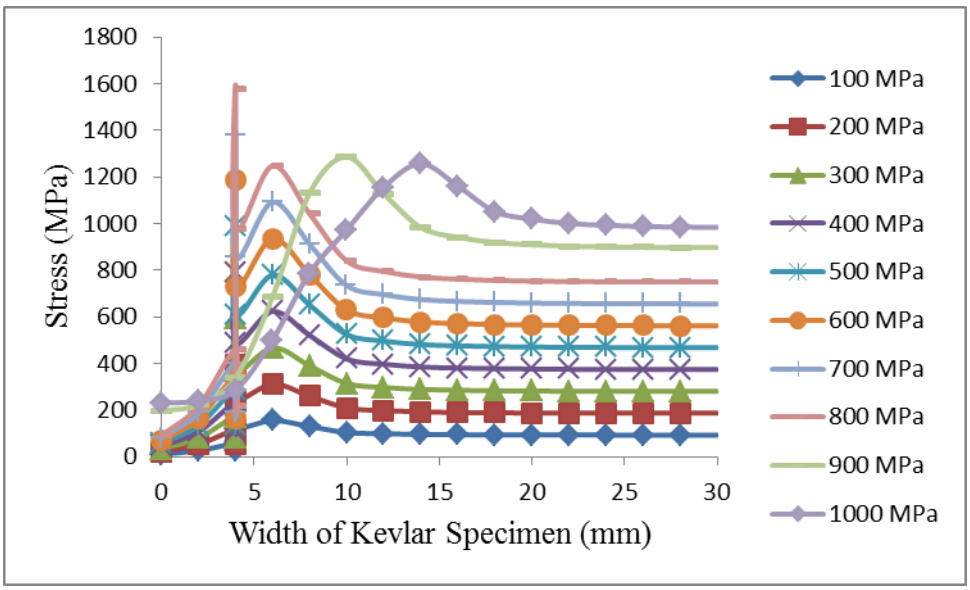

Figure 40 Stress as a function of Width of the Kevlar Specimen under deformed conditions above the crack location

Figure 40 shows the variation of stress as a function of width of the Kevlar specimen under deformed conditions above the crack location, for the crack located near to the fixed end of the specimen, at room temperature. It is observed that, along the width of the Kevlar specimen, the stress first increases and then it gradually decreases. The maximum stress of 1579 MPa occurred when the pressure of 800 MPa is applied. This increment in stress is due to the effect of stress that is concentrated at the tip of the crack. At approximately 800 MPa pressure, the crack tends to propagate. Therefore at this pressure, the maximum stress occurred. After the application of pressure more than 800 MPa, the graphs are shifted towards the right hand side, that is, the crack propagates towards the right hand side.

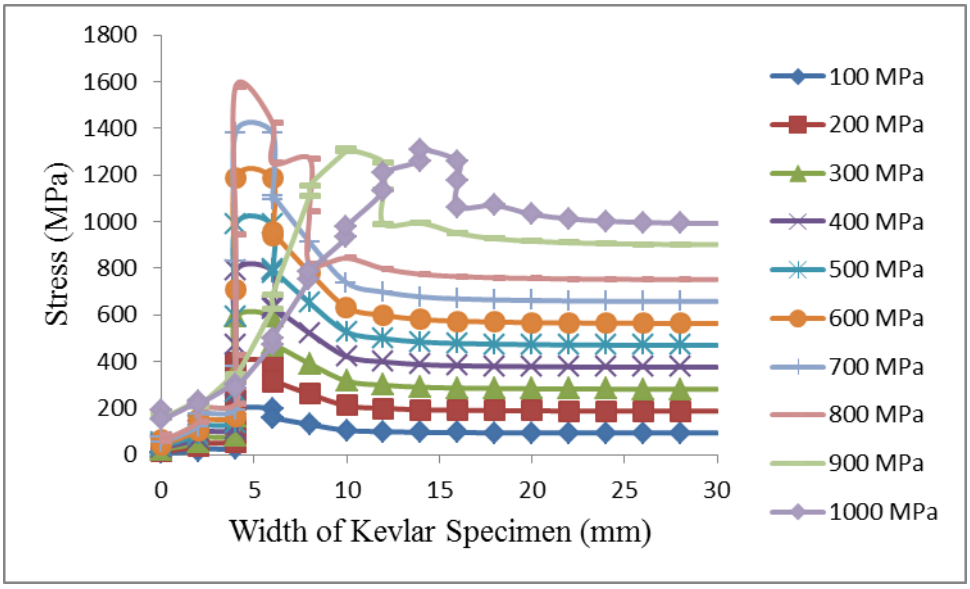

Figure 41 Stress as a function of Width of the Kevlar Specimen under deformed conditions below the crack location

Figure 41 shows the variation of stress as a function of width of the Kevlar specimen under deformed conditions below the crack location, for the crack located near to the fixed end of the specimen, at room temperature. It is observed that as the pressure increases, the stress increases. Moreover, along the width of the Kevlar specimen, the stress first increases and then it gradually decreases. On observing Figure 40 and Figure 41, it can be seen that there is an abrupt decrement for above the crack location and a gradual decrement in an initial stage for below the crack location.

7.1.3.2 Strain Analysis

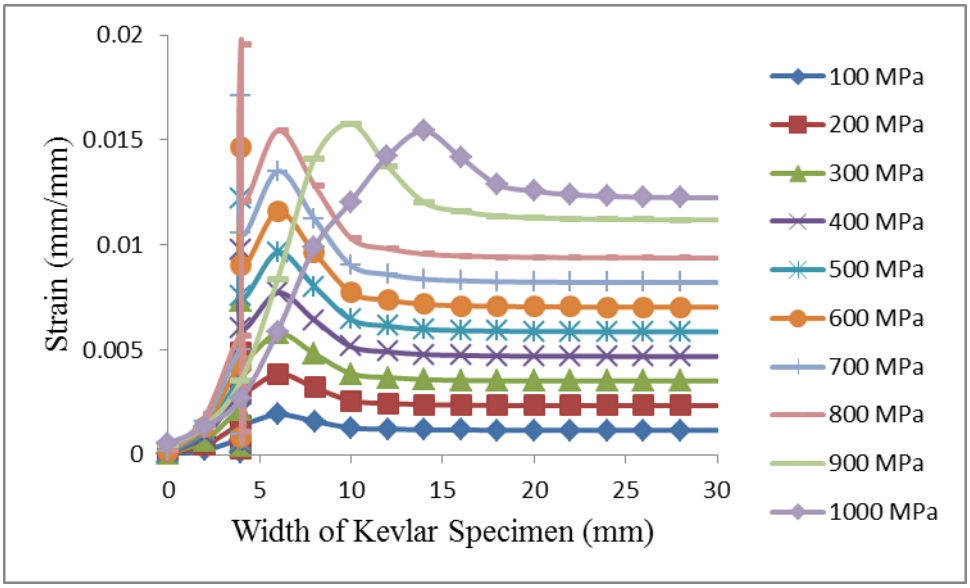

Figure 42 Strain as a function of Width of the Kevlar Specimen under deformed conditions above the crack location

Figure 42 shows the variation of strain as a function of width of the Kevlar specimen under deformed conditions above the crack location, for the crack located near to the fixed end of the specimen, at room temperature. It is observed that along the width of the Kevlar specimen, as the pressure increases, the strain first increases and then it gradually decreases. The maximum strain of 0.0196 mm/mm occurred when the pressure of 800 MPa is applied. As the stress is directly proportional to the strain, the similar type of increment is observed in the strain as observed in the stress. At approximately 800 MPa pressure, the crack tends to propagate. Therefore at this pressure, the maximum strain occurred. After the application of pressure more than 800 MPa, due to the shifting of the crack towards the right hand side, that is, the crack propagates towards the right hand side , the graphs are shifted towards the right hand side.

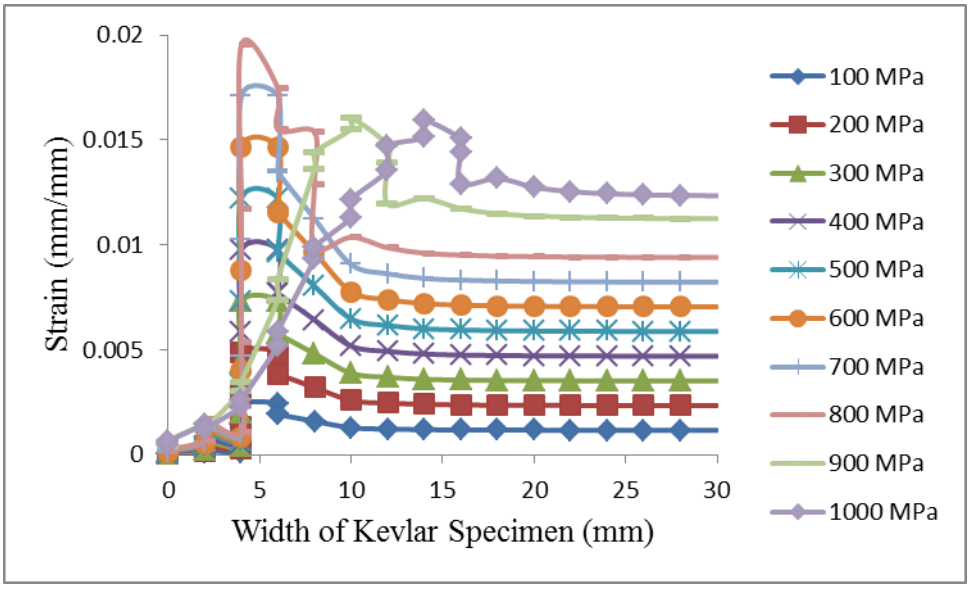

Figure 43 Strain as a function of Width of the Kevlar Specimen under deformed conditions below the crack location

Figure 43 shows the variation of strain as a function of width of the Kevlar specimen under deformed conditions below the crack location, for the crack located near to the fixed end of the specimen, at room temperature. It is observed that as the pressure increases, the strain increases. Moreover, along the width of the Kevlar specimen, the strain first increases and then it gradually decreases. As there is difference in the behaviour of stresses, therefore, the difference in the behaviour of strains for above and below the crack location occurred.

7.1.3.3 Strain Energy Analysis

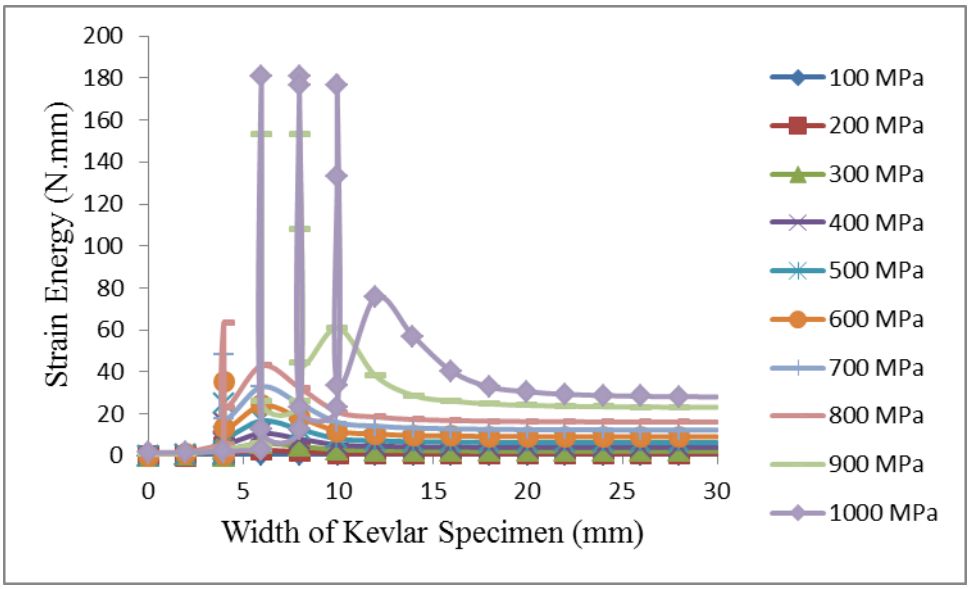

Figure 44 Strain Energy as function of Width of the Kevlar Specimen under deformed conditions above the crack location

Figure 44 shows the variation of strain energy as a function of width of the Kevlar specimen under deformed conditions above the crack location, for the crack located near to the fixed end of the specimen, at room temperature. It is observed that as the pressure increases, the strain energy increases and then decreases abruptly. The maximum amount of energy during the application of the load that the specimen could able to absorb was found to be approximately 180 N.mm at 1000 MPa, nearly at the width of 6mm and the it suddenly decreases and again it reaches to its maximum value, that is, 180 N.mm at 8 mm width uptil which the material again sustained the energy and after that the crack further propagated. This may be the indication that when the crack is propagated and reached at 6mm from the start of propagation, it was able to absorb the energy uptil 180 N.mm and then it propagated further and after reaching at 8mm, it again withstand the load uptil the same energy and then further propagated.

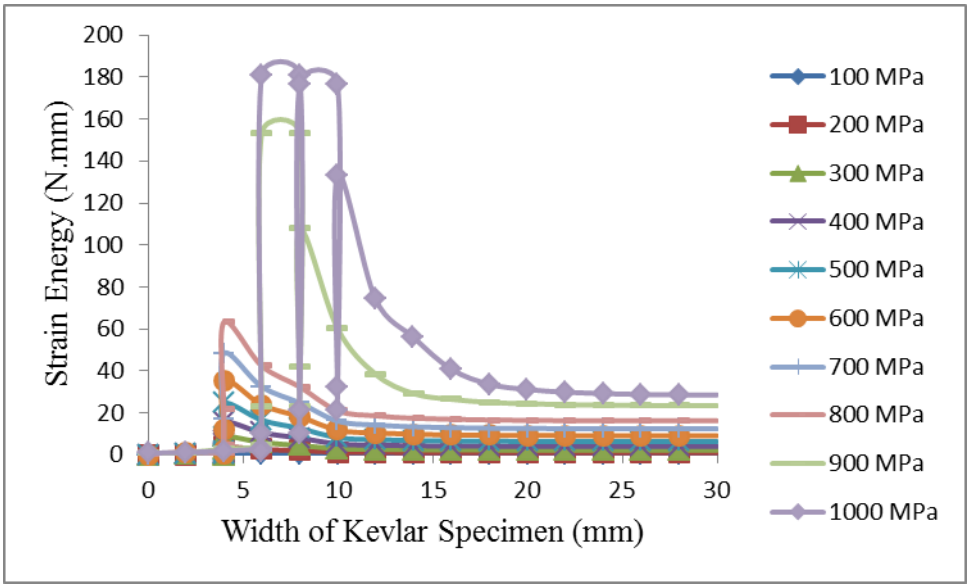

Figure 45 Strain Energy as function of Width of the Kevlar Specimen under deformed conditions below the crack location

Figure 45 shows the variation of strain energy as a function of width of the Kevlar specimen under deformed conditions below the crack location, for the crack located near to the fixed end of the specimen, at room temperature. It is observed that as the pressure increases, the strain energy increases and then firstly it gradually decreases and then a sudden decrement is observed. Moreover, along the width of the Kevlar specimen, the strain energy is higher between 5-10 mm, where the edge crack is further propagated.

7.1.3.4 Strain Energy Density Analysis

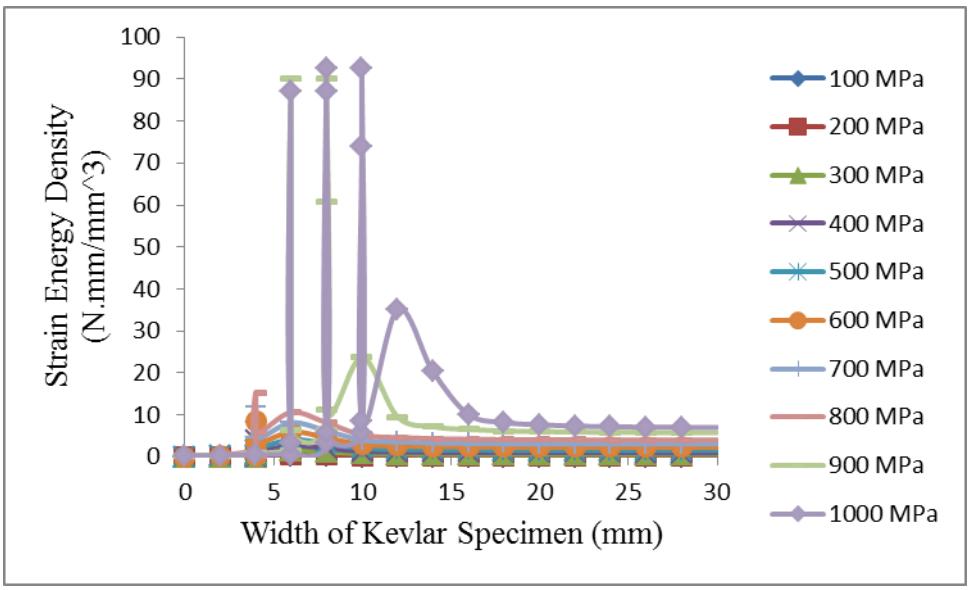

Figure 46 Strain Energy Density as function of Width of the Kevlar Specimen under deformed conditions above the crack location

Figure 46 shows the variation of the strain energy density as a function of the width of the Kevlar specimen under deformed conditions above the crack location, for the crack located near to the fixed end of the specimen, at room temperature. It is observed that as the pressure increases, the strain energy density firstly increases and then a sudden decrement is observed. As the strain energy density is defined as the strain energy per unit volume. Therefore, the similar behaviour will be observed in strain energy density as in strain energy. The maximum value for strain energy density observed is 92 N.mm/mm^3 at approximately 6mm and 8mm width of the specimen.

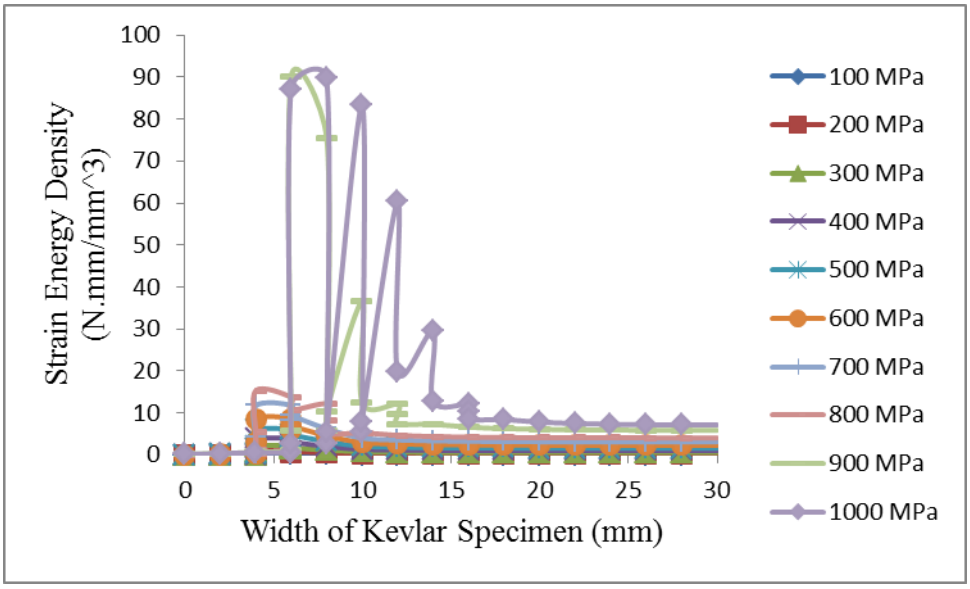

Figure 47 Strain Energy Density as function of Width of the Kevlar Specimen under deformed conditions below the crack location

Figure 47 shows the variation of the strain energy density as a function of the width of the Kevlar specimen under deformed conditions below the crack location for the crack located near to the fixed end of the specimen, at room temperature. It is observed that as the pressure increases, the strain energy density increases and then firstly decreases gradually and then a sudden decrement is observed. Moreover, along the width of the Kevlar specimen, the strain energy density is high between 5-10 mm from where the edge crack is initiated.

7.2 Mechanical Characterization of Kevlar at Cryogenic Temperatures

The results of three cases of a Kevlar specimen subjected to a uniaxial tensile loading obtained from the finite element solutions are considered in this section. The three cases are: 1) Crack towards the loading end, 2) Crack at the mid position and 3) Crack towards the fixed end in the specimen at the cryogenic temperatures are considered.

7.2.1 Crack towards the loading end

7.2.1.1 Stress Analysis

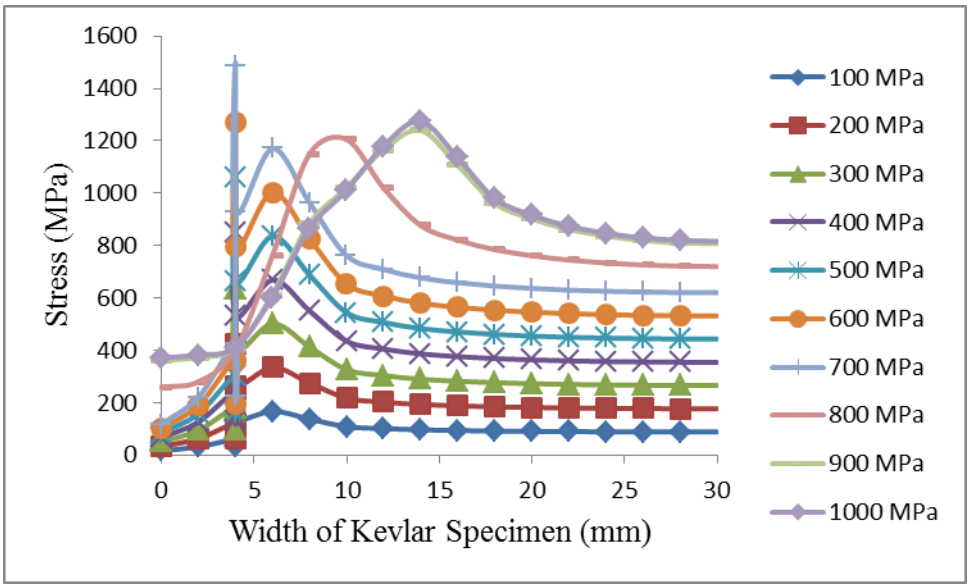

Figure 48 Stress as a function of Width of the Kevlar Specimen under deformed conditions above the crack location

Figure 48 shows the variation of stress as a function of width of the Kevlar specimen under deformed conditions above the crack location, for the crack located near to the loading end of the specimen, at cryogenic temperatures. It is observed along the width of the Kevlar specimen, as the pressure increases, the stress first increases and then it gradually decreases. The maximum stress of 1484 MPa occurred when the pressure of 700 MPa is applied. This increment in stress is due to the effect of stress that is concentrated at the tip of the crack. At approximately 700 MPa pressure, the crack tends to propagate. Therefore at this pressure, the maximum stress occurred. After the application of pressure more than 700 MPa, the graphs are shifted towards the right hand side, that is, the crack propagates towards the right hand side. However, after the crack propagates, the difference in the stresses occurred when comparison of the specimens at room and at cryogenic temperatures is done. That is, at 800

MPa, at room temperature, the stress obtained is 1237.87 MPa and at cryogenic temperature, the stress obtained is 1206 MPa.

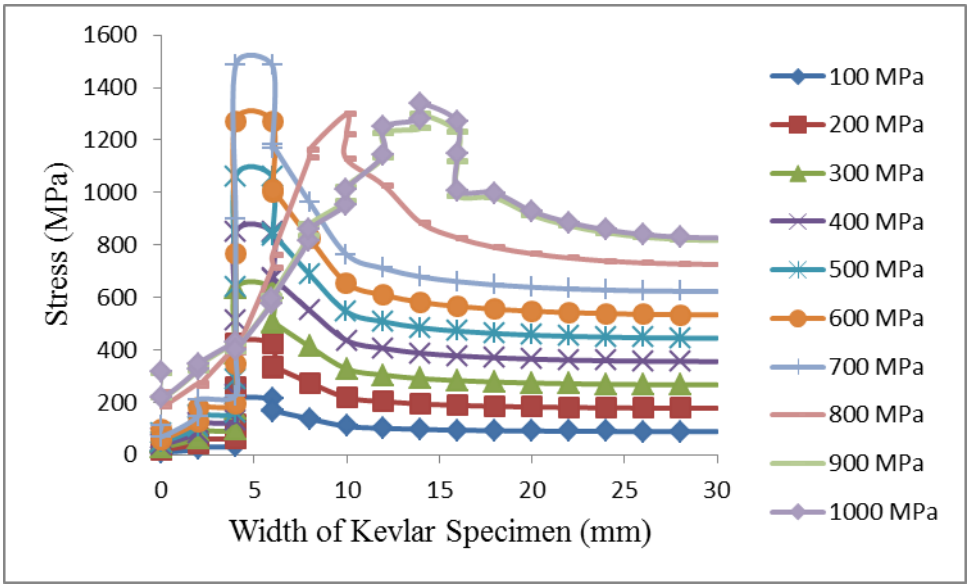

Figure 49 Stress as a function of Width of the Kevlar Specimen under deformed conditions below the crack location

Figure 49 shows the variation of stress as a function of width of the Kevlar specimen under deformed conditions below the crack location, for the crack located near to the loading end of the specimen, at cryogenic temperatures. It is observed that as the pressure increases, the stress increases. Moreover, along the width of the Kevlar specimen, the stress first increases and then it gradually decreases. On observing Figure 48 and Figure 49, it can be seen that there is an abrupt decrement for above the crack location and a gradual decrement in an initial stage for below the crack location. This difference may be due to the presence of residual stresses in the specimen.

7.2.1.2 Strain Analysis

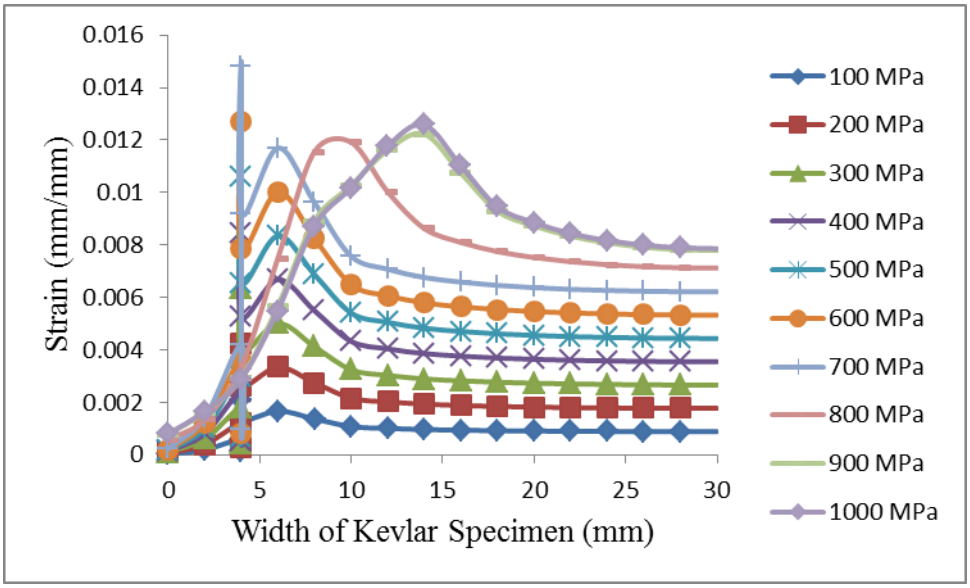

Figure 50 Strain as a function of Width of the Kevlar Specimen under deformed conditions above the crack location

Figure 50 shows the variation of strain as a function of width of the Kevlar specimen under deformed conditions above the crack location, for the crack located near to the loading end of the specimen, at cryogenic temperatures. It is observed that along the width of the Kevlar specimen, as the pressure increases, the strain first increases and then it gradually decreases. The maximum strain of 0.0148 mm/mm occurred when the pressure of 700 MPa is applied. As the stress is directly proportional to the strain, the similar type of increment is observed in the strain as observed in the stress. At approximately 700 MPa pressure, the crack tends to propagate. Therefore at this pressure, the maximum strain occurred. After the application of pressure more than 700 MPa, due to the shifting of the crack towards the right hand side, that is, the crack propagates towards the right hand side , the graphs are shifted towards the right hand side.

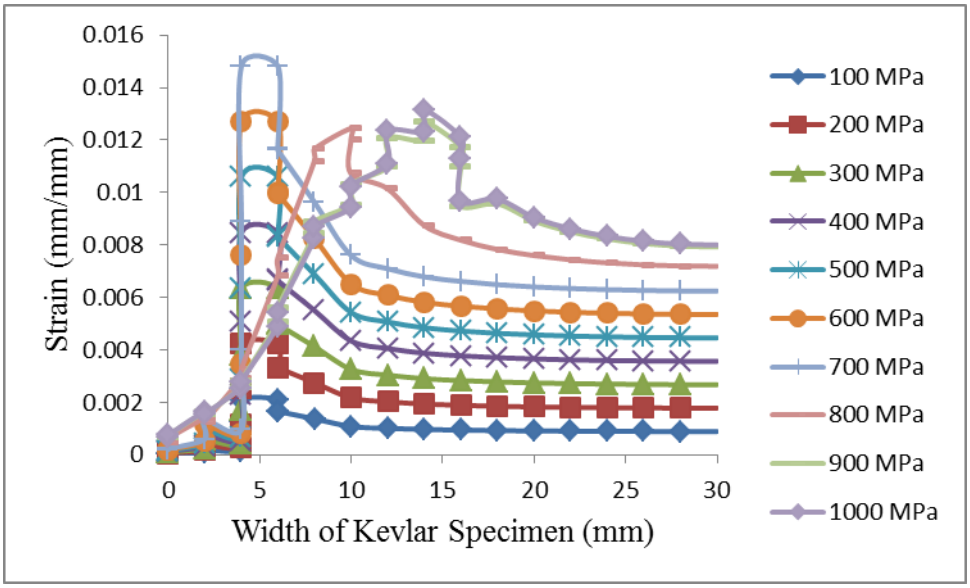

Figure 51 Strain as a function of Width of the Kevlar Specimen under deformed conditions below the crack location

Figure 51 shows the variation of strain as a function of width of the Kevlar specimen under deformed conditions below the crack location, for the crack located near to the loading end of the specimen, at room temperature. It is observed that as the pressure increases, the strain increases. Moreover, along the width of the Kevlar specimen, the strain first increases and then it gradually decreases. As there is difference in the behaviour of stresses, therefore, the difference in the behaviour of strains for above and below the crack location occurred.

7.2.1.3 Strain Energy Analysis

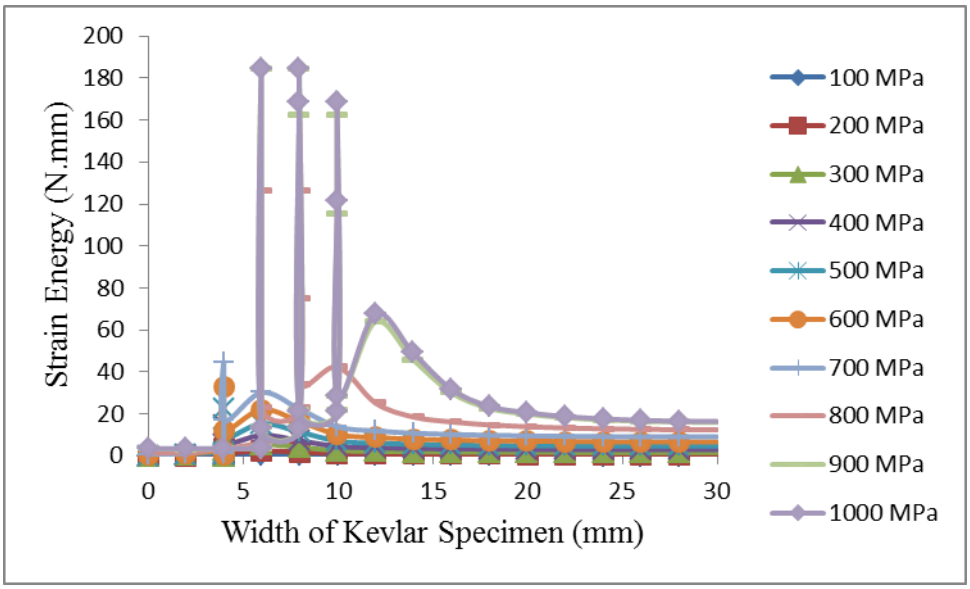

Figure 52 Strain Energy as function of Width of the Kevlar Specimen under deformed conditions above the crack location

Figure 52 shows the variation of strain energy as a function of width of the Kevlar specimen under deformed conditions above the crack location, for the crack located near to the loading end of the specimen, at cryogenic temperatures. It is observed that as the pressure increases, the strain energy increases and then decreases abruptly. The maximum amount of energy during the application of the load that the specimen could able to absorb was found to be approximately 184.6 N.mm at 900 MPa, nearly at the width of 6mm and the it suddenly decreases and again it reaches to its maximum value, that is, 184.6 N.mm at 8 mm width uptil which the material again sustained the energy and after that the crack further propagated. This may be the indication that when the crack is propagated and reached at 6mm from the start of propagation, it was able to absorb the energy uptil 184.6 N.mm and then it propagated further and after reaching at 8mm, it again withstand the load uptil the same energy and then further propagated.

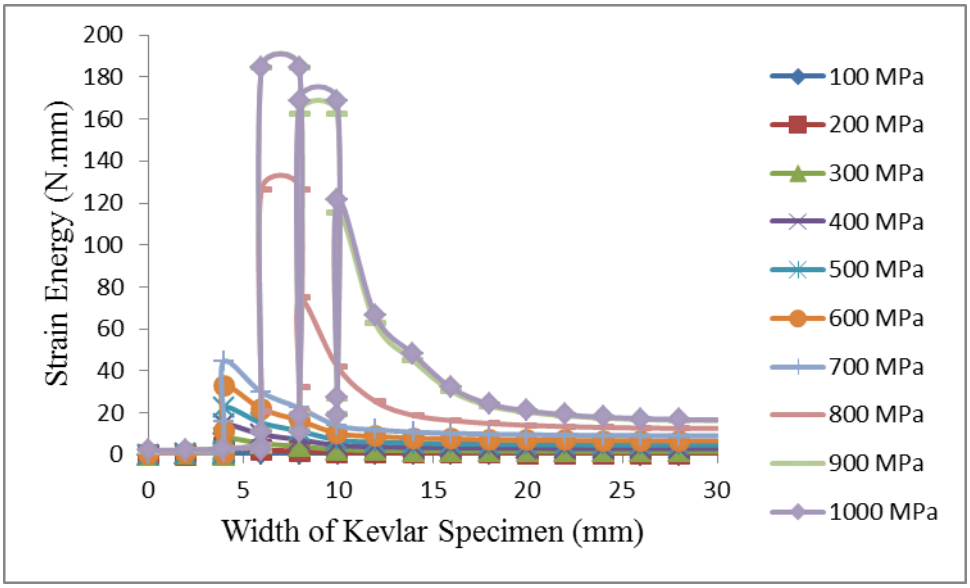

Figure 53 Strain Energy as function of Width of the Kevlar Specimen under deformed conditions below the crack location

Figure 53 shows the variation of strain energy as a function of width of the Kevlar specimen under deformed conditions below the crack location, for the crack located near to the loading end of the specimen, at cryogenic temperatures. It is observed that as the pressure increases, the strain energy increases and then firstly it gradually decreases and then a sudden decrement is observed. Moreover, along the width of the Kevlar specimen, the strain energy is higher between 5-10 mm, where the edge crack is further propagated.

7.2.1.4 Strain Energy Density Analysis

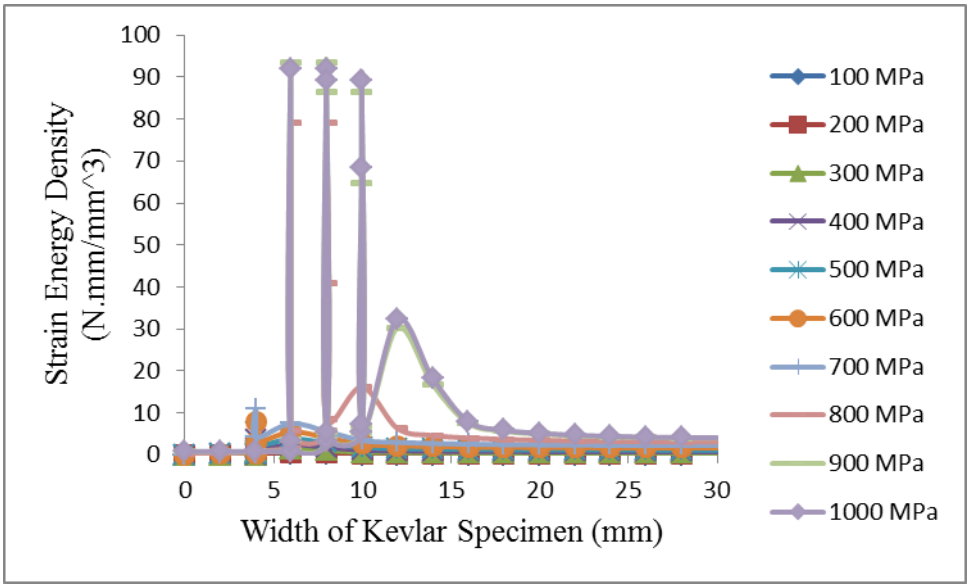

Figure 54 Strain Energy Density as function of Width of the Kevlar Specimen under deformed conditions above the crack location

Figure 54 shows the variation of the strain energy density as a function of the width of the Kevlar specimen under deformed conditions above the crack location, for the crack located near to the loading end of the specimen, at cryogenic temperatures. It is observed that as the pressure increases, the strain energy density firstly increases and then a sudden decrement is observed. As the strain energy density is defined as the strain energy per unit volume. Therefore, the similar behaviour will be observed in strain energy density as in strain energy. The maximum value for strain energy density observed is 93.3 $N.mm/mm^3$ at approximately 6mm and 8mm width of the specimen.

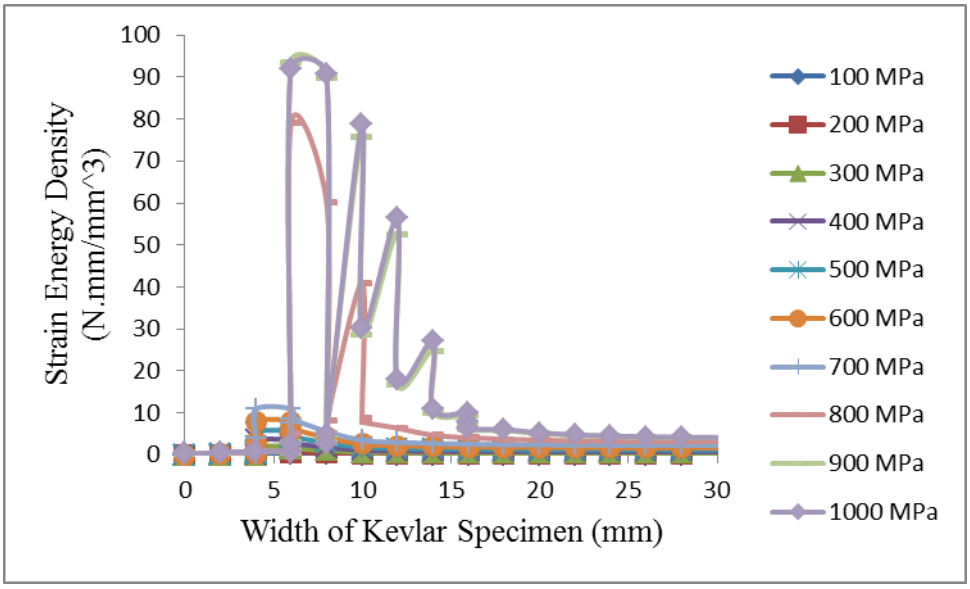

Figure 55 Strain Energy Density as function of Width of the Kevlar Specimen under deformed conditions below the crack location

Figure 55 shows the variation of the strain energy density as a function of the width of the Kevlar specimen under deformed conditions below the crack location, for the crack located near to the loading end of the specimen, at cryogenic temperatures. It is observed that as the pressure increases, the strain energy density increases and then firstly decreases gradually and then a sudden decrement is observed. Moreover, along the width of the Kevlar specimen, the strain energy density is high between 5-10 mm from where the edge crack is initiated.

7.2.2 Crack at the mid position

7.2.2.1 Stress Analysis

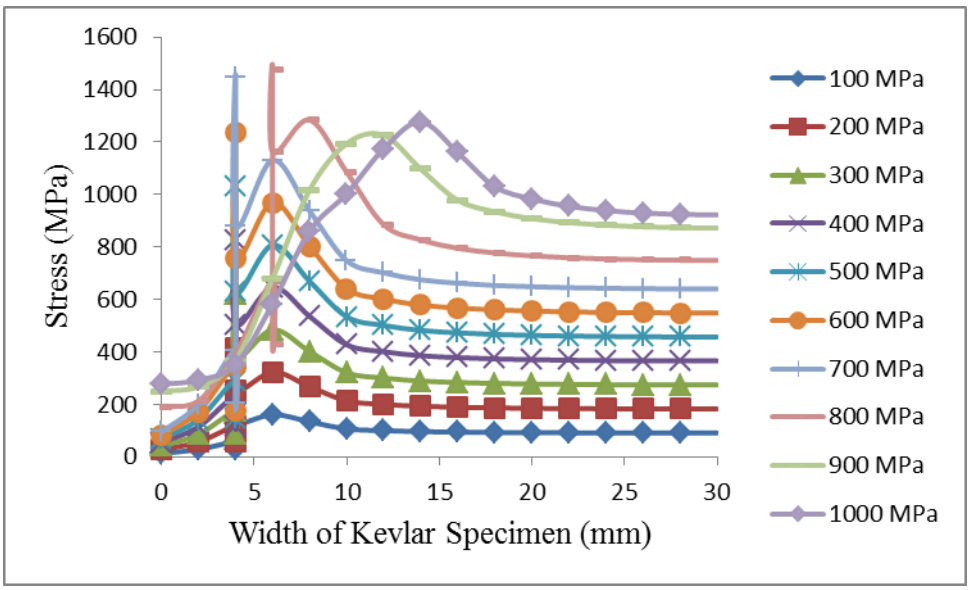

Figure 56 Stress as a function of Width of the Kevlar Specimen under deformed conditions above the crack location

Figure 56 shows shows the variation of stress as a function of width of the Kevlar specimen under deformed conditions above the crack location, for the crack located at the middle of the specimen, at cryogenic temperatures. It is observed that, along the width of the Kevlar specimen, the stress first increases and then it gradually decreases. The maximum stress of 1473 MPa occurred when the pressure of 800 MPa is applied. This increment in stress is due to the effect of stress that is concentrated at the tip of the crack. At approximately 800 MPa pressure, the crack tends to propagate. Therefore at this pressure, the maximum stress occurred. After the application of pressure more than 800 MPa, the graphs are shifted towards the right hand side, that is, the crack propagates towards the right hand side.

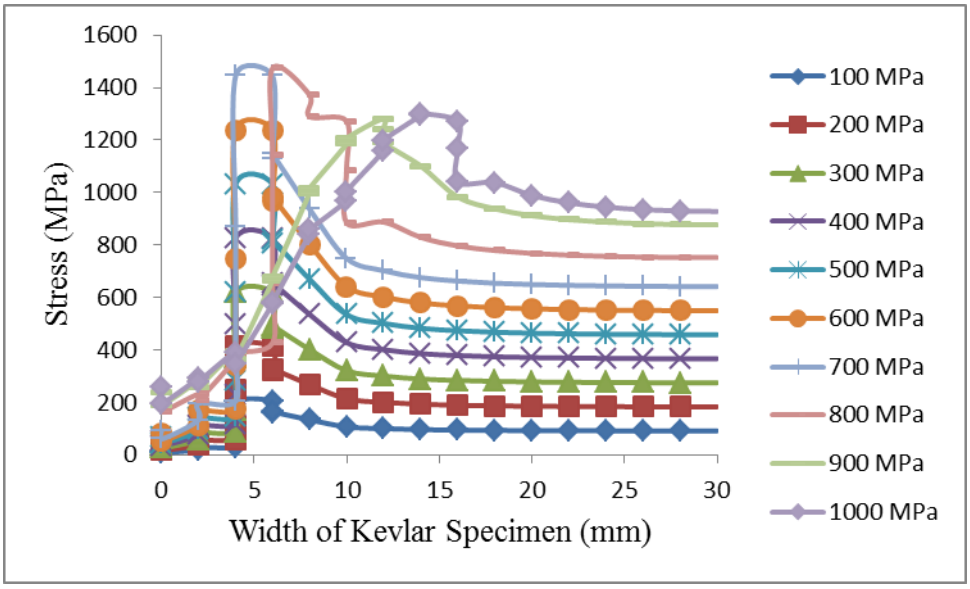

Figure 57 Stress as a function of Width of the Kevlar Specimen under deformed conditions below the crack location

Figure 57 shows the variation of stress as a function of width of the Kevlar specimen under deformed conditions below the crack location, for the crack located at the middle of the specimen, at cryogenic temperatures. It is observed that as the pressure increases, the stress increases. Moreover, along the width of the Kevlar specimen, the stress first increases and then it gradually decreases. On observing Figure 56 and Figure 57, it can be seen that there is an abrupt decrement for above the crack location and a gradual decrement in an initial stage for below the crack location.

7.2.2.2 Strain Analysis

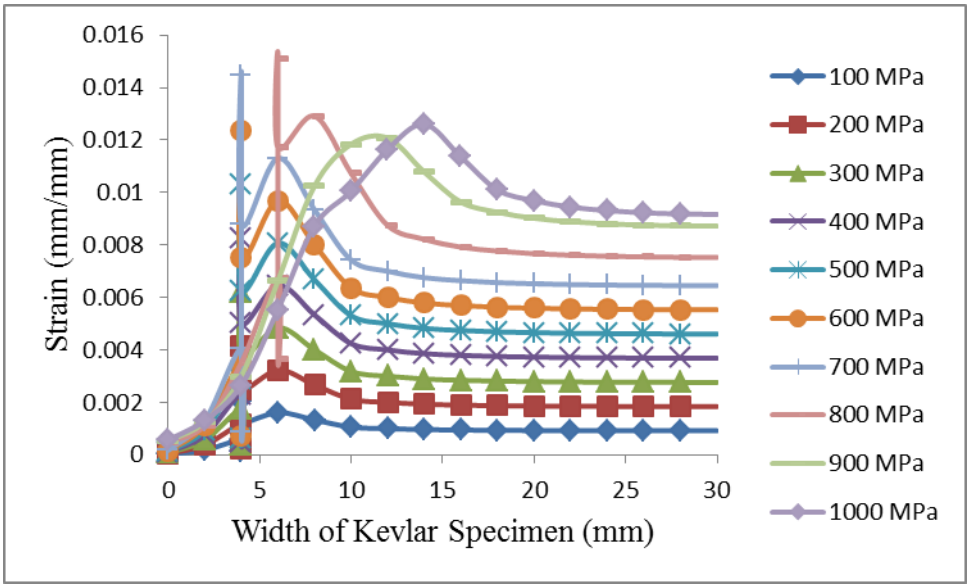

Figure 58 Strain as a function of Width of the Kevlar Specimen under deformed conditions above the crack location

Figure 58 shows the variation of strain as a function of width of the Kevlar specimen under deformed conditions above the crack location, for the crack located at the middle of the specimen, at cryogenic temperatures. It is observed that along the width of the Kevlar specimen, as the pressure increases, the strain first increases and then it gradually decreases. The maximum strain of 0.0151 mm/mm occurred when the pressure of 800 MPa is applied. As the stress is directly proportional to the strain, the similar type of increment is observed in the strain as observed in the stress. At approximately 800 MPa pressure, the crack tends to propagate. Therefore at this pressure, the maximum strain occurred. After the application of pressure more than 800 MPa, due to the shifting of the crack towards the right hand side, that is, the crack propagates towards the right hand side , the graphs are shifted towards the right hand side.

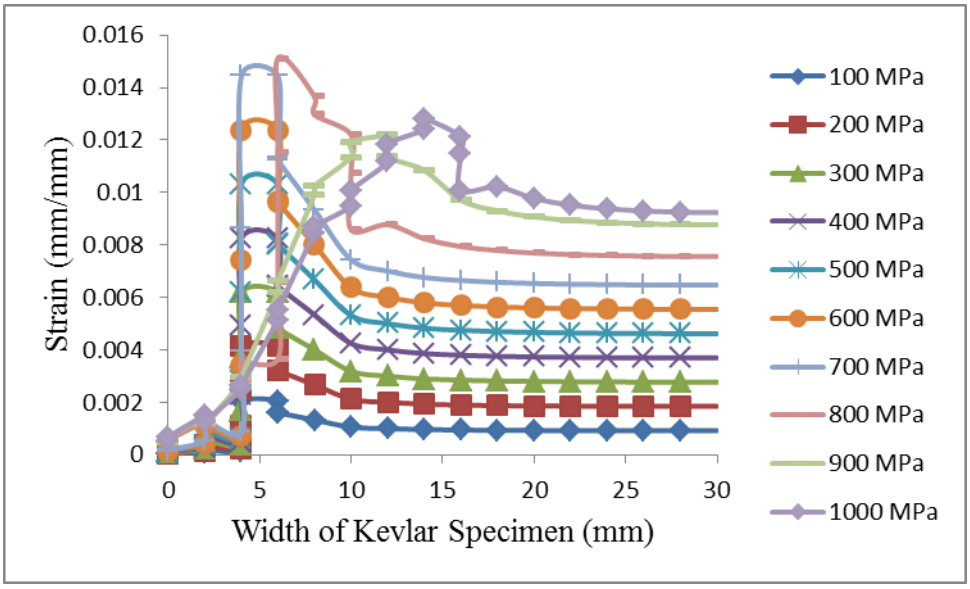

Figure 59 Strain as a function of Width of the Kevlar Specimen under deformed conditions below the crack location

Figure 59 shows the variation of strain as a function of width of the Kevlar specimen under deformed conditions below the crack location, for the crack located at the middle of the specimen, at cryogenic temperatures. It is observed that as the pressure increases, the strain increases. Moreover, along the width of the Kevlar specimen, the strain first increases and then it gradually decreases. As there is difference in the behaviour of stresses, therefore, the difference in the behaviour of strains for above and below the crack location occurred.

7.2.2.3 Strain Energy Analysis

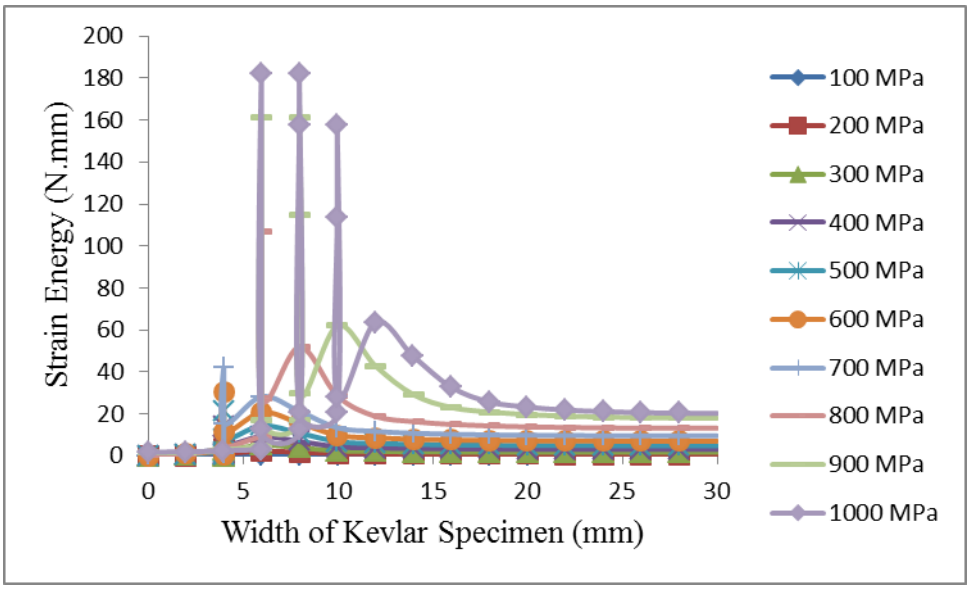

Figure 60 Strain Energy as function of Width of the Kevlar Specimen under deformed conditions above the crack location

Figure 60 shows the variation of strain energy as a function of width of the Kevlar specimen under deformed conditions above the crack location, for the crack located at the middle of the specimen, at cryogenic temperatures. It is observed that as the pressure increases, the strain energy increases and then decreases abruptly. The maximum amount of energy during the application of the load that the specimen could able to absorb was found to be approximately 182.27 N.mm at 1000 MPa, nearly at the width of 6mm and the it suddenly decreases and again it reaches to its maximum value, that is, 182.27 N.mm at 8 mm width uptil which the material again sustained the energy and after that the crack further propagated. This may be the indication that when the crack is propagated and reached at 6mm from the start of propagation, it was able to absorb the energy uptil 182.27 N.mm and then it propagated further and after reaching at 8mm, it again withstand the load uptil the same energy and then further propagated.

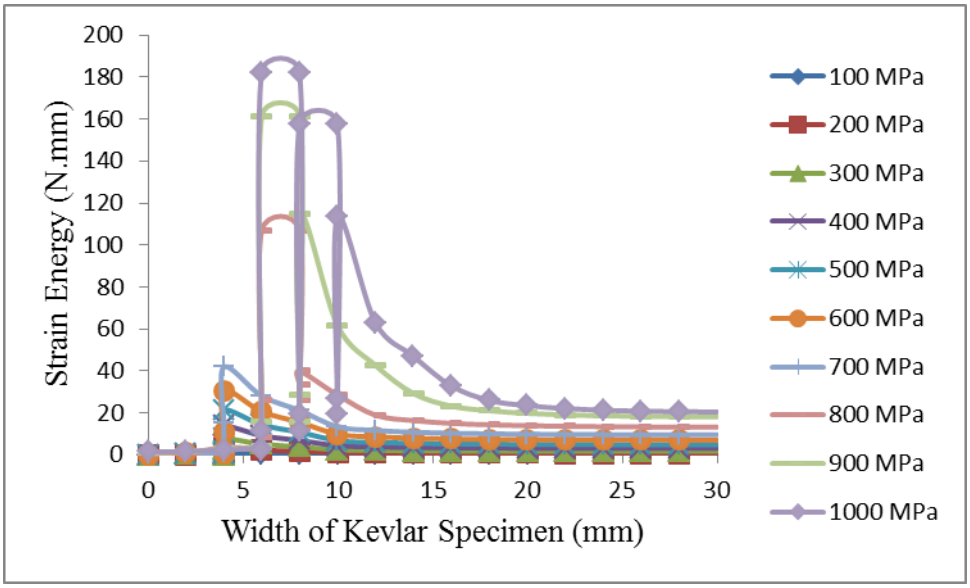

Figure 61 Strain Energy as function of Width of the Kevlar Specimen under deformed conditions below the crack location

Figure 61 shows the variation of strain energy as a function of width of the Kevlar specimen under deformed conditions below the crack location, for the crack located at the middle of the specimen, at cryogenic temperatures. It is observed that as the pressure increases, the strain energy increases and then firstly it gradually decreases and then a sudden decrement is observed. Moreover, along the width of the Kevlar specimen, the strain energy is higher between 5-10 mm, where the edge crack is further propagated.

7.2.2.4 Strain Energy Density Analysis

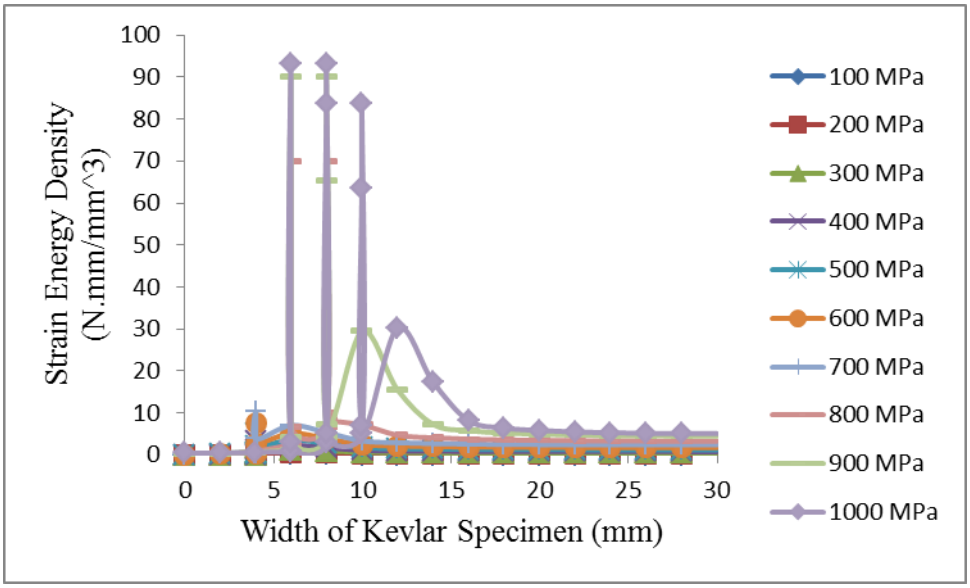

Figure 62 Strain Energy Density as function of Width of the Kevlar Specimen under deformed conditions above the crack location

Figure 62 shows the variation of the strain energy density as a function of the width of the Kevlar specimen under deformed conditions above the crack location, for the crack located at the middle of the specimen, at cryogenic temperatures. It is observed that as the pressure increases, the strain energy density firstly increases and then a sudden decrement is observed. As the strain energy density is defined as the strain energy per unit volume. Therefore, the similar behaviour will be observed in strain energy density as in strain energy. The maximum value for strain energy density observed is 93.2 N.mm/mm^3 at approximately 6mm and 8mm width of the specimen.

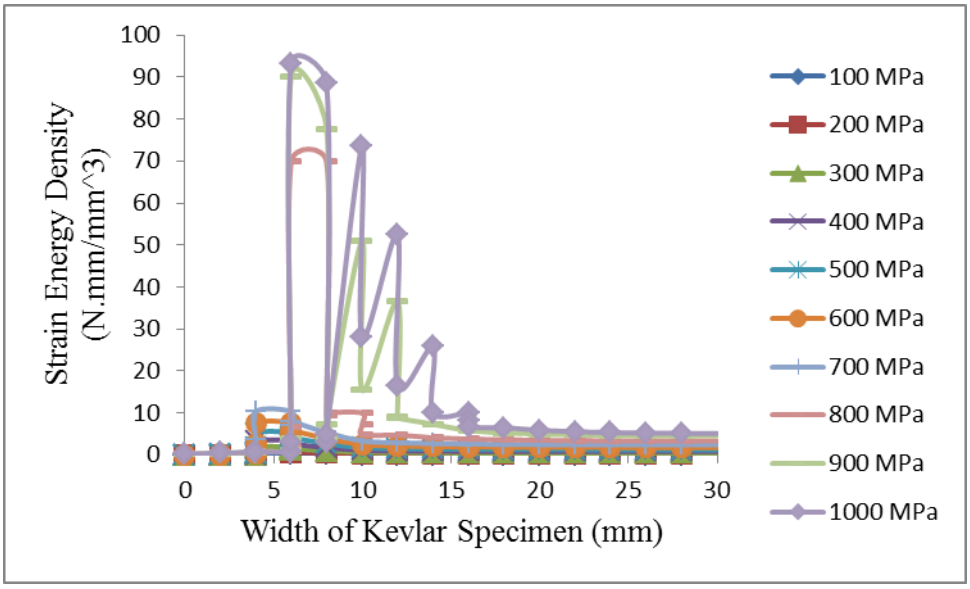

Figure 63 Strain Energy Density as function of Width of the Kevlar Specimen under deformed conditions below the crack location

Figure 63 shows the variation of the strain energy density as a function of the width of the Kevlar specimen under deformed conditions below the crack location, for the crack located at the middle of the specimen, at cryogenic temperatures. It is observed that as the pressure increases, the strain energy density increases and then firstly decreases gradually and then a sudden decrement is observed. Moreover, along the width of the Kevlar specimen, the strain energy density is high between 5-10 mm from where the edge crack is initiated.

7.2.3 Crack towards the fixed end

7.2.3.1 Stress Analysis

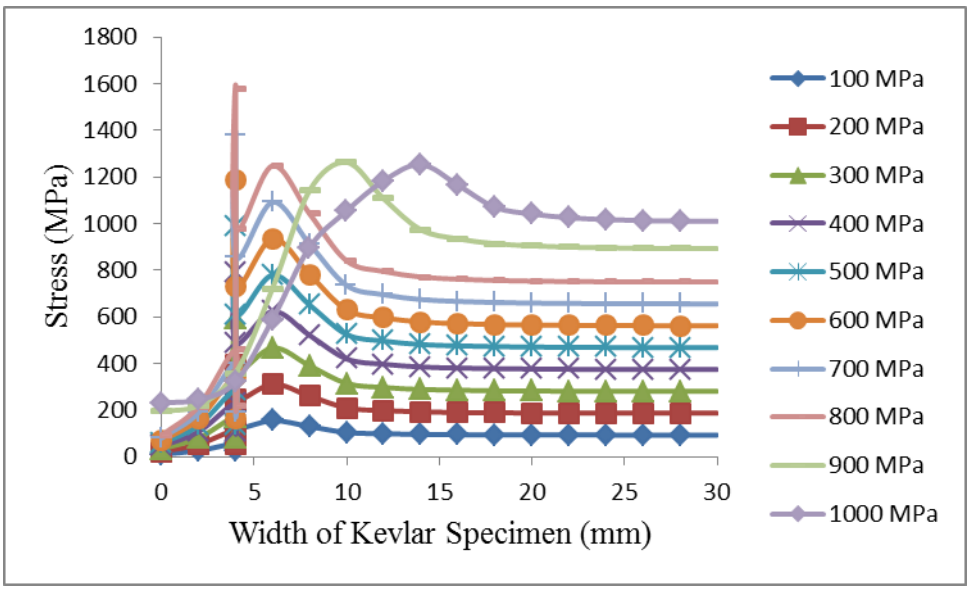

Figure 64 Stress as a function of Width of the Kevlar Specimen under deformed conditions above the crack location

Figure 64 shows the variation of stress as a function of width of the Kevlar specimen under deformed conditions above the crack location, for the crack located near to the fixed end of the specimen, at cryogenic temperatures. It is observed that, along the width of the Kevlar specimen, the stress first increases and then it gradually decreases. The maximum stress of 1579 MPa occurred when the pressure of 800 MPa is applied. This increment in stress is due to the effect of stress that is concentrated at the tip of the crack. At approximately 800 MPa pressure, the crack tends to propagate. Therefore at this pressure, the maximum stress occurred. After the application of pressure more than 800 MPa, the graphs are shifted towards the right hand side, that is, the crack propagates towards the right hand side. However, after the crack propagates, the difference in the stresses occurred when comparison of the specimens at room and at cryogenic temperatures is done. That is, at 900 MPa, at room temperature, the stress obtained is 1287.87 MPa and at cryogenic temperature, the stress obtained is 1263 MPa.

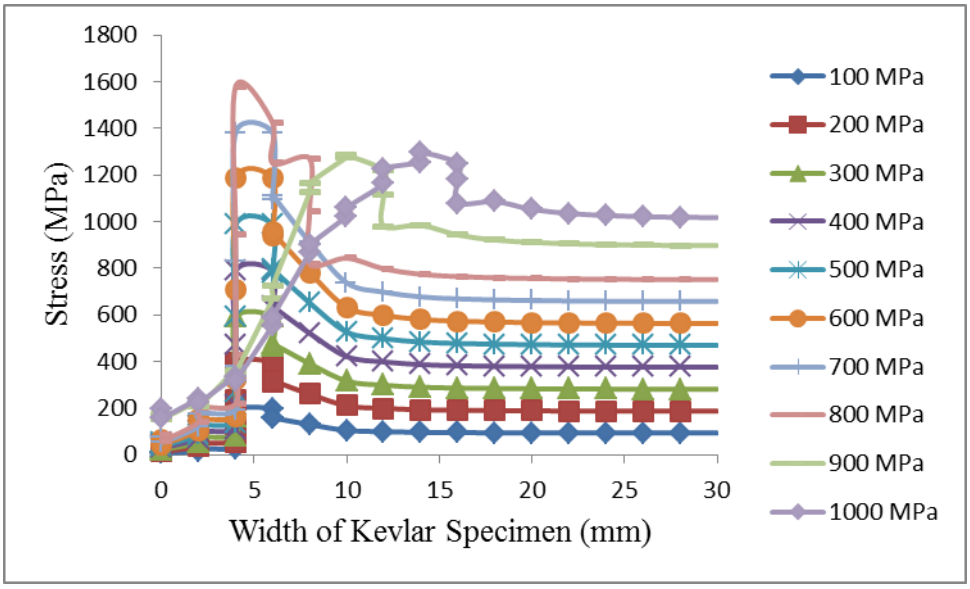

Figure 65 Stress as a function of Width of the Kevlar Specimen under deformed conditions below the crack location

Figure 65 shows the variation of stress as a function of width of the Kevlar specimen under deformed conditions below the crack location, for the crack located near to the fixed end of the specimen, at cryogenic temperatures. It is observed that as the pressure increases, the stress increases. Moreover, along the width of the Kevlar specimen, the stress first increases and then it gradually decreases. On observing Figure 64 and Figure 65, it can be seen that there is an abrupt decrement for above the crack location and a gradual decrement in an initial stage for below the crack location.

7.2.3.2 Strain Analysis

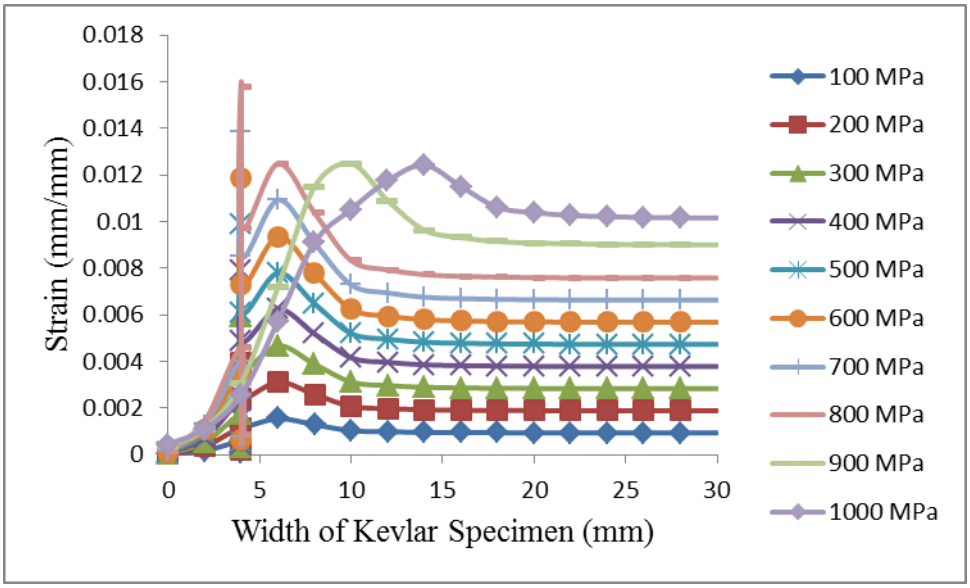

Figure 66 Strain as a function of Width of the Kevlar Specimen under deformed conditions above the crack location

Figure 66 shows the variation of strain as a function of width of the Kevlar specimen under deformed conditions above the crack location, for the crack located near to the fixed end of the specimen, at cryogenic temperatures. It is observed that along the width of the Kevlar specimen, as the pressure increases, the strain first increases and then it gradually decreases. The maximum strain of 0.0158 mm/mm occurred when the pressure of 800 MPa is applied. As the stress is directly proportional to the strain, the similar type of increment is observed in the strain as observed in the stress. At approximately 800 MPa pressure, the crack tends to propagate. Therefore at this pressure, the maximum strain occurred. After the application of pressure more than 800 MPa, due to the shifting of the crack towards the right hand side, that is, the crack propagates towards the right hand side , the graphs are shifted towards the right hand side.

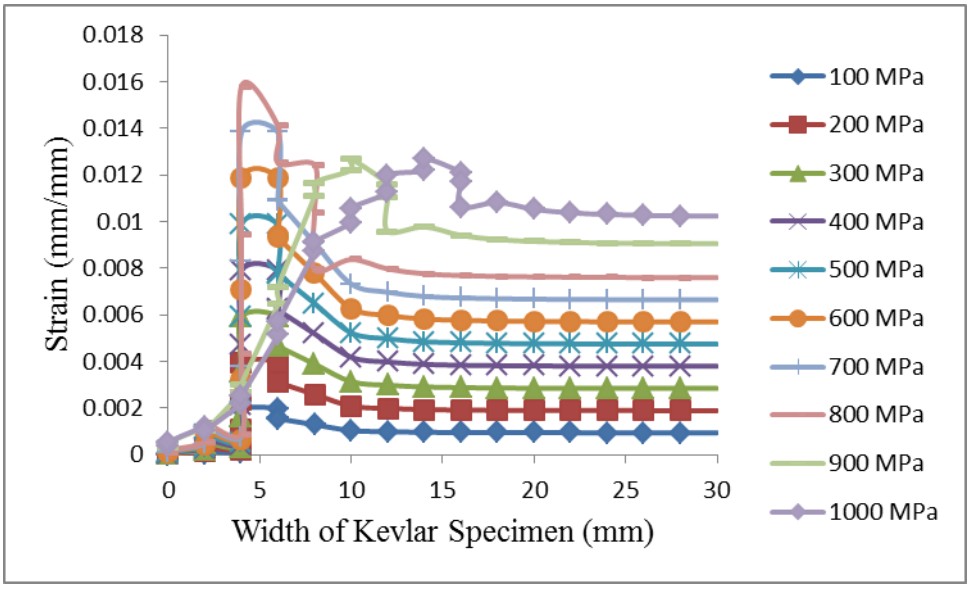

Figure 67 Strain as a function of Width of the Kevlar Specimen under deformed conditions below the crack location

Figure 67 shows the variation of strain as a function of width of the Kevlar specimen under deformed conditions below the crack location, for the crack located near to the fixed end of the specimen, at cryogenic temperatures. It is observed that as the pressure increases, the strain increases. Moreover, along the width of the Kevlar specimen, the strain first increases and then it gradually decreases. As there is difference in the behaviour of stresses, therefore, the difference in the behaviour of strains for above and below the crack location occurred.

7.2.3.3 Strain Energy Analysis

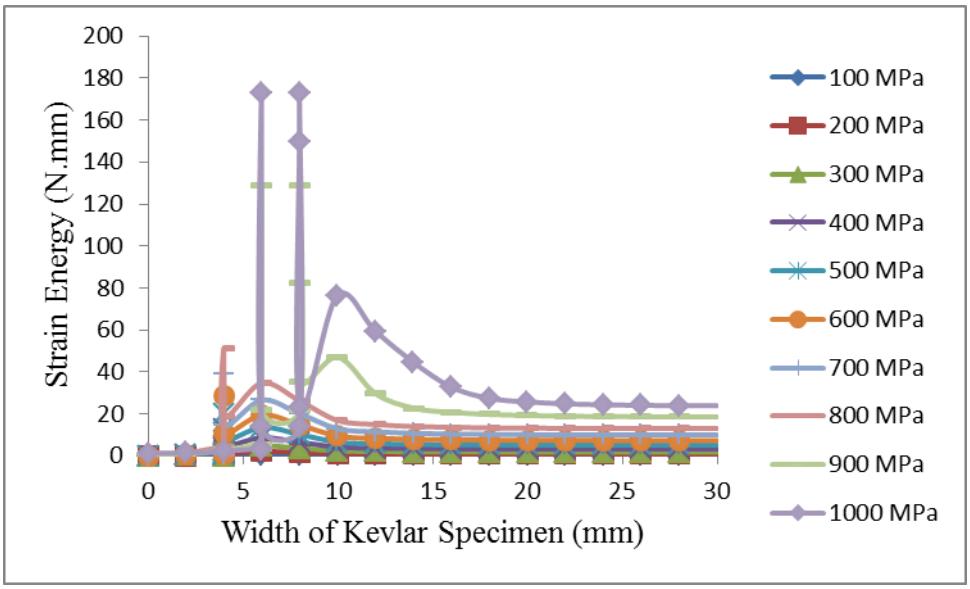

Figure 68 Strain Energy as function of Width of the Kevlar Specimen under deformed conditions above the crack location

Figure 68 shows the variation of strain energy as a function of width of the Kevlar specimen under deformed conditions above the crack location, for the crack located near to the fixed end of the specimen, at cryogenic temperatures. It is observed that as the pressure increases, the strain energy increases and then decreases abruptly. The maximum amount of energy during the application of the load that the specimen could able to absorb was found to be approximately 172.9 N.mm at 1000 MPa, nearly at the width of 6mm and the it suddenly decreases and again it reaches to its maximum value, that is, 172.9 N.mm at 8 mm width uptil which the material again sustained the energy and after that the crack further propagated. This may be the indication that when the crack is propagated and reached at 6mm from the start of propagation, it was able to absorb the energy uptil 172.9 N.mm and then it propagated further and after reaching at 8mm, it again withstand the load uptil the same energy and then further propagated.

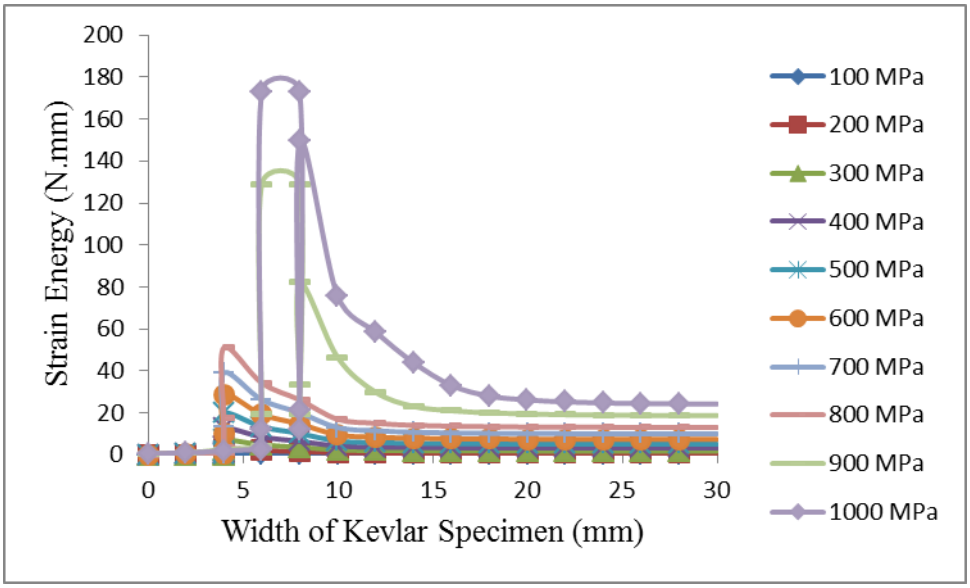

Figure 69 Strain Energy as function of Width of the Kevlar Specimen under deformed conditions below the crack location

Figure 69 shows the variation of strain energy as a function of width of the Kevlar specimen under deformed conditions below the crack location, for the crack located near to the fixed end of the specimen, at cryogenic temperature. It is observed that as the pressure increases, the strain energy increases and then firstly it gradually decreases and then a sudden decrement is observed. Moreover, along the width of the Kevlar specimen, the strain energy is higher between 5-10 mm, where the edge crack is further propagated.

7.2.3.4 Strain Energy Density Analysis

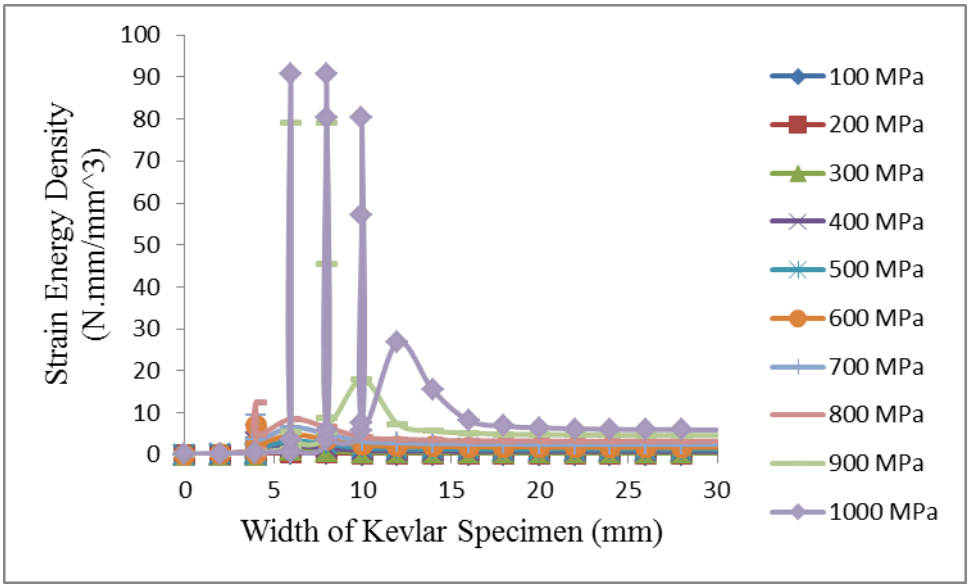

Figure 70 Strain Energy Density as function of Width of the Kevlar Specimen under deformed conditions above the crack location

Figure 70 shows the variation of the strain energy density as a function of the width of the Kevlar specimen under deformed conditions above the crack location, for the crack located near to the fixed end of the specimen, at cryogenic temperatures. It is observed that as the pressure increases, the strain energy density firstly increases and then a sudden decrement is observed. As the strain energy density is defined as the strain energy per unit volume. Therefore, the similar behaviour will be observed in strain energy density as in strain energy. The maximum value for strain energy density observed is 90.74 N.mm/mm^3 at approximately 6mm and 8mm width of the specimen.

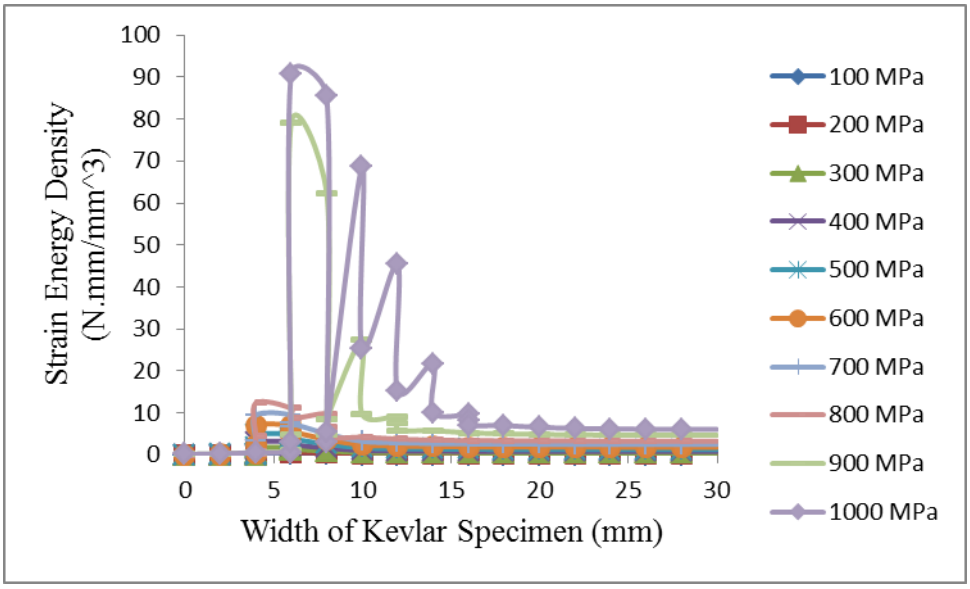

Figure 71 Strain Energy Density as function of Width of the Kevlar Specimen under deformed conditions below the crack location

Figure 71 shows the variation of the strain energy density as a function of the width of the Kevlar specimen under deformed conditions below the crack location for the crack located near to the fixed end of the specimen, at cryogenic temperatures. It is observed that as the pressure increases, the strain energy density increases and then firstly decreases gradually and then a sudden decrement is observed. Moreover, along the width of the Kevlar specimen, the strain energy density is high between 5-10 mm from where the edge crack is initiated.

CHAPTER

8 CONCLUSION

The purpose of this research work was to use the Extended Finite Element Method (XFEM) for inspecting the performance of crack behaviour in Kevlar 49 composites at room and cryogenic temperatures under various pressures ranging from 100 MPa to 1000 MPa. Results for stress, strain, strain energy and strain energy density are compared for above and below the crack location for three different crack location in the Kevlar specimen.. Further, comparison for the stress, strain, strain energy and strain energy density at room temperature and cryogenic temperature is done.

The following are the conclusions:

1. There was a minor difference in the stress, strain, strain energy and strain energy density, when comparison for above and below crack locations are compared. This difference might have occurred due to presence of residual stresses in the specimen.
2. On comparison for the three locations of the crack, that is, crack towards the loading end, crack at the mid position and crack towards the fixed end, there was a significant difference in the values of stress, strain, strain energy and strain energy density. This determines that the position of the crack can effect the failure of the material.
3. When compared to the room temperature, it has been proved that Kevlar is equally stronger at cryogenic temperatures and proved to be as one of the materials that can be used both at room and at cryogenic temperatures.

The outcomes demonstrated here can be effective for designers to analyze the behaviour of an edge crack in Kevlar 49 based composites at room as well as at cryogenic temperatures. This work may help the researchers to analysis the amount of stress a Kevlar fibre can sustain at room as well as at cryogenic temperatures. Kevlar may also be made self healed by adding some material in the form of liquid or semi liquid. Therefore, this may help the researchers to know about the strength of the materials that may be used for self healing purposes for the Kevlar in future. However, for more complete and quantitative analysis of this problem, further experimental as well as computational work, is necessary to be performed and various aspects such as compression, torque, bending moment etc., must be analysed.

9 REFERENCES

[1] T. J. Singh and S. Samanta, “Characterization of Kevlar Fiber and Its Composites: A Review,” *Mater. Today Proc.*, vol. 2, no. 4–5, pp. 1381–1387, 2015.

[2] G. Ventura and V. Martelli, “Very low temperature thermal conductivity of Kevlar 49,” *Cryogenics (Guildf).*, vol. 49, no. 7, pp. 376–377, 2009.

[3] B. L. James, R. M. Martinez, P. Shirron, J. Tuttle, N. M. Galassi, D. S. McGuinness, D. Puckett, J. J. Francis, and Y. Flom, “Mechanical tensile testing of titanium 15-3-3-3 and Kevlar 49 at cryogenic temperatures,” *AIP Conf. Proc.*, vol. 1435, no. 2012, pp. 78–85, 2012.

[4] A. Bersani, L. Canonica, M. Cariello, R. Cereseto, S. Di Domizio, and M. Pallavicini, “Long term elongation of Kevlar-49 single fiber at low temperature,” *Cryogenics (Guildf).*, vol. 54, pp. 50–53, 2013.

[5] P. K. Mallick, *Fiber-Reinforced Composites: Materials, Manufacturing, and Design, Second Edition*. Taylor & Francis, 1993.

[6] R. S. Dondapati, J. Ravula, S. Thadela, and P. R. Usurumarti, “Analytical approximations for thermophysical properties of supercritical nitrogen (SCN) to be used in futuristic high temperature superconducting (HTS) cables,” *Phys. C Supercond. its Appl.*, vol. 519, pp. 53–59, Dec. 2015.

[7] G. Vyas, R. S. Dondapati, and P. R. Usurumarti, “Parametric Evaluation of AC Losses in 500 MVA/1.1 kA High Temperature Superconducting (HTS) Cable for Efficient Power Transmission: Self Field Analysis,” *2014 European Modelling Symposium*. pp. 315–319, 2014.

[8] R. S. Dondapati and V. V Rao, “Pressure Drop and Heat Transfer Analysis of Long Length Internally Cooled HTS Cables,” *IEEE Transactions on Applied Superconductivity*, vol. 23, no. 3. p. 5400604, 2013.

[9] R. S. Dondapati and V. V Rao, “Influence of mass flow rate on Turbulent Kinetic

Energy (TKE) distribution in Cable-in-Conduit Conductors (CICCs) used for fusion grade magnets," *Fusion Eng. Des.*, vol. 88, no. 5, pp. 341–349, Jun. 2013.

[10] R. S. Dondapati and V. V Rao, "Entropy generation minimization (EGM) to optimize mass flow rate in dual channel cable-in-conduit conductors (CICCs) used for fusion grade magnets," *Fusion Eng. Des.*, vol. 89, no. 6, pp. 837–846, Jun. 2014.

[11] R. S. Dondapati and V. V Rao, "CFD Analysis of Cable-In-Conduit Conductors (CICC) for Fusion Grade Magnets," *IEEE Transactions on Applied Superconductivity*, vol. 22, no. 3. p. 4703105, 2012.

[12] J. W. Bray, "10 – High-temperature superconducting motors and generators for power grid applications," in *Superconductors in the Power Grid*, 2015, pp. 325–344.

[13] B. Eom, C. Lee, S. Kim, C. Lee, and S. Yun, "Investigation on Prototype Superconducting Linear Synchronous Motor (LSM) for 600-km/h Wheel-Type Railway," *Phys. Procedia*, vol. 65, pp. 261–264, 2015.

[14] M. Hirakawa, S. Inadama, K. Kikukawa, E. Suzuki, and H. Nakasima, "Developments of superconducting motor with YBCO bulk magnets," *Phys. C Supercond.*, vol. 392, pp. 773–776, 2003.

[15] E. Viola, A. Piva, and E. Radi, "Crack propagation in an orthotropic medium under general loading," *Eng. Fract. Mech.*, vol. 34, no. 5–6, pp. 1155–1174, 1989.

[16] M. H. Aliabadi and P. Sollero, "Crack growth analysis in homogeneous orthotropic laminates," *Compos. Sci. Technol.*, vol. 58, no. 10, pp. 1697–1703, 1998.

[17] K. B. Broberg, "Intersonic crack propagation in an orthotropic material," *Int. J. Fract.*, vol. 99, no. 1–2, pp. 1–11, 1999.

[18] W. K. Lim, S. Y. Choi, and B. V. Sankar, "Biaxial load effects on crack extension in anisotropic solids," *Eng. Fract. Mech.*, vol. 68, no. 4, pp. 403–416, 2001.

[19] L. Nobile and C. Carloni, "Fracture analysis for orthotropic cracked plates," *Compos. Struct.*, vol. 68, no. 3, pp. 285–293, 2005.

[20] F. García-Sánchez, C. Zhang, and A. Sáez, “A two-dimensional time-domain boundary element method for dynamic crack problems in anisotropic solids,” *Eng. Fract. Mech.*, vol. 75, no. 6, pp. 1412–1430, 2008.

[21] A. R. M. Kasavajhala and L. Gu, “Fracture analysis of Kevlar-49/epoxy and e-glass/epoxy doublers for reinforcement of cracked aluminum plates,” *Compos. Struct.*, vol. 93, no. 8, pp. 2090–2095, 2011.

[22] Y. Yang, G. Sun, H. Zheng, and X. Fu, “A four-node quadrilateral element fitted to numerical manifold method with continuous nodal stress for crack analysis,” *Comput. Struct.*, vol. 177, pp. 69–82, 2016.

[23] R. M. JONES, “Mechanics of composite materials,” *Mechanics of Composite Materials*, no. 2. p. 519, 1999.

[24] T. L. Anderson, *Fracture Mechanics: Fundamentals and Applications*, vol. 58, no. 1. 2012.

[25] J. R. Rice, “A Path Independent Integral and the Approximate Analysis of Strain Concentration by Notches and Cracks,” *J. Appl. Mech.*, vol. 35, no. 2, pp. 379–386, 1968.

[26] J. W. Hutchinson, “Singular behaviour at the end of a tensile crack in a hardening material,” *J. Mech. Phys. Solids*, vol. 16, no. 1, pp. 13–31, Jan. 1968.

[27] J. R. Rice and G. F. Rosengren, “Plane strain deformation near a crack tip in a power-law hardening material,” *J. Mech. Phys. Solids*, vol. 16, no. 1, pp. 1–12, Jan. 1968.

[28] A. A. Griffith, “The Phenomena of Rupture and Flow in Solids,” *Philos. Trans. R. Soc. A Math. Phys. Eng. Sci.*, vol. 221, no. 582–593, pp. 163–198, 1921.

[29] G. R. Irwin, “Linear fracture mechanics, fracture transition, and fracture control,” *Eng. Fract. Mech.*, vol. 1, no. 2, pp. 241–257, 1968.

[30] D. S. Dugdale, “Yielding of steel,” *J. Mech. Phys. Solids*, vol. 8, pp. 100–104, 1960.

[31] J. D. Eshelby, “The Continuum Theory of Lattice Defects,” 1956, pp. 79–144.

[32] X. Li and J. Chen, “An extended cohesive damage model for simulating multicrack propagation in fibre composites,” *Compos. Struct.*, vol. 143, pp. 1–8, 2016.

[33] N. R. Iyer, G. S. Palani, and A. Ramachandra Murthy, “Advanced Methodologies for Fracture Analysis and Damage Tolerant Evaluation,” *Proc. Indian Natl. Sci. Acad.*, vol. 0, no. 0, pp. 209–222, 2016.

[34] S. C. Wu, S. Q. Zhang, and Z. W. Xu, “Thermal crack growth-based fatigue life prediction due to braking for a high-speed railway brake disc,” *Int. J. Fatigue*, vol. 87, pp. 359–369, 2016.

[35] H. Zhang, J. Liu, and Z. Zuo, “Investigation into the effects of tangential force on fretting fatigue based on XFEM,” *Tribol. Int.*, vol. 99, pp. 23–28, 2016.

[36] G. Liu, D. Zhou, J. Ma, and Z. Han, “Numerical investigation of mixed-mode crack growth in ductile material using elastic???plastic XFEM,” *J. Brazilian Soc. Mech. Sci. Eng.*, vol. 38, no. 6, pp. 1689–1699, 2016.

[37] K. P. Marimuthu, F. Rickhey, H. Lee, and J. H. Lee, “Spherical Indentation Cracking in Brittle Materials : An XFEM Study,” pp. 267–273, 2016.

[38] T. Huang and Y. X. Zhang, “Numerical modelling of mechanical behaviour of engineered cementitious composites under axial tension,” *Comput. Struct.*, vol. 173, pp. 95–108, 2016.

[39] Y. Liu, Y. Zhang, S. Liu, S. Xiao, Y. Sun, and X. Wang, “Effect of unbonded areas around hole on the fatigue crack growth life of diffusion bonded titanium alloy laminates,” *Eng. Fract. Mech.*, vol. 163, pp. 176–188, 2016.

[40] N. Rodriguez-Florez, A. Carriero, and S. J. Shefelbine, “The use of XFEM to assess the influence of intra-cortical porosity on crack propagation,” *Comput. Methods Biomech. Biomed. Engin.*, vol. 5842, no. November, pp. 1–8, 2016.

[41] H. Jia and Y. Nie, “Thermoelastic analysis of multiple defects with the extended finite element method,” *Acta Mech. Sin.*, vol. 32, no. 6, pp. 1123–1137, 2016.

[42] X. Xu, J. Xu, J. Chen, P. Li, B. Liu, and Y. Li, “Investigation of dynamic multi-

cracking behavior in PVB laminated glass plates," *Int. J. Impact Eng.*, vol. 100, pp. 62–74, 2017.

[43] R. Dimitri, N. Fantuzzi, Y. Li, and F. Tornabene, "Numerical computation of the crack development and SIF in composite materials with XFEM and SFEM," *Compos. Struct.*, vol. 160, pp. 468–490, 2017.

[44] Z. Wang, T. Yu, T. Q. Bui, S. Tanaka, C. Zhang, S. Hirose, and J. L. Curiel-Sosa, "3-D local mesh refinement XFEM with variable-node hexahedron elements for extraction of stress intensity factors of straight and curved planar cracks," *Comput. Methods Appl. Mech. Eng.*, vol. 313, pp. 375–405, 2017.

[45] A. Nasirmanesh and S. Mohammadi, "Eigenvalue buckling analysis of cracked functionally graded cylindrical shells in the framework of the extended finite element method," *Compos. Struct.*, vol. 159, pp. 548–566, 2017.

[46] K. Huang, L. Guo, H. Yu, P. Jia, and T. Kitamura, "A domain-independent interaction integral method for evaluating the dynamic stress intensity factors of an interface crack in nonhomogeneous materials," *Int. J. Solids Struct.*, vol. 100, pp. 547–557, 2016.

[47] Z. Wang, T. Yu, T. Q. Bui, N. A. Trinh, N. T. H. Luong, N. D. Duc, and D. H. Doan, "Numerical modeling of 3-D inclusions and voids by a novel adaptive XFEM," *Adv. Eng. Softw.*, vol. 102, pp. 105–122, 2016.

[48] L. Wu, P. Liu, C. Shi, Z. Zhang, T. Q. Bui, and D. Jiao, "Edge-based smoothed extended finite element method for dynamic fracture analysis," *Appl. Math. Model.*, vol. 0, pp. 1–16, 2016.

[49] X. F. Hu, B. Y. Chen, M. Tirvaudey, V. B. C. Tan, and T. E. Tay, "Integrated XFEM-CE analysis of delamination migration in multi-directional composite laminates," *Compos. Part A Appl. Sci. Manuf.*, vol. 90, pp. 161–173, 2016.

[50] L. Marsavina, D. M. Constantinescu, E. Linul, F. A. Stuparu, and D. A. Apostol, "Experimental and numerical crack paths in PUR foams," *Eng. Fract. Mech.*, vol. 167, pp. 68–83, 2016.

[51] C. Zhang, C. Wang, T. Lahmer, P. He, and T. Rabczuk, "A dynamic XFEM

formulation for crack identification," *Int. J. Mech. Mater. Des.*, 2015.

[52] S. N. Raja, S. Basu, A. M. Limaye, T. J. Anderson, C. M. Hyland, L. Lin, A. P. Alivisatos, and R. O. Ritchie, "Strain-dependent dynamic mechanical properties of Kevlar to failure: Structural correlations and comparisons to other polymers," *Mater. Today Commun.*, vol. 2, pp. e33–e37, 2015.

[53] R. Tian and L. Wen, "Improved XFEM—An extra-dof free, well-conditioning, and interpolating XFEM," *Comput. Methods Appl. Mech. Eng.*, vol. 285, pp. 639–658, 2015.

[54] S. H. Ardakani, H. Ahmadian, and S. Mohammadi, "Thermo-mechanically coupled fracture analysis of shape memory alloys using the extended finite element method," *Smart Mater. Struct.*, vol. 24, no. 4, p. 45031, 2015.

[55] G. Wang, S. Wang, N. Duan, Y. Huangfu, H. Zhang, W. Xu, and J. Qiu, "Extended Finite-Element Method for Electric Field Analysis of Insulating Plate With Crack," vol. 51, no. 3, pp. 3–6, 2015.

[56] F. Curà, A. Mura, and C. Rosso, "Effect of rim and web interaction on crack propagation paths in gears by means of XFEM technique," *Fatigue Fract. Eng. Mater. Struct.*, vol. 38, no. 10, pp. 1237–1245, 2015.

[57] J. J. Liu, H. Huang, R. Liu, L. Rong, W. Wang, and Z. R. Nie, "Finite Element Analysis of the Influence of Crack Tip Stress Distributionon Fatigue Crack Propagation Rate of 5XXX Aluminum Alloy," *Mater. Sci. Forum*, vol. 817, pp. 698–705, 2015.

[58] M. Yu, Z. H. Dai, and G. J. Hu, "Crack Extension Calculation under Tensile and Shear Load by XFEM," *Appl. Mech. Mater.*, vol. 580–583, pp. 3046–3050, 2014.

[59] Y. L. Pang and D. M. Dai, "XFEM for Crack Propagation in Fiber-Reinforced Materials," *Adv. Mater. Res.*, vol. 997, pp. 450–453, 2014.

[60] S. Natarajan, P. Kerfriden, D. R. Mahapatra, and S. P. A. Bordas, "Numerical Analysis of the Inclusion-Crack Interaction by the Extended Finite Element Method," *Int. J. Comput. Methods Eng. Sci. Mech.*, vol. 15, no. 1, pp. 26–32, 2013.

[61] L. P. Qiu, E. C. Zhu, and J. W. G. van de Kuilen, “Modeling crack propagation in wood by extended finite element method,” *Eur. J. Wood Wood Prod.*, vol. 72, no. 2, pp. 273–283, 2013.

[62] X. D. Zhang, “Free Vibration Analysis and Damage Identification of Beam-Like Structures Containing a Crack Based on the Extended Finite Element Method,” *Adv. Mater. Res.*, vol. 831, pp. 164–169, 2013.

[63] D. Zhu, B. Mobasher, A. Vaidya, and S. D. Rajan, “Mechanical behaviors of Kevlar 49 fabric subjected to uniaxial, biaxial tension and in-plane large shear deformation,” *Compos. Sci. Technol.*, vol. 74, pp. 121–130, 2013.

[64] M. Cheng, W. Chen, and T. Weerasooriya, “Mechanical Properties of Kevlar ® KM2 Single Fiber,” vol. 127, no. April 2005, pp. 197–203, 2013.

[65] X. Q. Li, X. Y. Sun, and Y. W. Li, “Study on Three-Point Bending Numerical Tests of CFRP Reinforced Concrete Beam with Initial Crack,” *Adv. Mater. Res.*, vol. 838–841, pp. 639–643, 2013.

[66] R. P. Reed and M. Golda, “Cryogenic properties of unidirectional composites,” *Cryogenics (Guildf).*, vol. 34, no. 11, pp. 909–928, 1994.

[67] G. Hartwig and S. Knaak, “Fibre-epoxy composites at low temperatures,” *Cryogenics (Guildf).*, vol. 24, no. 11, pp. 639–647, 1984.

[68] S. Yang, V. B. Chalivendra, Y. K. Kim, and A. Kevlar, “Fracture and Impact Characterization of Novel Auxetic Kevlar ® / Epoxy Laminated Composites Department of Mechanical Engineering Department of Bioengineering University of Massachusetts Dartmouth , North Dartmouth , MA , 02747,” 2017.

[69] R. Kapoor, L. Pangeni, A. K. Bandaru, S. Ahmad, and N. Bhatnagar, “High strain rate compression response of woven Kevlar reinforced polypropylene composites,” *Compos. Part B Eng.*, vol. 89, pp. 374–382, 2016.

[70] A. K. Bandaru, V. V. Chavan, S. Ahmad, R. Alagirusamy, and N. Bhatnagar, “Ballistic impact response of Kevlar?? reinforced thermoplastic composite armors,” *Int. J. Impact Eng.*, vol. 89, pp. 1–13, 2016.

[71] G. Cai, D. Li, D. Fang, and W. Yu, “A new apparatus to measure the effect of temperature and light on the bending fatigue properties of Kevlar 49 and PBO fibers,” *El sevier*, vol. 40, pp. 143–148, 2014.

[72] A. Russelle and N. Naganambi, “Numerical Investigation of Bonded Repair for TDS of Helicopter and Characterization of Kevlar/Epoxy Composite Patch,” *Procedia Mater. Sci.*, vol. 5, pp. 204–211, 2014.

[73] S.-C. Woo and T.-W. Kim, “High strain-rate failure in carbon/Kevlar hybrid woven composites via a novel SHPB-AE coupled test,” *Compos. Part B Eng.*, vol. 97, pp. 317–328, 2016.

[74] B. S. Yilbas and S. S. Akhtar, “Laser cutting of Kevlar laminates and thermal stress formed at cutting sections,” *Opt. Lasers Eng.*, vol. 50, no. 2, pp. 204–209, 2012.

[75] U. K. Fatema and Y. Gotoh, “Iodine-aided palladium-free catalyzation process for durable electroless nickel plating on Kevlar ® fiber,” *Surf. Coatings Technol.*, vol. 206, no. 16, pp. 3472–3478, 2012.

[76] A. Srivastava, A. Majumdar, and B. S. Butola, “Improving the impact resistance performance of Kevlar fabrics using silica based shear thickening fluid,” *Mater. Sci. Eng. A*, vol. 529, no. 1, pp. 224–229, 2011.

[77] D. Micheli, A. Vricella, R. Pastore, A. Del, A. Giusti, M. Albano, M. Marchetti, F. Moglie, and V. M. Primiani, “Ballistic and electromagnetic shielding behaviour of multifunctional Kevlar fi ber reinforced epoxy composites modi fi ed by carbon nanotubes,” vol. 104, pp. 141–156, 2016.

[78] M. Su, A. Gu, G. Liang, and L. Yuan, “The effect of oxygen-plasma treatment on Kevlar fibers and the properties of Kevlar fibers/bismaleimide composites,” *Appl. Surf. Sci.*, vol. 257, no. 8, pp. 3158–3167, 2011.

[79] S. L. Valença, S. Griza, V. G. De Oliveira, M. Sussuchi, F. Guilherme, and D. C. Cunha, “COMPOSITE REINFORCED WITH KEVLAR PLAIN FABRIC Abstract :,” 2014.

[80] R. Nath, D. Fenner, and C. Galiotis, “Finite element modelling of interfacial failure in

model carbon fibre-epoxy composites," *J. Mater. Sci.*, vol. 31, pp. 2879–2883, 1996.

[81] I. F. Brown and C. J. Burgoyne, "The friction and wear of Kevlar 49 sliding against aluminium at low velocity under high contact pressures," *Wear*, vol. 236, no. 1–2, pp. 315–327, 1999.

[82] M. Akay, S. K. Ah Mun, and A. Stanley, "Influence of moisture on the thermal and mechanical properties of autoclaved and oven-cured Kevlar-49/epoxy laminates," *Compos. Sci. Technol.*, vol. 57, no. 5, pp. 565–571, 1997.

[83] A. M. Hindeleh and S. M. Abdo, "Effects of annealing on the crystallinity and microparacrystallite size of Kevlar 49 fibres," *Polymer (Guildf).*, vol. 30, no. 2, pp. 218–224, Feb. 1989.

[84] a Mittelman and L. Roman, "Tensile properties of real unidirectional Kevlar / epoxy composites," vol. 21, no. 1, pp. 63–69, 1990.

[85] P. N. B. Reis, J. A. M. ZhangFerreira, Z. Y. Zhang, T. Benameur, and M. O. W. Richardson, "Impact response of Kevlar composites with nanoclay enhanced epoxy matrix," *Compos. Part B Eng.*, vol. 46, pp. 7–14, 2013.

[86] A. Bendada, S. Sfarra, M. Genest, D. Paoletti, S. Rott, E. Talmy, C. Ibarra-Castanedo, and X. Maldague, "How to reveal subsurface defects in Kevlar?? composite materials after an impact loading using infrared vision and optical NDT techniques?," *Eng. Fract. Mech.*, vol. 108, pp. 195–208, 2013.

[87] J.-S. Lin, "Effect of surface modification by bromination and metalation on Kevlar fibre-epoxy adhesion," *Eur. Polym. J.*, vol. 38, no. 1, pp. 79–86, 2002.